Synthesis And Characterization Of Dyes And Benzimidazole-Phenols For The Study Of Electron Transfer

by

John Jacob Tomlin

A Dissertation Presented in Partial Fulfillment
of the Requirements for the Degree
Doctor of Philosophy

Approved April 2015 by the
Graduate Supervisory Committee:

Ana Moore, Chair
Devens Gust
Gerdenis Kodis

ARIZONA STATE UNIVERSITY

May 2015

ABSTRACT

Converting solar energy into electricity is a reasonable way to ameliorate the current untenable energy situation. One way to harness solar energy is to mimic the mechanisms already present in natural photosynthesis. A key component of many artificial photosynthetic systems is the linker connecting the dye to an electrode. Studying the associated electron transport process is important for improving linker efficiency. Similarly it is important to be able to control the electron transfer to the dye from a water oxidation catalyst, and to be able to improve the lifetime of the charge separated state. Natural photosynthesis provides a blueprint for this in the tyrosine-histidine pair in photosystem II. In this work, research on these topics is described.

For Diana, John, Rose and Sara, for their love and support

ACKNOWLEDGEMENTS

I would like to thank my advisors, Professors Ana L. Moore, Thomas A. Moore and Devens Gust for their support. I would also like to thank Professors Marcia Levitus, Ian Gould and Ulrich Haussermann for their participation as my committee for my oral examination, and Dr. Gerdenis Kodis for his membership in my graduate supervisory committee. I would also like to thank I would also like to thank professors Ernesto Mariño-Ochoa, Gonzalo Cosa, Rodrigo E. Palacios, Sharon Hammes-Schiffer and Dr. Alexander Soudakov for there collaborative efforts. Thanks to Dr. John Lopez for his help in obtaining mass spectra. Thanks to Dr. Brian Cherry, and Professor Jeff Yarger for teaching me to obtain and interpret NMR spectra. Thanks to Larry Orr, and Alexander Melkozernov for there administration. Thanks to Current and past members of the Gust, Moore, Moore group Dr. Paul Liddell, Professor Gary Moore, Dr. Anne-Lucie Teillot, Dr. Michael Vaughn, Dr. Jesse Bergkamp, Dr. Smitha Pillai, Dr. Benjamin Sherman, Dr. Dalvin Mendez, Dr. Manuel Llansola Portolés, Dr. Anindya Roy, Dr. Maxime Fournier, Antaeres' Antoniuk-Pablant, Ian Pahk, Marely Tejeda Ferrari, Dustin Patterson. Special thanks to Dr. Peter J. Pessiki for getting me started in chemistry. I would also like to thank the Department of Energy and the National Science Foundation for funding my research. And lastly I would like to thank my Family, and friends for supporting me, with special thanks going to John, Rose, Sara and Diana.

TABLE OF CONTENTS

Page

LIST OF FIGURES

Figure Page

Figure Page

Figure Page

LIST OF SCHEMES

Scheme Page

LIST OF TABLES

Table Page

INTRODUCTION

Humanity's demand for energy, especially as regards our use of fossil fuels, has led to significant damage to many different components of the planetary ecosystem. Of special concern is the contribution to the increase in greenhouse gasses caused by the burning of fossil fuels.(213) Though there are many potential sources of energy available to humanity, very few options exist that won't continue to cause damage to the environment. One such option is solar energy.

Virtually all energy currently available to humanity has its ultimate source in the sun. Even fossil fuels originated principally as plant matter, and that matter was created through the action of photosynthesis on carbon dioxide from the atmosphere, along with water. The sun provides a significant amount of energy, on the order of 15,600 TW in the form of light that is able to make it to the surface of the earth, making solar power a compelling target for energy research.(214, 215)

Natural photosynthesis is a well-known system in nature that is able to obtain energy from the sun. Of special interest is photosystem II, in which light is absorbed by antenna pigments, and the energy from the light is then transferred to the P680 pigment cluster in the reaction center, shown in figure 1.(216) This excitation, then causes the transfer of an electron from the P680 to the nearby pheophytin, followed by further electron transfer to a plastoquinone molecule, which is eventually reduced to plastoquinol. The P680 ground state is then regenerated by transferring the hole that was present on it to a nearby tyrosine moiety, and through the process of proton coupled electron transfer (PCET), to the oxygen-evolving complex.(171) After four such occurrences, a sufficient number of

oxidizing equivalents is accumulated on the oxygen evolving complex to oxidize water, producing oxygen gas, and four protons.

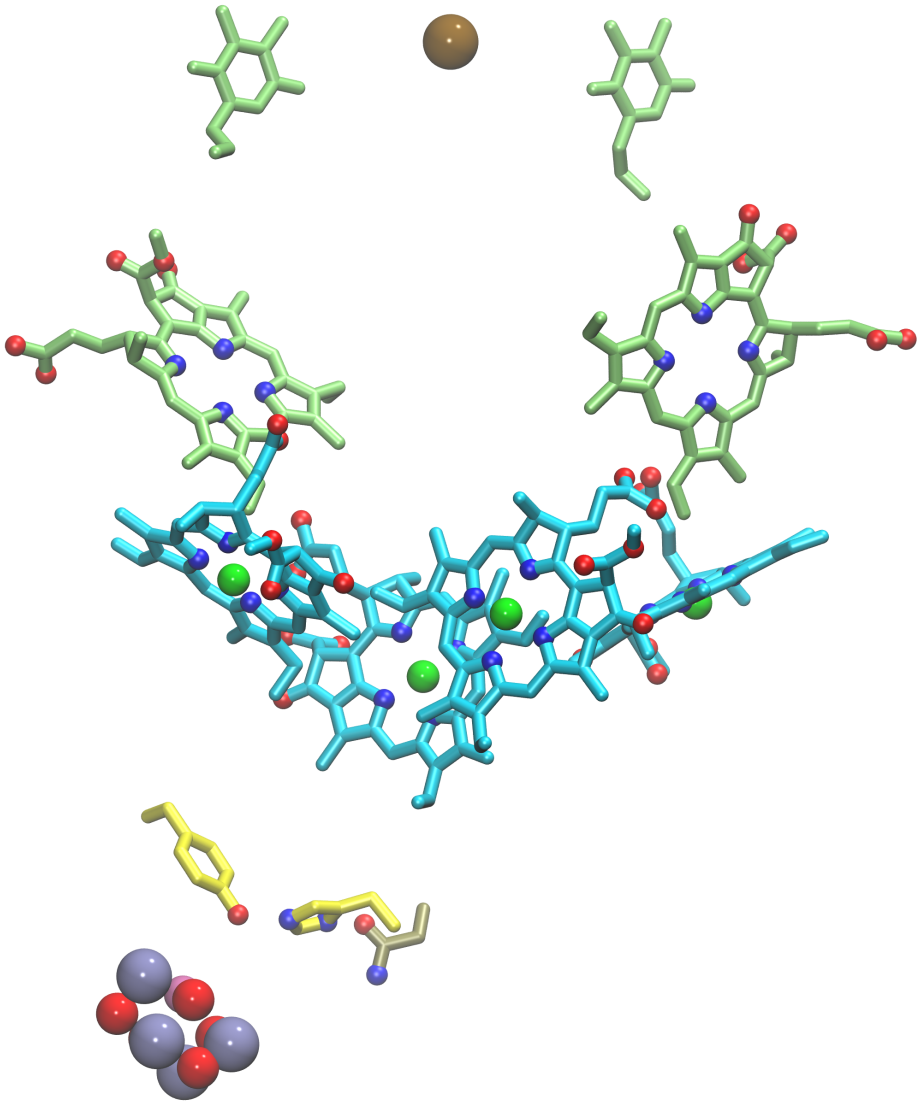

6. Figure 1 – The reaction center of photosystem II (216)

Though natural photosynthesis does not directly provide usable electrical power, the processes involved include both the transport of electrons, through the reduction and diffusion of plastoquinone, and the generation of a proton gradient. Mimicking the light harvesting components of this system using artificial dyes allows for the creation of organic photocells, which can be used to generate electricity. In addition to directly generating electrical power it is also possible to mimic another property of Photosystem II, by utilizing catalysts to help oxidize water. The electrons, and protons produce by the oxidation of water can then be used to produce, with the help of addition catalysts, hydrogen gas, a storable fuel. It may even be possible in the future to reduce carbon dioxide to produce higher energy fuels such as formaldehyde and methanol.

In many artificial photosynthetic systems like that seen in figure 2, a dye is attached to a semiconducting electrode, and is also either adjacent to or directly attached to a water oxidation catalyst such as an iridium oxide nanoparticle. When the dye is excited by light, an electron is injected into the conduction band of the semiconductor, followed by the abstraction of an electron from the oxidation catalyst to regenerate the ground state of the dye. In a similar manner to natural photosynthesis, after four cycles, water can then be oxidized. The electrons and protons thus produced are then transferred to the other half of the cell where they can be used to reduce the protons and produce hydrogen gas.

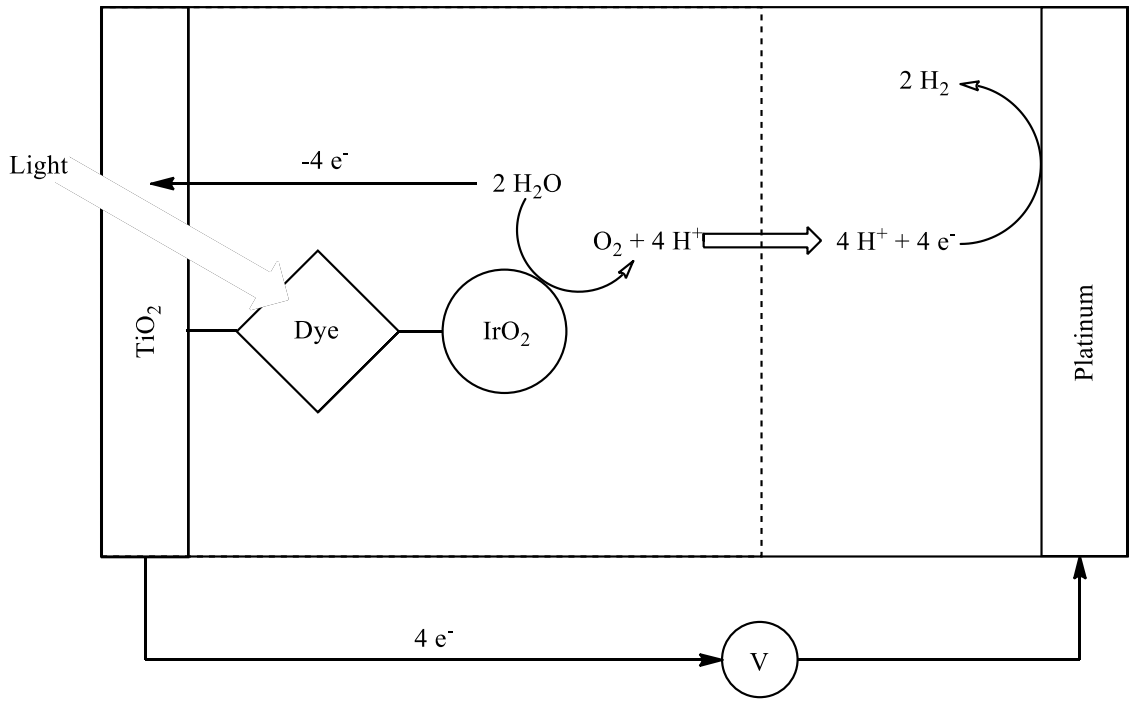

Figure 2 – Artificial Photosynthetic System

ELECTRON TRANSFER IN DYE-SEMICONDUCTOR SYSTEMS

Many artificial photosynthetic systems involve the attachment of a dye to a semiconductor electrode. The study of the electron transfer in dye-semiconductor systems is therefore important to the understanding of the processes involved in artificial photosynthetic systems.(1-6) In conventional systems, however, the large degree of inhomogeneity in the binding and orientation of the dye on the electrode can complicate the study of the electron transfer process.(28)

There have been many spectroscopic studies done on the photoinduced electron transfer from dyes to semiconductor nanoparticles, however the studies are often complicated not only by the binding inhomogeneity, but also by the size distribution and crystallinity of the nanoparticles being studies. In addition there are often unbound dye molecules trapped near the nanoparticle, which can complicate the kinetics being studies by interfering with the electron transfer process.(1, 29-32) These problems can be ameliorated by using a system that is well characterized in both the size of the nanoparticles and the concentration of the dye.(1, 4-6, 25, 33-63)

Perylene dyes are a good choice for this type of study because they are highly stable, and there redox properties can be easily tuned by adjusting their functionalization. Several perylene dyes were studied and are shown in figure 3.(64-75) These perylene dyes contain carboxylic anhydride moieties which, after hydrolysis, are able to bind to the nanoparticle as carboxylic acid anchoring groups.(77-79)

Initially the nanoparticles used were produced in reverse micelles (Chapter 2), which allowed for finer control of the nanoparticle size distribution.(39, 52, 53, 56, 58) However the surfactant groups interfered with the binding of some of the dyes due to

steric effects. In addition the electric field near the nanoparticle surface generated by the ionic properties of the polar head of the surfactant may have affected the electron transfer. Because of these problems, titanium dioxide nanoparticles were prepared without surfactant molecules (Chapter 3), and suspended in an organic solvent. In both cases, electron transfer was observed for perylene dyes 1 and 2, but not for dye 3.

1) R= 

2) R= 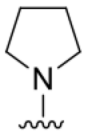

3) R= 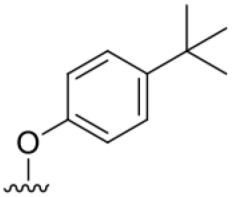

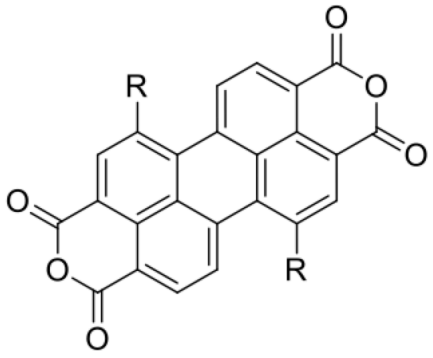

Figure 3 – Perylenes used in the studies of Chapters 2 and 3

FREEBASE PORPHYRIN DYES

Because of their similarity to chlorophyll, and their relatively simpler synthesis, porphyrins are commonly studied as light harvesting molecules for use in dye sensitized solar cells and artificial photosynthetic systems.(172-175) In addition, porphyrin dyes do not contain rare elements. Due to the presence of rare metals in many water oxidation catalysts, a lot of attention has been devoted to developing organic catalysts.(179-183) Unfortunately, in artificial photosynthetic systems the ration of dye to catalyst can exceed 1000:1, therefore insuring that the dye contains no rare metals also becomes important. In artificial photosynthetic systems ruthenium dyes are used the most, though systems using zinc porphyrins have been able to produce photocurrents.(178, 184-188)

In chapter 4 water splitting is demonstrated using a series of free-base porphyrins using visible light. Photocurrents were observed which were comparable to ruthenium dyes.

BENZIMIDAZOLE-PHENOLS

In photosystem II the electron transfer from the oxygen evolving complex to the oxidized P680 pigment complex is coupled to proton movement, it has been suggested that this results in an increase of the charge separation lifetime. This is critical in photosynthesis since the charge separation has to last long enough to allow for the accumulation of sufficient oxidizing equivalents on the oxygen evolving complex. In the natural system this occurs through the oxidation of a tyrosine moiety, followed by proton transfer to a nearby hydrogen bonded histidine moiety. In addition, there is a asparagine moiety hydrogen bonded to the other side of the histidine ring likely providing another pathway for proton transfer. (217-220)

Benzimidazole-phenols (BIPs) have been previously studied as synthetic mimics of the tyrosine histidine pair.(221) It is expected that, for the PCET step to work optimally the proton and electron transfer should occur in a concerted manner. If this is the case, then it would be expected that the kinetic isotope effect (KIE) of the proton transfer should be larger than 1, since the proton transfer would occur in the rate limiting step. In chapter 5 The KIE of several BIP models, seen in figure 4, are studied by computational or electrochemical methods. It is determined that inclusion of a methyl ester or carboxylic acid moiety on the 4-position of the benzimidazole is necessary to increases the KIE above 1.

BIP-H

BIP-COOH

BIP-COOMe

BIP-CONEt$_2$

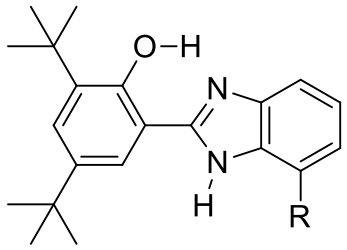

Figure 4 – Benzimidazole-phenols studied in chapter 5

SPECTRAL CHARACTERISTICS AND PHOTOSENSITIZATION OF TIO2 NANOPARTICLES IN REVERSE MICELLES BY PERYLENES

Laura I. Hernández †, Robert Godin ‡, Jesse J. Bergkamp §, Manuel J. Llansola Portolés §, Benjamin D. Sherman §, John Tomlin §, Gerdenis Kodis §, Dalvin D. Méndez-Hernández §, Sonia Bertolotti †, Carlos A. Chesta †, Ernesto Mariño-Ochoa ⁄⁄ , Ana L. Moore §, Thomas A. Moore §, Gonzalo Cosa ‡, and Rodrigo E. Palacios *†

† Departamento de Química, Facultad de Ciencias Exactas Físico-Químicas y Naturales, Universidad Nacional de Río Cuarto, Río Cuarto, Córdoba 5800, Argentina

‡ Department of Chemistry and Center for Self Assembled Chemical Structures (CSACS/CRMAA), McGill University, Otto Maass Chemistry Building, 801 Sherbrooke Street West, Montreal, QC, H3A 0B8, Canada

§ Department of Chemistry and Biochemistry, Center for Bioenergy and Photosynthesis, Arizona State University, Tempe, Arizona 85287-1604, United States

⁄⁄ Department of Chemistry, Tecnológico de Monterrey, Campus Monterrey, Monterrey, NL, 64849, México

*E-mail: rpalacios@exa.unrc.edu.ar.

This article is part of the Paul F. Barbara Memorial Issue special issue.

(This article was adapted with permission from a previously published article: Hernandez, L.; Godin, R.; Bergkamp, J. J.; Llansola Portoles, M. J.; Sherman, B. D.; Tomlin, J.; Bertolotti, S.; Chesta, C. A.; Marino-Ochoa, E.; Moore, A. L.; Moore, T. A.;

Cosa, G.; Palacios, R. E. *J. Phys. Chem. B*, 2013, *117* (16), pp 4568–4581 doi: 10.1021/jp3086792. My contributions included synthesis and writing of the manuscript. See Appendix D for permission details)

ABSTRACT

We report on the photosensitization of titanium dioxide nanoparticles (TiO_2 NPs) synthesized inside AOT (bis(2-ethylhexyl) sulfosuccinate sodium salt) reverse micelles following photoexcitation of perylene derivatives with dicarboxylate anchoring groups. The dyes, 1,7-dibromoperylene-3,4,9,10-tetracarboxy dianhydride (1), 1,7-dipyrrolidinylperylene-3,4,9,10-tetracarboxy dianhydride (2), and 1,7-bis(4-*tert*-butylphenyloxy)perylene-3,4,9,10-tetracarboxy dianhydride (3), have considerably different driving forces for photoinduced electron injection into the TiO_2 conduction band, as estimated by electrochemical measurements and quantum mechanical calculations. Fluorescence anisotropy measurements indicate that dyes 1 and 2 are preferentially solubilized in the micellar structure, creating a relatively large local concentration that favors the attachment of the dye to the TiO_2 surface. The binding process was followed by monitoring the hypsochromic shift of the dye absorption spectra over time for 1 and 2. Photoinduced electron transfer from the singlet excited state of 1 and 2 to the TiO_2 conduction band (CB) is indicated by emission quenching of the TiO_2-bound form of the dyes and confirmed by transient absorption measurements of the radical cation of the dyes and free carriers (injected electrons) in the TiO_2 semiconductor. Steady state and transient spectroscopy indicate that dye 3 does not bind to the TiO_2 NPs and does not photosensitize the semiconductor. This observation was rationalized as a consequence of the bulky *t*-butylphenyloxy groups which create a strong steric

impediment for deep access of the dye within the micelle structure to reach the semiconductor oxide surface.

INTRODUCTION

The study of interfacial electron transfer (IET) in dye–semiconductor nanoparticle systems is an area of considerable research interest from both fundamental and practical points of view.(1-6) Modification of metal oxide semiconductors with organic dyes is a well-known method to extend their photoresponse to visible light. Application of metal oxide/dye systems has been extensively demonstrated in a variety of organic–electronic devices such as dye-sensitized solar cells (DSSC),(7-12) heterogeneous photocatalysis,(13-18) and chemical sensing.(19-23) The current need for performance improvement in many of these devices entails a better understanding of the IET process which plays a central role in device operation.(1, 12, 24-27)

Dye to semiconductor nanoparticle (NP) photoinduced electron transfer has been widely studied in nanostructured metal oxide semiconductor films where the dye molecules are deposited in a relatively uncontrolled manner leading to a number of physically adsorbed and nonbound aggregated dyes with poor electronic coupling with the semiconductor.(28) A large number of the electron transfer studies on these systems have been performed using steady state and time-resolved UV–vis spectroscopic techniques. The results obtained usually show complex kinetics and spectra due to the heterogeneous nature of the dye–NP binding, the size and crystallinity of the semiconductor NPs, scattering effects of the nanostructured film, and the presence of unbound trapped dye and dye aggregates.(1, 29-32) The use of well characterized dye-sensitized NP

suspensions can help to overcome many of these difficulties (by reducing scattering effects and providing a more homogeneous set of semiconductor NPs), and accordingly a large number of studies have been carried out on such systems.(1, 4-6, 25, 33-63) In some of these studies, well dispersed and homogeneous semiconductor particle suspensions were obtained via a microemulsion method.(39, 52, 53, 56, 58)

Perylene based dyes have been extensively explored as photosensitizers for DSSC because they absorb strongly in the visible, are chemically photostable, and are amenable for fine-tuning their light absorbing and redox properties through structural modifications.(64-75) Additionally, the relatively low number of excited state relaxation pathways in perylenes, as compared to the prototypical ruthenium based dyes, facilitates the study of IET.(75) Binding of perylene derivatives to TiO_2 has been achieved through carboxylic acid and dicarboxylic acid groups derived from anhydrides.(66-74) The nature of the binding and the electronic coupling between the dye and the semiconductor has been shown to influence the dye excited state properties and IET behavior.(66, 67, 69, 73, 74, 76) Binding of perylene derivatives to metal NPs and metal-oxide and nanorods has also been achieved through thiol and sulfide groups, respectively.(77-79)

Herein we report studies of the sensitization of TiO_2 nanoparticles in a reverse micelle suspension by perylene dye derivatives. The perylene dyes used in this study, (1,7-dibromoperylene-3,4,9,10-tetracarboxy dianhydride (1), 1,7-dipyrrolidinylperylene-3,4,9,10-tetracarboxy dianhydride (2), and 1,7-bis(4-*tert*-butylphenyloxy)perylene-3,4,9,10-tetracarboxy dianhydride (3), contain cyclic anhydride moieties which hydrolyze to yield two carboxylic acid groups that serve as anchoring groups to the TiO_2 surface.

Steady state and transient spectroscopic results indicate that a large portion of dyes 1 and 2 are attached to the TiO_2 NP surface and can effectively initiate IET. On the other hand, spectroscopic results show inefficient binding of dye 3 to the semiconductor surface and lack of photoinduced electron transfer, indicating that the bulky structure of the dye hampers the binding process within the micelle–TiO_2 NP structure.

EXPERIMENTAL AND THEORETICAL METHODS

Materials

Titanium tetraisopropoxide (TTIP, ≥97.0%), isopropanol (anhydrous, 99.5%), 3,4,9,10-perylenetetracarboxylic dianydride (97%), 2,6-diisopropylaniline (97%), pyrrolidine (99%), and bis(2-ethylhexyl) sulfosuccinate sodium salt (AOT, 98%) were purchased from Sigma-Aldrich and used as received. Anhydrous *tert*-butyl alcohol was purchased from Alfa-Aesar and used as received. Thin layer chromatography plates (250 μm), with fluorescent and nonfluorescent indicators, were purchased from Analtech, Inc. Silica gel (SiliaFlash F60 40–63 μm) used for column chromatography was purchased from SILICYCLE. Syringe PTFE membrane (200 nm pore) filters: disposable assemblies (PALL, Acrodisc. CR 25 mm) and disposable membranes (Microclar, T02013WPH) on a reusable filter holder (Cole-Palmer, CZ-02928-10) were used interchangeably. *N*-Heptane (HPLC grade), ethanol (anhydrous, HPLC grade), and potassium hydroxide (KOH, ACS reagent grade) were purchased from Merk. Perchloric acid (ACS reagent grade) was purchased from Taurus. Ultrapure water (18Ω, Millipore) and bottled water (Sintorgan, HPLC grade) were used interchangeably. Tetrahydrofuran (THF) (Sintorgan, HPLC) was

distilled over metallic sodium with benzophenone. All solvents used for column chromatography were distilled before use.

Synthesis

1,7-Dibromoperylene-3,4,9,10-tetracarboxy dianhydride (1)

Compound 1 was obtained following a literature procedure.(74)

1,7-Dipyrrolidinylperylene-3,4,9,10-tetracarboxy dianhydride (2)

Compound 2 was prepared following slightly modified reported protocols. First, *N*,*N*′-bis(2,6-diisopropylphenyl)-1,7-bis(pyrrolidin-1-yl)perylene-3,4,9,10-tetracarboxylic acid bisimide was prepared.(74) This was followed by base hydrolysis in *tert*-butyl alcohol and purification by column chromatography using 2% ethyl acetate in chloroform as eluent on silica gel(80) to yield compound 2. All compounds were characterized by ^{1}H NMR and MALDI-TOF mass spectrometry; the spectra were identical to those previously reported.

1,7-Bis(4-tert-butylphenyloxy)perylene-3,4,9,10-tetracarboxy dianhydride (3)

Compound 3 was prepared following a modified published procedure.(81) A portion of compound 1 (8 g, 14.5 mmol), 4-*tert*-butlyphenol (7.2 g, 48.0 mmol), and cesium carbonate (9.5 g, 29.1 mmol) were dissolved in dimethylformamide (485 mL) and heated at reflux for 4 h under nitrogen. The reaction mixture was poured into water (200 mL) and neutralized with aqueous 1 M HCl. The precipitate was filtered and washed repeatedly with water and then methanol to give a crude solid. A 100 mg portion was then purified by preparatory TLC, which was followed by flash column chromatography

on silica gel using chloroform as the eluent to afford a red solid (15.4 mg, 0.022 mmol, 15.4% yield). ^{1}H NMR (Chloroform-d, 400 MHz): δ_H, ppm 9.64 (d, J = 8.2 Hz, 2 H), 8.71 (d, J = 8.2 Hz, 2 H), 8.28 (s, 2 H), 7.52 (d, J = 8.6 Hz, 4 H), 7.13 (d, J = 8.6 Hz, 4 H), 1.39 (s, 18 H).

Titanium Dioxide Nanoparticles (TiO_2 NPs)

The synthesis was carried out by the hydrolysis of TTIP inside the water pool of AOT reverse micelles suspended in *n*-heptane.(52) In this system, the micelles act as nanoreactors, where the hydrolysis reaction takes place, preventing the formation of TiO_2 nanoparticle aggregates. A micellar suspension of w_0 = 1 (w_0 = [H_2O]/[AOT]) was prepared by adding 220 μL of aqueous $HClO_4$ (0.02 M) to 30 mL of AOT solution (0.4 M) in *n*-heptane under continuous stirring. A 0.2 mL aliquot of a TTIP stock solution (0.136 M) in anhydrous isopropanol was added dropwise to 30 mL of the micellar suspension under mild agitation at room temperature. Stirring was continued for 20 min to obtain a clear micellar suspension containing TiO_2 NPs (see Figure 6, inset).

Micelles without TiO_2 NPs

A control sample of micelles without TiO_2 NPs was prepared following exactly the same procedure described above except for the addition of TTIP. We estimate a significant proton concentration inside the reverse micelle water pool based on the concentration of $HClO_4$ in the aqueous solution used for micelle formation. However, calculation of pH is

not valid in these systems where the nanoscopic size of the water pool limits the number of avalible water molecules.(82)

Instruments and Measurements

Steady State Absorption

Spectra were recorded in 1 cm path length cuvettes with the following spectrophotometers: diode array HP 8452, Shimadzu - UV-IR (2041PC), and Hitachi double beam UV/vis spectrophotometer (U-2800).

Steady State Fluorescence

Spectra and fluorescence anisotropy measurements were obtained with the following spectrofluorometers: Horiba FluoroMax-4 and PTI Quantamaster 40, both equipped with motorized polarizers. To compare emission intensities of samples measured with absorbances not matched at the excitation wavelength (Abs(λ_{ex})), the corrected emission intensity of a given sample ($I_{corr}(\lambda_{em})$) was calculated from the observed emission intensity ($I_{obs}(\lambda_{em})$) using eqs 1 and 2:(83)

$$I_{A,corr}(\lambda_{em}) = \left(\frac{Abs_B(\lambda_{ex})}{Abs_A(\lambda_{ex})}\right) I_{A,obs}(\lambda_{em}) \cdot 10^{\left(\frac{Abs_A(\lambda_{ex}) + Abs_A(\lambda_{em})}{2}\right)} \quad (1)$$

and

$$I_{B,corr}(\lambda_{em}) = I_{B,obs}(\lambda_{em}) \cdot 10^{\left(\frac{Abs_B(\lambda_{ex}) + Abs_B(\lambda_{em})}{2}\right)} \quad (2)$$

where λ_{ex} and λ_{em} are excitation and emission wavelengths, respectively, and the subscripts A and B correspond to the different samples for which the emission intensity is compared.

Time Resolved Fluorescence

Fluorescence lifetime measurements were performed with a time-correlated single photon counting (TC-SPC) system. The excitation source was a fiber supercontinuum laser based on a passive mode-locked fiber laser and a high-nonlinearity photonic crystal fiber supercontinuum generator (Fianium SC450). The laser provides 6 ps pulses at a repetition rate variable between 0.1 and 40 MHz. The laser output was sent through an Acousto-Optical Tunable Filter (Fianium AOTF) to obtain excitation pulses at the desired wavelength. Fluorescence emission was collected at 90° and detected using a double-grating monochromator (Jobin-Yvon, Gemini-180) and a microchannel plate photomultiplier tube (Hamamatsu R3809U-50). The polarization of the emission was 54.7° relative to that of the excitation. Data acquisition was done using a single photon counting card (Becker-Hickl, SPC-830). The IRF had a FWHM of ~50 ps, measured from the scattering of sample at the excitation wavelength. The data was globally fitted as a sum of exponential decays including IRF deconvolution using locally written software (ASUFIT)(84) developed in a MATLAB environment (Mathworks Inc.).

Time Resolved Absorption

Femtosecond to nanosecond transient absorption measurements were acquired with a kilohertz pulsed laser source and a pump–probe optical setup. Laser pulses of 100 fs at 800 nm were generated from an amplified, mode-locked titanium sapphire kilohertz laser

system (Millennia/Tsunami/Spitfire, Spectra Physics). Part of the laser pulse energy was sent through an optical delay line and focused onto a 2 mm sapphire plate to generate a white light continuum for probe beam. The remainder of the pulse energy was used to pump an optical parametric amplifier (Spectra Physics) to generate excitation pulses at different wavelengths, which were modulated using a mechanical chopper. The excitation intensity was adjusted using a continuously variable neutral density filter. The probe beam was sent through a monochromator (SP150, Action Res. Corp.) and recorded by a diode detector (model 2032, New Focus Inc.) and boxcar (SR250, Stanford Research Systems). The instrument response function was ca. 200 fs.

Nanosecond transient absorption measurements were recorded with excitation from an optical parametric oscillator pumped by the third harmonic of a Nd:YAG laser (Ekspla NT342B). The pulse width was ~4–5 ns, and the repetition rate was 10 Hz. The detection portion of the spectrometer (Proteus) was manufactured by Ultrafast Systems. The instrument response function was ca. 4.8 ns.

Transient absorption data analysis was carried out using ASUFIT. In brief, decay-associated spectra were obtained by fitting the transient absorption kinetic traces over a selected wavelength region simultaneously as described by eq 3 (parallel kinetic model)

$$I_{B,corr}(\lambda_{em}) = I_{B,obs}(\lambda_{em}) \cdot 10^{\left(\frac{Abs_B(\lambda_{ex}) + Abs_B(\lambda_{em})}{2}\right)}$$

(3)

where $\Delta A(\lambda, t)$ is the observed absorption change at a given wavelength at time delay t and n is the number of kinetic components used in the fitting. A plot of $A_i(\lambda)$ versus wavelength is called a decay-associated spectrum (DAS), and represents the amplitude

spectrum of the *i*th kinetic component, which has a lifetime of τ_i. The global analysis procedures described here have been extensively reviewed. Random errors associated with the reported lifetimes obtained from fluorescence and transient absorption measurements were typically ≤5%.

Structural Characterization

^{1}H NMR spectra were recorded on a 400 MHz Varian Liquid-State spectrometer. NMR samples were dissolved in deuteriochloroform with 0.03% tetramethylsilane as an internal reference. Mass spectra were obtained on an Applied Biosystems Voyager-DE STR matrix-assisted laser desorption/ionization time-of-flight spectrometer (MALDI-TOF).

Dynamic Light Scattering (DLS)

Measurements were performed with a Malvern Instrument 4700 system with detection at 90° from the excitation, at a temperature of 25 °C, and using the 488 nm spectral line of an argon ion laser. Light scattering results were analyzed with Zetasizer software (provided by the manufacturer) to obtain hydrodynamic radius distributions and polydispersity indexes. Microemulsion solutions were filtered through 200 nm pore filters right before data acquisition. Extreme care was taken to reduce the contamination by dust.

Electrochemical Measurements

Cyclic voltammograms on 1, 2, and 3 in solution were carried out in benzonitrile (1) or acetonitrile (2, 3) with 100 mM tetrabutylammonium hexafluorophosphate as supporting

electrolyte. A three electrode setup, consisting of a glassy carbon disc working electrode, platinum gauze counter electrode, and Ag^{+}/Ag quasireference, was used with the sample volume under an argon atmosphere. A CH Instruments 760D pontentiostat and corresponding software were used for all measurements. The Ag^{+}/Ag quasireference was calibrated to the ferrocenium/ferrocene (Fc^{+}/Fc) couple with $E_{Fc^{+}/Fc}$ taken as 0.45 V vs saturated calomel electrode (SCE).

Transmission Electron Microscopy

TEM micrographs were collected using a Philips CM200 TEM at 200 kV. The TiO_2–micelle microemulsion was plated on a plasma treated (10 min, air intake) 200-mesh carbon coated copper grid (Canemco, Lakefield, QC, Canada) for 1 min before wicking using filter paper. The grid was then rinsed with high purity water (HyClone, Logan, UT) to wash AOT surfactant away. TEM micrographs were analyzed using ImageJ software.(85) The "analyze particle" plug-in was used to find the outline and calculate the diameter of nanoparticles on arbitrarily thresholded images.

Computational Methodology

Geometry optimizations of dyes 1, 2, and 3 (in their open (O) and closed (C) forms) (see Figure S3a in the Supporting Information) were performed with Gaussian 09(86) using density functional theory (DFT) calculations at the B3LYP/6-31G(d) level of theory.(87-94) Using the conductor-like polarizable continuum model (CPCM), acetonitrile was implicitly included for all the optimizations.(95, 96)

RESULTS AND DISCUSSION

Perylene Dyes

Molecular Structure

The structures of perylene derivatives 1, 2, and 3 are shown in Scheme 1. On the basis of the structure of the dyes, at least three species in equilibrium can be proposed during the hydrolysis of an anhydride group (catalyzed in basic media), as shown in Scheme 1 (right). Partially hydrolyzed and/or deprotonated species, i.e., involving only one of the two anhydride rings present in the dyes, were not considered in this scheme but are also possible. As it is discussed below, the opening of at least one anhydride group to yield a dicarboxylic acid species is necessary for binding of the dyes to the TiO_2 surface. The precise nature of the interaction between the carboxylic group and the TiO_2 surface atoms still remains a subject of debate. Possible binding modes of the carboxylic acid species to the TiO_2 surface involve bidentate simple adsorption (electrostatic attraction and hydrogen bonding) and chemical bonding (ester linkage, bridging, and chelating).(76, 97)

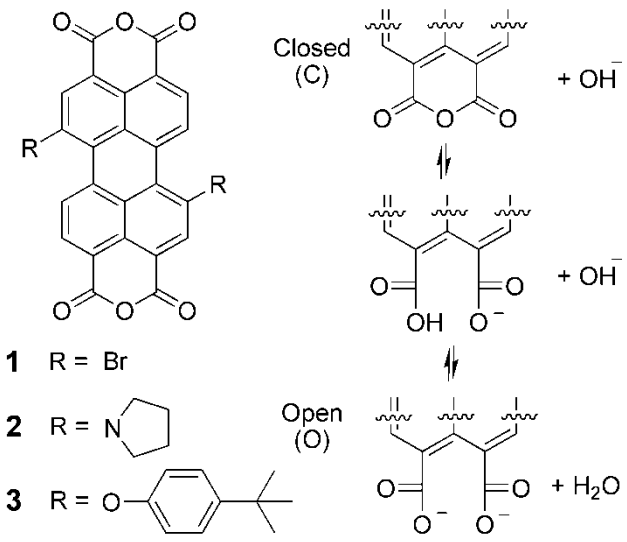

Scheme 1 – Structure of perylene dyes
(left) Molecular Structure of Dyes 1, 2, and 3; (right) Opening of Anhydride Ring under Basic Catalysis

Spectroscopic Characterization in Homogeneous Solution

Figure 5 shows the absorption and fluorescence of dyes 1 and 2 in ethanol (~10^{-6} M) as a function of time and addition of base (potassium hydroxide). The solutions were prepared by addition of a small aliquot (100 μL) of dye stock solution in THF (in this solvent, the dyes are present in the anhydride form, species C, Scheme 1) to 3 mL of ethanol with continuous stirring. The acquisition of spectra as a function of time started immediately after the stock dye solution was added to ethanol. For perylenes 1 and 3, both absorption and fluorescence spectra (Figure 5a and b) show clear isosbestic and isoemissive points, indicating the interconversion between two species with distinct spectra and similar fluorescence quantum yields. The species that absorb and emit at longer wavelengths are assigned to the anhydride form (C, Scheme 1), while the shorter wavelength absorption and emission spectra are assigned to the fully hydrolyzed form for each dye (O, Scheme 1).(66, 67, 69-71) In the case of 2, isosbestic points and isoemissive points were not observed. This indicates that there are more than two interconverting species with significantly different spectra, presumably protonated/deprotonated amines, protonated/deprotonated carboxylic acids, or *zwitterion*ic species. For all perylenes, the spectral changes observed indicate that the addition of a strong base (potassium hydroxide) is necessary to shift the equilibrium between the anhydride species (C, Scheme 1) and its hydrolyzed form (O, Scheme 1) toward the later. The base catalyzes the hydrolysis of the cyclic anhydride and deprotonates the resulting dicarboxylic acid (species O, Scheme 1). Figure 5a, c, and e show that the absorption spectra of the freshly prepared ethanol solutions (where the anhydride species prevails) are significantly

bathochromically shifted (49, 134, and 48 nm for 1, 2, and 3, respectively) compared to the corresponding spectra after base addition (when the fully hydrolyzed species prevails). The fluorescence spectra shown in Figure 5a and c were recorded with excitation at the isosbestic point for 1 and 3 (472 and 478 nm, respectively) to allow for the direct comparison of the relative fluorescence quantum yields of the anhydride and hydrolyzed species. The resulting fluorescence intensities indicate that the emission quantum yields (Φ_F) of both species (C and O) are very similar for these perylenes. For 2 the emission spectra were corrected for the number of photons absorbed at the excitation wavelength as described in the experimental section. Comparison of emission intensities before and after base addition for 2 (Figure 5d) indicates that the emission quantum yield of the hydrolyzed form is significantly larger than that of the dianhydride form ($\Phi_F^O > 8\ \Phi_F^C$). The spectral changes observed upon hydrolysis of the dyes in solution are consistent with previous reports on analogous dyes(66, 67, 69, 70, 74) and were useful for monitoring the kinetics of dye binding to TiO_2 as described below.

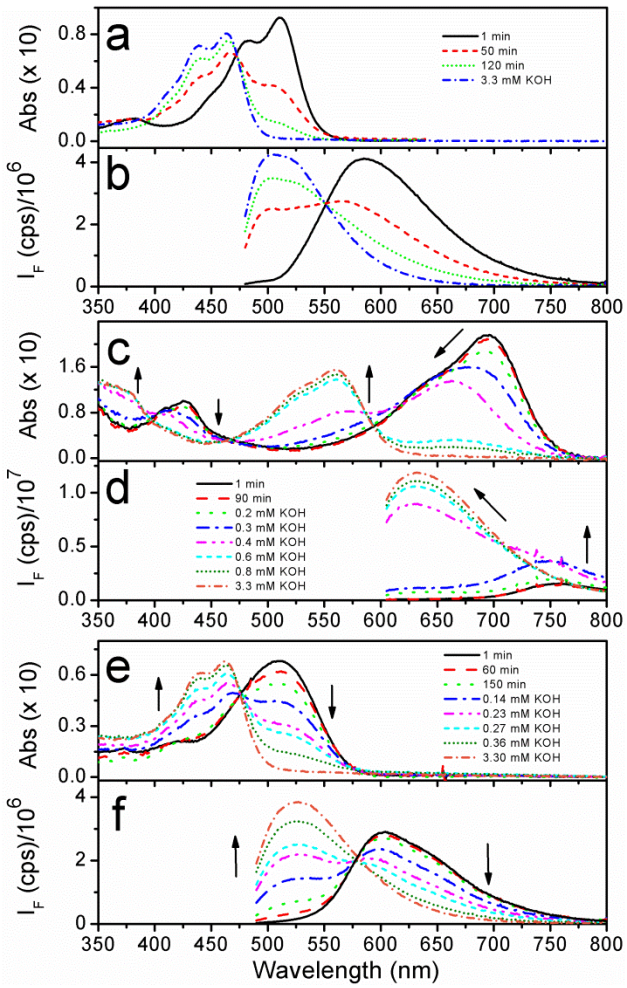

Figure 5 – Absorption and emission spectra of perylene dyes
Absorption and emission spectra of 1 (a, b), 2 (c, d), and 3 (e, f) in ethanol as a function of time and KOH addition. Emission spectra for 1 and 3 were taken with excitation at the isosbestic point (472 and 475 nm, respectively). Emission spectra for 2 were taken with excitation at 594 nm. The dye concentration was ~10–6 M for all samples. Arrows indicate the direction of change.

Energy Diagram

Scheme 2 shows the relative energetics for the oxidation of the ground and excited states of the dyes and the conduction band edge (E_{CB}) of TiO_2. The potential for the first oxidation (D^+/D) of the dyes was measured electrochemically for the cyclic anhydride (closed) form of the dyes. Attempts to measure D^+/D of the hydrolyzed (open) form were unsuccessful; thus, to a first approximation, the D^+/D of the C form will be used for calculations through the text. The potential for the oxidation of the excited state (D^+/D^*) was calculated with the equation $D^+/D^* = D^+/D - E_{00}$, where E_{00} is the zero–zero optical excitation energy estimated from the intersection of the normalized absorption and emission spectra of the hydrolyzed (open) species in ethanol (see Figure S1 in the Supporting Information). The E_{CB} value of TiO_2 was estimated as the flat-band potential(98) of polycrystalline TiO_2, −0.52 vs SCE at pH 2,(99) to account for the concentration of protons in the micelle water before NP formation. On the basis of energetic considerations, according to Scheme 2, all the dyes are capable of photoinjecting an electron in the conduction band of TiO_2. Two additional factors not considered in Scheme 2 could in principle lead to a higher driving force for the photoinduced IET process: (a) the oxidation potentials of similar dyes attached to the TiO_2 surface in their open bound form are known to shift anodically relative to those in solution in their closed form(67, 69, 71) and (b) the presence of trap-sites energetically situated between the valence and conduction bands of the TiO_2 NPs which could act as electron acceptors. Finally, the size-quantization effect observed in the TiO_2 NPs used

herein (*vide infra*) could lead to a negative shift of E_{CB} shown in Scheme 2, resulting in a decreased driving force for photoinduced electron transfer. Since the magnitude of the factors mentioned before cannot be estimated accurately, Scheme 2 provides only a first approximation for the energetics of the system.

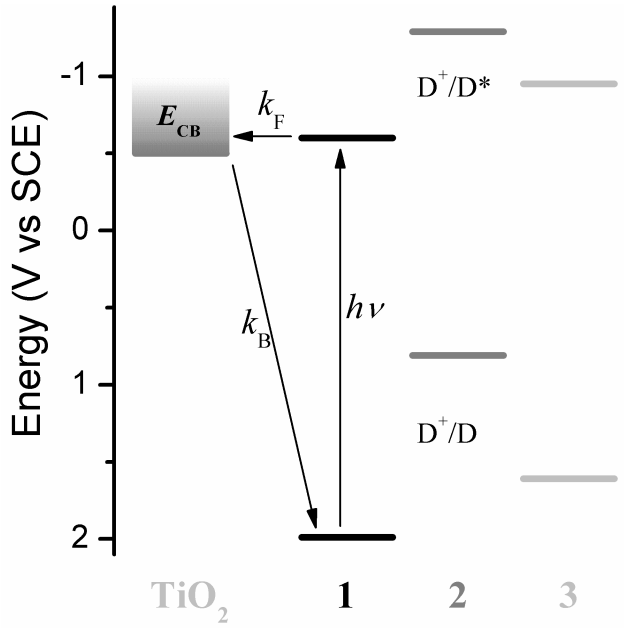

Scheme 2 – Oxidation potentials for perylene dye excited states
Diagram Depicting the Potentials for the First Oxidation and for the Oxidation of the Optically Excited States of 1, 2, and 3 and the TiO2 Conduction Band (CB) Energy. D/D+ values were measured electrochemically for the anhydride (closed) form of the dye. D/D* values were calculated as described in the text from the E00 energy of the hydrolyzed (open) form of the dyes.

Quantum mechanical calculations were performed to correlate molecular structure with the experimental electrochemical and spectroscopic parameters. The calculated HOMO–LUMO energies and energy gaps are summarized in Table 1. Rationalizing the DFT calculations by means of molecular orbital analysis, it was observed that both the HOMO and LUMO energies of all dyes shifted to less negative energies (vs vacuum) upon opening of the anhydride ring. Also, the HOMO–LUMO gap of all dyes increased upon opening of the anhydride with respect to the closed form, resulting in a hypsochromic shift of the absorption spectra. These two observations combined yield an increase in the driving force for photoinduced injection. These results are in agreement with previous work on analogous perylenes(65, 66, 70, 71) and correlate well with the electrochemical and spectroscopic data presented in Table 1 and Figure 5.

Table 1 – Potentials of opened and closed perylene dyes
Energetics of 1, 2, and 3 estimated by electrochemistry, spectroscopy and quantum mechanical calculations.

	Ox(1)[a]	Ox(2)[a]	Red(1)[a]	Red(2)[a]	HOMO[c]	LUMO[c]	HOMO-LUMO Gap[c]	E_{00} [b]
1-C	1.99 (irr)	--	-0.25 (61)	-0.52 (64)	1.99	-0.52	2.51	2.32
1-O	--	--	--	--	1.83	-0.82	2.65	2.59
2-C	0.81 (47)	0.91 (35)	-0.72 (61)	--	0.86	-1.08	1.94	1.71
2-O	--	--	--	--	0.73	-1.40	2.13	2.10
3-C	1.61 (65)	-- --	-0.51 (52)	-0.70 (55)	1.56	-0.80	2.36	2.22
3-O	--	--	--	--	1.41	-1.10	2.51	2.56

[a]E1/2 values for the indicated process reported in V vs SCE with the peak separation (ΔEp) given in mV.
[b]Calculated HOMO and LUMO energies (see Figure S3a in the Supporting Information) were normalized to the experimental oxidation potential of 1-C vs SCE by the equation Evs SCE = −Ecal – 4.26 eV.
[c]Determined from the intersection of the normalized emission and absorption spectra (measured in ethanol, Figure 1S in the Supporting Information) with the equation E00 (eV) = 1240/λ (nm).

Titanium Dioxide Nanoparticles (TiO_2 NPs)

Characterization

The hydrodynamic diameter distribution of the micellar suspension before and after the addition of TTIP stock was measured by DLS. As shown in Figure 6a (gray bars), the mean hydrodynamic diameter (d) of the micelles before TTIP addition was found to be d = 3.8 ± 0.5 nm (mean and standard deviation of three independent experiments). After formation of TiO_2 NPs, the mean hydrodynamic diameter of the micelle/TiO_2 microemulsion is slightly increased to d = 4.5 ± 0.1 nm; see Figure 6a (black bars). As seen in this figure, the size distribution of the micelle microemulsion with TiO_2 NPs is narrower than that of the micelles without TiO_2 NPs. This effect can be attributed to the fact that micelles without TiO_2 inside are inherently dynamic systems continually exchanging water from the inner pool and surfactant molecules with other micelles, so that its size varies constantly. In the case of micelles containing TiO_2 NPs, the surfactant movement is much more restricted, possibly due to attractive electrostatic interactions between the negatively charged polar head of the surfactant and the positively charged oxide surface under the acidic conditions inside the water pool. Estimation of the total concentration of micelles ($C_m = 10^{-3}$ M) and of TiO_2 NPs ($C_{NP} = 10^{-6}$ M) (see details in the Supporting Information) in the resulting solution after NP formation indicates that a large fraction of the total micelles do not contain TiO_2 NPs. Considering this estimation, we rationalize the significant difference observed for the DLS results of micelles with

and without TiO_2 NPs as a consequence of a higher light scattering efficiency of the TiO_2 NP vs that of “empty” micelles.

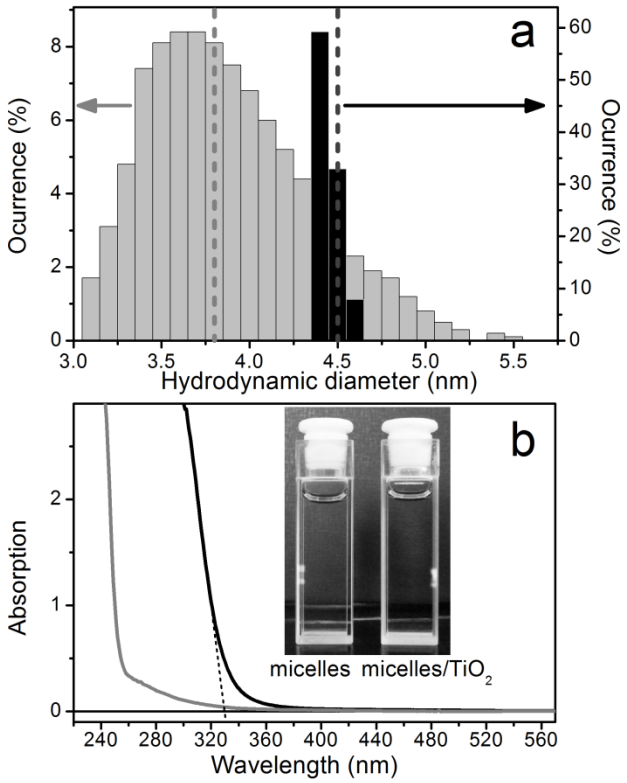

Figure 6 – DLS measurements of micelles
(a) DLS measurements of microemulsions without (gray bars) and with (black bars) TiO2 NPs. Dashed lines indicate the corresponding mean diameter values for each sample. (b) Absorption spectra of microemulsions without (gray) and with (black) TiO2 NPs. The inset shows a photograph of the micelle and micelle–TiO2 microemulsions.

Spectroscopic evidence for the formation of TiO_2 particles is seen in the absorption spectra. Figure 6b shows the absorption spectra of micelles before (dashed line) and after the addition of TTIP (solid line). In the latter, the strong absorption in the UV region is assigned to the TiO_2 band gap transition. It is well-known that the band gap of semiconductors is modulated by quantum confinement effects when the particle size reaches nanometric dimensions.(100, 101) These size-induced quantum effects produce an increase of the band gap which results in a blue-shift of the optical absorption. However, some reports in the literature indicate unusual variation of the oscillator strength of the first allowed direct transition in TiO_2 NPs (as a consequence of structural size effects) and caution about the use of the absorption shifts to estimate NP size based on quantization effects.(102) Other reports indicate that the presence of surface states and formation of a surface dipole layer on the surface of TiO_2 NPs synthesized in inverse micelles leads to sub-band gap absorption, making the comparison of shifts unreliable.(103) Our TiO_2 NPs show a significant blue shift in the absorption spectra relative to that of bulk TiO_2. Assuming that this shift is due to quantum effects, the apparent band gap of the NPs can be estimated as $E_{BG} \sim 3.88$ eV (see Figure S2 in the Supporting Information). This putative E_{BG} of TiO_2 NPs is significantly higher than that of bulk TiO_2 (3.2 and 3.0 eV for anatase and rutile phases, respectively), suggesting significant size-quantization.(53, 103-105) The prepared micelle/TiO_2 microemulsion has very low light scattering effects even at wavelengths below 350 nm due to the small

average size of the TiO_2 NP and narrow size distribution, being an ideal system for spectroscopic studies.

The morphology and crystallinity of the synthesized TiO_2 NPs were studied by transmission electron microscopy (TEM). The micrographs in Figure 7 show nearly spherical particles with an estimated mean diameter of 3.5 ± 0.7 nm (average from 123 particles). The particles have a relatively narrow size distribution, as shown on the histogram in Figure 7c. These measurements are consistent with the DLS results showing a mean diameter for the "naked" TiO_2 NPs which is slightly smaller than the mean hydrodynamic diameter of the TiO_2–micelle system. High resolution TEM (HRTEM) images (Figure 7a) show, for some particles, clear crystal planes with an average spacing of 2.186 ± 0.004 Å (mean from 6 NPs), which matches well the literature values of the (111) planes of bulk rutile TiO_2 (2.188 Å, (111) plane); no interplanar spacing in the anatase phase matches this value. Even though this information is not sufficient to categorically assign a crystal structure to the synthesized nanoparticles, since this would require a more detailed study involving diffraction experiments, the results suggest the rutile phase as the most likely one. However, given the large number of factors that affect the observation of NP crystalline structure in TEM micrographs,(106) we cannot make a definitive assignment of the crystalline nature of the prepared TiO_2 nanoparticles based only on HRTEM images.

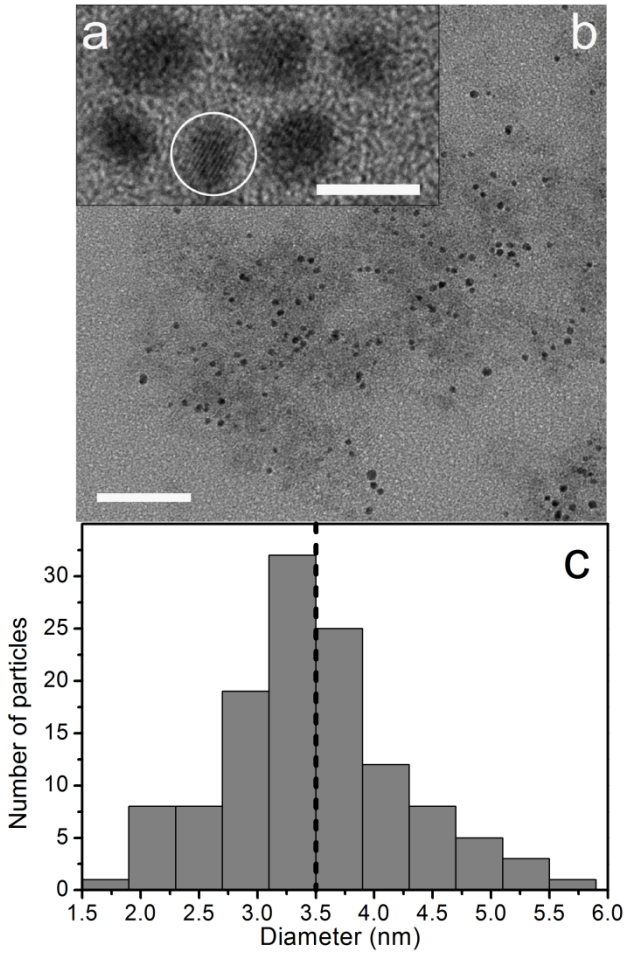

Figure 7 – TEM micrographs of TiO2 nanoparticles
TEM micrographs of TiO2 nanoparticles synthesized in AOT reverse micelles. (a) High magnification image showing crystallinity in the circled TiO2 nanoparticle. Scale bar = 5 nm. (b) Representative region showing TiO2 nanoparticles as dark circles and excess AOT surfactant as dark gray areas. Scale bar = 50 nm. (c) Histogram of nanoparticle diameter constructed by analyzing TEM micrographs; see details in text. The dashed line indicates the mean diameter value.

Dye–TiO_2 NP Systems

Assembly

Binding of perylene 1 and 2 to TiO_2 NPs in a microemulsion was carried out by addition of 100 μL of dye stock solution (~10^{-4} M) in THF to 3 mL of a TiO_2–NP–micelle suspension ([TiO_2] = 0.109 g/L) in *n*-heptane (for pump–probe experiments, the dye/TiO_2 NP concentration ratio was increased 2 times). The microemulsion was left incubating for >4 h, and absorption spectra were recorded at periodic time intervals immediately after addition of the dye, as shown in Figure 8. A control sample of micelles without TiO_2 was prepared as described in the Materials section and analyzed in an analogous manner. The hypsochromic shift observed in the absorption spectra of dyes 1 and 2 in the presence of TiO_2 is indicative of opening of the anhydride ring and suggests binding of the resulting dicarboxylic form of the dye to the semiconductor.(65-71, 73, 74) Further evidence for dye binding to the oxide surface comes from time-resolved experiments that are described in detail below and which show the formation of the dye$^{\bullet+}$–$TiO_2(e^-)$ charge separated state. Other authors have confirmed binding of dyes (containing carboxylic acid moieties) to TiO_2 films using FTIR by monitoring the frequency shift of the carbonyl band upon acid deprotonation and binding to the oxide surface.(107, 108) In the micelle systems described herein, AOT surfactant molecules are in an ~10^5-fold excess relative to dye molecules (*vide infra*); thus, the IR absorption of the AOT ester groups dominates the carbonyl band signal and precludes observation of dye binding to TiO_2 by vibrational

spectroscopy. In both systems, 1-TiO_2 and 2-TiO_2, the binding of the dye was a relatively slow process, as shown by the kinetic traces in the insets of Figure 8a,b. When 3 was added to a TiO_2 NP microemulsion, no significant changes were observed in the absorption and emission spectra over time, indicating that the dye's anhydride groups are not hydrolyzed. Under these conditions, the attachment of the dye to the TiO_2 surface through the possible binding modes of the carboxylic acid species is precluded.

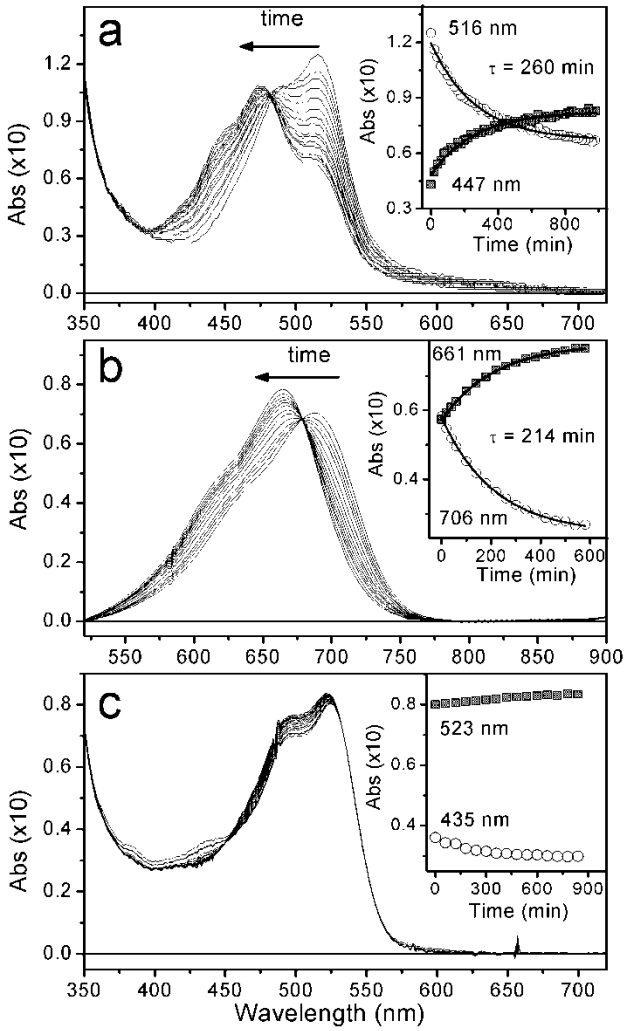

Figure 8 – Absorbtion spectra of perylenes in TiO2 nanoparticle microemulsion Absorption spectra of 1 (a), 2 (b), and 3 (c) in a microemulsion containing TiO2 NPs as a function of time. The inset displays kinetic traces at the indicated wavelengths (circles and squares) and corresponding monoexponential fittings (solid lines) with a shared time constant.

Figure 9 shows the absorption, fluorescence emission, and excitation spectra of the dyes in samples described above after incubation for 17 h. No further spectral changes were observed beyond this time. The absorption spectrum of 1 in the presence of TiO_2 NPs (Figure 9a, solid line) shows clear contributions from two distinct species, referred to as 1-C and 1-OB (for closed-unbound and open-bound to TiO_2, respectively), with absorption peaks (Abs_{max}) at ~519 and 471 nm, respectively. The presence of the TiO_2 NPs is confirmed by the strong absorption in the UV region (below 360 nm); see Figure 9a, solid and dotted lines. The corresponding fluorescence excitation spectrum (Figure 9a, dashed line) indicates that 1-C is the species that contributes predominantly to the observed fluorescence. The absorption and fluorescence excitation spectra of the control sample without TiO_2 NPs (Figure 9b) show that 1-C is the only species present in the absence of TiO_2 NPs. Note that in this case the strong TiO_2 absorption in the UV region is not observed.

Analogous preparation and analysis using perylene 2 shows similar results (Figure 9c and d). In this case, the observed shift (~25 nm) is significantly smaller than that observed in ethanol upon full basic hydrolysis (~134 nm); this difference could be explained considering only partial hydrolysis of the dye in the TiO_2–micelle microemulsion. Thus, the spectra with peak absorption at ~690 and 665 nm are assigned to the anhydride (closed, 2-C) and partially hydrolyzed (open bound, 2-OB, i.e., only one anhydride group is hydrolyzed) forms of 2, respectively. Evidence for the putative partial hydrolysis of 2 in ethanol is shown as a small shift in the absorption and emission spectra upon addition

of a few equivalents of KOH; see Figure 5c (blue dash-dotted line). As mentioned before, the lack of an isosbestic point in Figure 5c suggests the presence of more than two interconverting species for 2.

The absorption and emission spectra of 3 did not show significant changes in TiO_2–micelle vs empty micelle microemulsions, as shown in Figure 9e and f. The lack of spectral shift and low emission quenching suggest that the dye does not open and bind to the oxide and consequently cannot effectively photoinject an electron in its conduction band. The deficient binding of the dye is rationalized as a consequence of the bulky 4-*tert*-butylphenyloxy groups which create a strong steric hindrance for the insertion of the dye through the micelle structure to reach the TiO_2 NP surface. Analysis of the calculated molecular structure for the dyes supports this interpretation, indicating that the largest molecular dimension (D) across the perylenes' bay substituents varies in the series as D1 (9 Å) < D2 (13 Å) < D3 (27 Å); see Figure S3b in the Supporting Information.

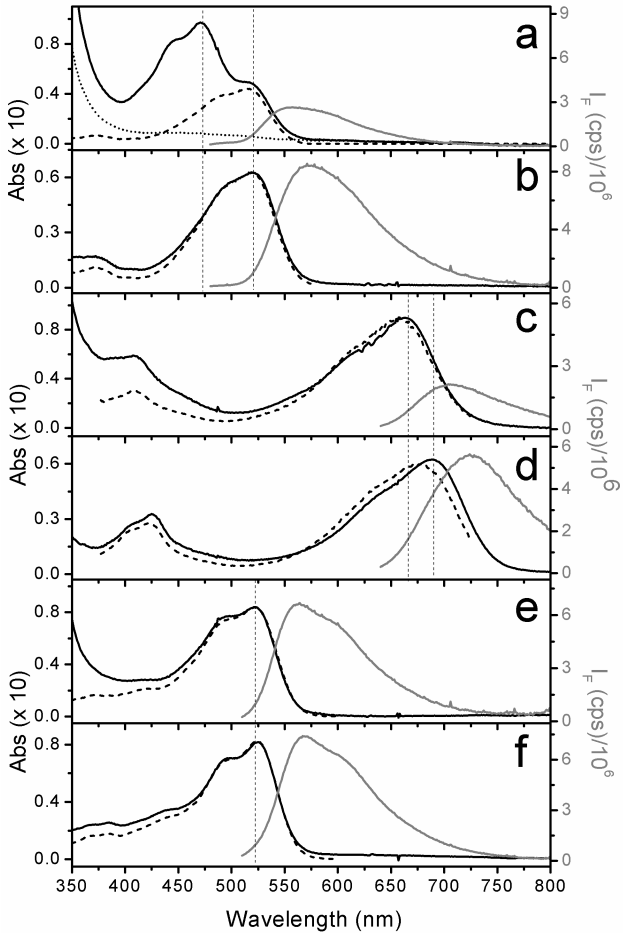

Figure 9 – Absorbtion and emission spectra of perylenes in micelle microemulsion with and without TiO_2

(a) Absorption (solid black), emission (solid gray), and normalized excitation spectra (dash) of perylene 1 in a microemulsion containing TiO2 NPs and absorption of a microemulsion containing TiO2 NPs (dotted line) but not the dye. (b) Same as part a but for a microemulsion without TiO2. (c, d) Same as parts a and b, respectively, for perylene 2. (e, f) Same as parts a and b for perylene 3. Excitation spectra were recorded with emission at 578, 735, and 610 nm for (a, b), (c, d), and (e, f), respectively. Emission spectra were recorded with excitation at 470, 630, and 495 nm for (a, b), (c, d), and (e, f), respectively. Emission spectra intensities were corrected as described in the experimental section. Vertical dotted lines show absorption maximum in microemulsions with and without TiO2 NPs for each dye.

Steady State Absorption and Emission Spectra and Emission Anisotropy

Steady state fluorescence anisotropy measurements were performed to gain insight on the location of the dyes in micellar suspensions. Table 2 shows that the fluorescence anisotropy of 1, 2, and 3 is considerably higher in micellar suspensions than in the low viscosity solvent THF, indicating that the movement of the dye is significantly restricted and suggesting that it is preferentially located in the ordered micellar environment. This preferential location of the dye generates a relatively high local concentration of the dye in the micellar environment which presumably facilitates the binding of dye to the adjacent oxide surface in solutions of micelles with TiO_2 NPs. Under these conditions, the fluorescence of 1 and 2 in the TiO_2–micelle suspension is highly reduced (~70% quenched for 1-TiO_2 and 2-TiO_2 compared to the corresponding control samples without TiO_2). In the case of the 1-TiO_2 system, the emission is dominated by the spectrum of the closed anhydride species of the dye (Scheme 1, C), while the absorption spectrum has a major contribution corresponding to the open bound species (OB). The lack of significant emission corresponding to the OB species suggests an efficient fluorescence deactivation pathway by electron injection from photoexcited dye into the TiO_2 conduction band (see Scheme 2). The remaining emission of the 1-TiO_2 system, which is presumably from the nonbound C species located in the micellar environment, is more polarized than that of 1 in the micelle without TiO_2. This indicates that the TiO_2 NP restricts the movement of the nonbound dye presumably by creating a more rigid micelle due to the strong electrostatic interaction of the positively charged TiO_2 surface and the negatively charged sulfonate

group of the surfactant. Similar observations were found for the 2-TiO_2 system, although it is difficult to discriminate the contribution of the C species and partially OB species due to the relatively small spectral shift in their emission spectra. The shape of the fluorescence excitation spectra of the 2-TiO_2 system is in between the absorption spectra of the 2-TiO_2 and 2-micelle systems, indicating a significant contribution of both the C and OB species to the observed fluorescence. In the case of the 3-TiO_2 system, the emission spectrum is dominated by the emission of the C species and the steady state emission anisotropy measurements in different environments show similar trends to the other perylene systems, but not so marked. This observation is consistent with the dye being located in the outer layer of the micellar structure but not close enough to attach to the TiO_2 surface.

Table 2 – Steady State Fluorescence Anisotropy (r) of Perylene Dyes in Different Environments[a]

	THF	micelle	micelle/TiO_2
1	0.004 (0.002)	0.12 (0.01)	0.24 (0.01)
2	0.011 (0.001)	0.15 (0.02)	0.33 (0.03)
3	0.015 (0.007)	0.04 (0.01)	0.21 (0.01)

[a]Anisotropy was measured in an L-format geometry spectrofluorimeter. The reported numbers are the average and the standard deviation (in parentheses) of the values obtained over the 520–610, 710–770, and 550–640 nm spectral ranges for 1, 2, and 3, respectively.

Time Resolved Fluorescence Anisotropy

Figure 10 shows the fluorescence anisotropy decays of dyes 1, 2, and 3 in different environments. The fluorescence anisotropy decay of 1 in heptane can be fitted with one fast decay lifetime of 81 ps. However, when 1 is dissolved in a micelle solution (control sample), the anisotropy shows a biexponential decay with components of 81 ps (2%) and 1.67 ns (98%). The 81 ps component is associated to the rotational correlation time of 1 in the heptane, whereas the 1.67 ns component could be associated to the rotation of the dye within the surfactant layer of the micelle. Alternatively, the 1.67 ns component can be associated to the rotation of the whole dye–micelle assembly (the decay closely matches the rotational correlation time of a sphere with a diameter of ~3.5 nm in hexane).(83) The anisotropy decay of 1 in a micelle solution containing TiO_2 NPs shows a biexponential decay with a 81 ps (15%) component associated with the free dye in heptane and a longer 2.74 ns (85%) component associated with the rotation of the dye in the restricted surfactant layer or with the rotation of the whole 1-TiO_2/micelle assembly in heptane. Dye 2 shows analogous behavior with slightly larger decay components in all media; this difference is associated with the larger molecular dimension D (see Figure S3b, Supporting Information) of 2 vs 1 which hinders the rotation of 2 relative to that of 1. Dye 3 dissolved in heptane and micelles shows analogous behavior to 1 and 2 but with slightly larger decay components consistent with a larger steric hindrance for rotation due to the bulky *t*-butylphenoxy groups. The anisotropy decay of 3 in micelles with TiO_2 NPs is very similar to that in micelles without NPs. This observation is consistent with the lack of spectroscopic evidence for opening of the anhydride groups and putative binding

to the TiO_2 surface. Overall, the analysis of the time-resolved data shows results in line with those of the steady state anisotropy emission shown in Table 2.

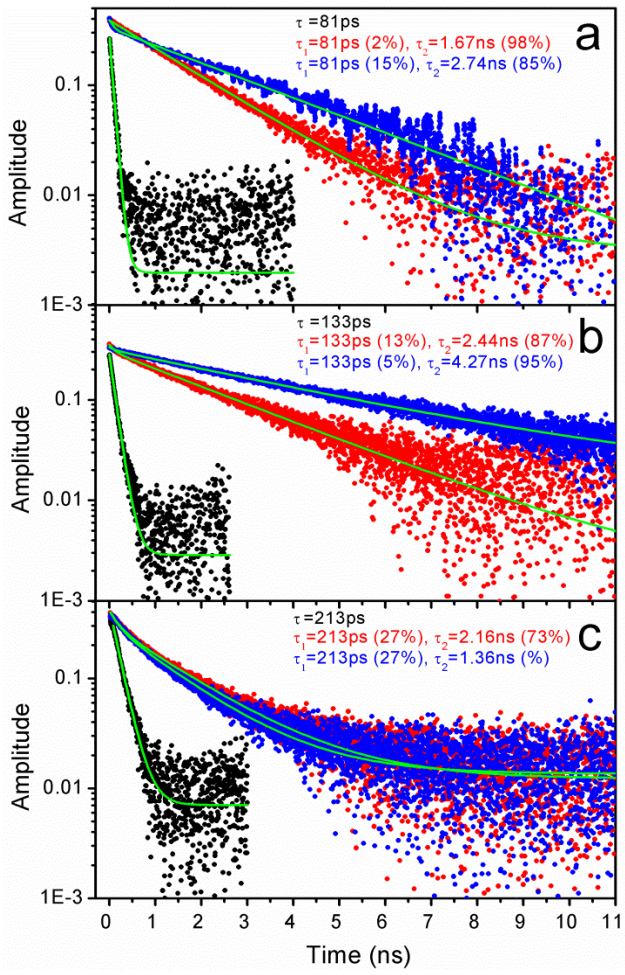

Figure 10 – Fluorescence anisotropy decays
(a) Fluorescence anisotropy decays (data points) of 1 in heptane (black), micelle solution (red), and TiO2–micelle solution (blue). Smooth lines show exponential fits to the data. Samples were excited and emission collected at the following wavelengths: heptane and micelle: λex = 520 nm, λem = 600 nm; 1-TiO2: λex = 420 nm, λem = 510 nm. (b) Same as part a but for dye 2. Heptane: λex = 640 nm, λem = 750 nm; micelle: λex = 640 nm, λem = 750 nm; 2-TiO2: λex = 640 nm, λem = 750 nm. (c) Same as part a but for dye 3. Heptane, micelle, and 3-TiO2: λex = 515 nm and λem = 600 nm. The dye concentration was ~10–6 M for all samples.

Time Resolved Emission

TC-SPC measurements were performed to investigate the nature of the steady state emission quenching observed for the dye–TiO_2 systems. Figure 11a shows the fluorescence decay associated spectra (DAS) of the 1-TiO_2 system. Global analysis of kinetics yields four decay components (χ^2 = 1.14) with lifetimes of 29 ps, 212 ps, 1.09 ns, and 4.28 ns. To a first approximation, the 29 ps component with maximum at 520 nm is associated with the 1-OB (open bound species) and the rest of the components are associated with the 1-C (closed unbound species) in different environments. On the basis of these assignments, the first fluorescence DAS (29 ps) shows energy transfer from 1-OB (open bound species) to 1-C, as indicated by the negative amplitude above 600 nm. The second (212 ps) and third (1.09 ns) components show energy migration in between 1-C species which are in slightly different environments toward the most solvated one, with the lowest energy (4.28 ns component). Overall, the data indicates the existence of a nonhomogeneous system with several dyes per micelle. Analogous measurements on the 1-micelle system (control sample without TiO_2 NPs) show longer lived multiexponential decays (see Figure S4a in the Supporting Information) consistent with the high emission quenching observed for 1-TiO_2 vs 1-micelle in the steady state measurements (*vide supra*).

Figure 11b shows the fluorescence decay associated spectra (DAS) of the 2-TiO_2 system. Global analysis yields four decay components (χ^2 = 1.10) with lifetimes of 487 ps, 2.8 ns, and 5.3 ns. The 487 ps component is associated with the 2-OB (partially open bound

species) and could be assigned in principle to the photoinduced electron injection process from 2-OB to TiO_2. However, some electron injection may occur faster than the instrument resolution (~10 ps) and therefore is non-time-resolved in this experiment. The rest of the components are associated with the 2-C (closed nonbound species) in different environments. Analogous measurements on the 2-micelle system (control sample without TiO_2 NPs) show a longer lived biexponential decay (2.9 and 4.9 ns, see Figure S4b in the Supporting Information) consistent with the high emission quenching observed for 2-TiO_2 vs 2-micelle in the steady state measurements (*vide supra*).

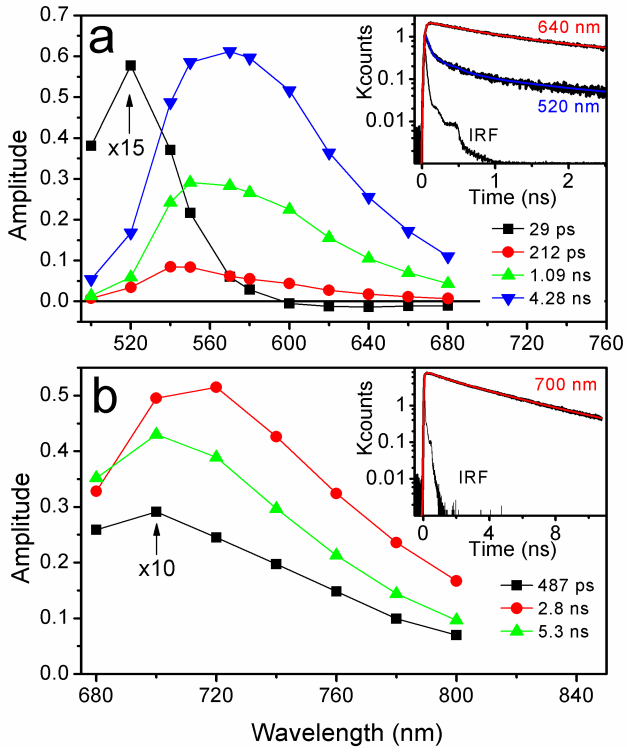

Figure 11 – Fluorescence decay associated spectra
(a) Fluorescence decay associated spectra of the 1-TiO2 system; data was acquired with excitation at 480 nm. Data was globally fitted ($\chi 2 = 1.14$) as described in the experimental section. Inset: kinetic traces and corresponding fits (smooth line) at selected wavelengths and the instrument response function (IRF). (b) Same as part a for the 2-TiO2 system ($\chi 2 = 1.10$). Data was acquired with excitation at 640 nm. The short-lived components were multiplied by a factor to make them clearly visible.

Time Resolved Absorption

Femtosecond pump–probe experiments were performed to establish the kinetics of the photoinduced electron transfer reaction of the dye–TiO_2 system. Figure 12a shows the results for the 1-TiO_2 system; global analysis of kinetics (measured up to 40 ps time delay) shows four decay components with lifetimes of 210 fs, 2.5 ps, 21.5 ps, and 212 ps. The 40 ps time window used in the experiment was chosen to accurately determine the faster components of the decay; the 212 ps component cannot be accurately determined with this window and was fixed in the analysis based on the information provided by the TC-SPC experiments (*vide supra*). The decay associated spectra (DAS) of the 210 fs component can be attributed to the formation of a charge transfer state between 1-OB and TiO_2 (i.e., $1^{\bullet+}$-$TiO_2(e^-)$). It shows decay of stimulated emission and singlet excited state absorption at ~540 and 780 nm, respectively, and formation (negative amplitude) of 1-OB radical cation with characteristic absorption at ~650 nm.(75, 109) The DAS of the 2.5 ps component can be attributed to the decay of 1-C, showing ground state bleaching and stimulated emission at ~500–700 nm and singlet excited state absorption at ~780 nm. This DAS can be associated with the process seen in the fluorescence decays, i.e., energy migration in between 1-C species in different environments. The 21.5 ps component is most likely due to the energy transfer process between 1-OB and 1-C, as seen in the fluorescence decay data (Figure 11a, 29 ps fluorescence DAS). The DAS of the 212 ps component shows a mixture of two main processes: (a) decay of singlet excited state of the 1-C species (as seen in the fluorescence decay data) and (b) decay of the $1^{\bullet+}$-$TiO_2(e^-)$

charge separated state with strong absorption at ~650 nm and weak absorption around 850–1000 nm characteristic of the 1-OB(75, 109) radical cation species and free carrier (injected electrons) in the TiO_2 semiconductor,(110) respectively.

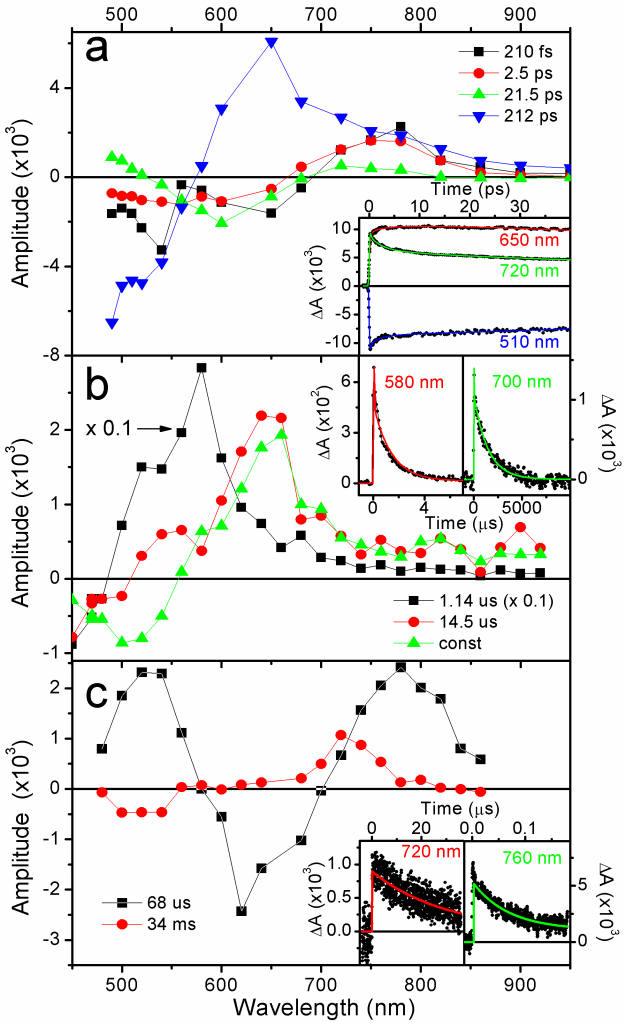

Figure 12 – Decay associated spectra
(a) Decay associated spectra of the 1-TiO2 system measured by pump–probe (fs to ps range). Data was acquired with laser excitation at 460 nm. Inset: kinetic traces (data points) and corresponding fits (smooth lines) at selected wavelengths. (b) Same as part a but measured by flash photolysis (ns to μs range). Data was acquired with laser excitation at 440 nm. (c) Decay associated spectra of the 2-TiO2 system in argon saturated solution measured by flash photolysis (ns to μs range). Data was acquired with laser excitation at 660 nm.

Transient absorption measurements on the 1-TiO_2 system in the nanosecond to millisecond time range were performed to complement the pump–probe data on the faster time scale; the results are shown in Figure 12b. Global analysis of the kinetics shows three decay components: 1.14 μs, 14.5 μs, and a component that does not decay within the 40 ms time window. The 1.14 μs DAS is associated with the decay of triplet excited states of 1-C and 1-OB showing transient absorption in the ~500–650 nm range and ground state bleaching at 450 and 510 nm. The other two DAS are associated with the decay of the $1^{\bullet+}$-$TiO_2(e^-)$ state. They show the characteristic ground state bleaching and induced absorption seen in the pump–probe data (see Figure 12a, 212 ps DAS). The nondecaying transient has ground state bleaching at ~510 nm and is associated with the charge transfer state formed with 1-C most likely due to migration of charge from 1-OB to 1-C. The triplet excited state is not clearly shown in these measurements, since it is most likely quenched due to the presence of molecular oxygen. To determine the lifetime of the nonresolved component, a kinetic trace at 700 nm was recorded up to 10 ms; see the Figure 12b inset. Fitting of this trace yields two decay components of ~15 μs and ~1.5 ms. As mentioned before, both of these components are consistent with the decay of $1^{\bullet+}$ species.

Flash photolysis measurements on the 2-TiO_2 system in argon saturated solution are shown in Figure 12c. Global fit to the data yields two components: a long-lived component of 34 ms assigned to the decay of the $2^{\bullet+}$-$TiO_2(e^-)$ charge transfer state and a

68 μs DAS assigned to 2-OB and 2-C triplet states. Measurements in air saturated solutions (see Figure S5 in the Supporting Information) show only one DAS of 30 ms assigned to the $2^{\bullet+}$-$TiO_2(e^-)$ state with spectral features very similar to the long decay measured in argon. The transients in the 520–700 and 640–820 nm regions correspond to the 2-OB ground state absorption recovery and the 2-OB radical cation absorption decay, respectively.

Attempts to determine the formation rate of $2^{\bullet+}$-$TiO_2(e^-)$ at short time scales using the pump–probe technique showed only features associated with the excited state decay (see Figure S6, Supporting Information). The lack of radical cation absorption at early times is probably due to the long lifetime of the $2^{\bullet+}$-$TiO_2(e^-)$ state which precludes the recovery of the 2-TiO_2 system ground state in the time between laser pulses (2 ms, pulse frequency = 500 Mz) coupled to slow sample mixing due to the high viscosity of the solutions. Rigorous analysis of time-resolved emission and absorption data in a non-homogeneous system requires the use of a model which considers a distribution of exponential decays to describe the kinetics of each transient species. The distribution of decays accounts for the distribution of available environments in the heterogeneous system. In our analysis, we used the minimum number of exponential components that adequately fitted the experimental data within the experimental error. Thus, it is likely that the reported decay components correspond to a weighted mean value of the actual distribution of constants associated with each species.

Distribution of Dyes in the Micellear Solution

To better understand the dye–TiO_2 assembly process, it is useful to discuss the expected distribution of dyes in micellar systems. The distribution of nonreacting dyes (i.e., in anhydride form) in a micelle microemulsion can be calculated from the concentration of dye and micelles (C_{dye} and C_m, respectively) assuming Poisson statistics,(111) as shown in eq 4:

$$P_n = \frac{\lambda^n \cdot e^{-\lambda}}{n!} \tag{4}$$

where P_n is the probability of finding n dyes in a given micelle and $\lambda_m = C_{dye}/C_m$ is the average number of dyes per micelle. In our experiments, $\lambda_m > 10^{-3}$ (see the Supporting Information); thus, the probability of finding two (or more) dyes in a given micelle is less than one in a million. On the other hand, considering that $\lambda_{NP} = C_{dye}/C_{NP} \sim 0.77$ (see the Supporting Information) and assuming that the dyes are distributed exclusively among micelles that contain TiO_2 NPs, the probability of finding two and three dyes per NP are $P_2 \sim 0.14$ and $P_3 \sim 0.03$, respectively. Comparison of $C_m \sim 10^{-3}$ M and $C_{NP} \sim 1.3 \times 10^{-6}$ indicates that in the TiO_2–NP microheterogeneous solutions a large fraction of the total micelles does not contain TiO_2 NPs. The results of these calculations and the evidence for dye aggregation shown in the time-resolved experiments (*vide supra*) suggest that in the equilibrated 1-TiO_2 and 2-TiO_2 systems the dyes are preferentially located in the small

fraction of the micelles that contain TiO_2 NPs rather than being statistically distributed among all the available micelles. This preferential dye location can be explained considering the following mechanism. At early times after dye addition, the dyes are statistically distributed among all the available micelles in the solution by micelle-collision mediated dye exchange. When a dye reaches a micelle containing a TiO_2 NP, it can attach to the oxide surface and it is longer available to be exchanged with other micelles on subsequent collisions. Eventually, all nonbound dyes "find" micelles containing a TiO_2 NP and attach to them. The slow equilibration process shown in Figure 8a,b could in principle be evidence of the proposed mechanism.

Photoiduced Electron Transfer

The spectroscopic results discussed above show evidence that both the 1-TiO_2 and 2-TiO_2 systems undergo photoinduced electron transfer to yield the dye–TiO_2 charge separated state. Global analysis of pump–probe and flash photolysis results indicate that the apparent forward and backward rate constants for the formation and decay of the $1^{\bullet+}$-$TiO_2(e^-)$ state are $k_F \sim 4.8 \times 10^{12}\ s^{-1}$ (1/210 fs) and $k_B < 6.9 \times 10^{4}\ s^{-1}$ (1/14.5 μs), respectively. On the other hand, as it was mentioned above, it was not possible to measure by pump–probe the k_F of the $2^{\bullet+}$-$TiO_2(e^-)$. TC-SPC results for this system show a fluorescence decay with relatively slow components; the shortest decay component of ~490 ps for 2*-TiO_2 might in principle be associated with the formation of the $2^{\bullet+}$-$TiO_2(e^-)$; however, due to the limited time resolution of the TC-SPC experiment, there is

most likely a much faster unresolved fluorescence decay component associated with photoinduced electron injection on a shorter time scale (<10 ps). Formation of $2^{\bullet+}$-$TiO_2(e^-)$ was confirmed by flash photolysis experiments showing clear features of charge separated state that decayed on a very long time scale, $k_b = 33\ s^{-1}$ (1/30 ms). For the 3-TiO_2 system, the spectroscopic studies indicate that the dye does not bind to the TiO_2 NPs and show no evidence of photoinduced electron injection. Thus, in the following analysis only, the 1-TiO_2 and 2-TiO_2 systems will be considered.

The experimentally determined electron transfer rate constants can be discussed in terms of eq 5 and similar equations that have been developed to describe electron transfer from a single donating state to a continuum of accepting states, such as those present in the conduction band of TiO_2 nanoparticles.(1, 98, 112-115)

$$k_{F(eT)} = \frac{2\pi}{\hbar}\int_{-\infty}^{\infty}\rho(E)\left|\bar{H}(E)\right|^2\left(4\pi\lambda k_B T\right)^{-1/2} e^{-\frac{(\lambda+\Delta G^0+E)^2}{4\lambda k_B T}}$$

(5)

where ρ(E) is the effective density of states at the energy E relative to the conduction band edge, $f(E)$ represents the Fermi distribution function, $\bar{H}(E)$ is the average electronic coupling between the dye excited state and all k states in the semiconductor, and λ is the total reorganization energy. ΔG^0 is the energy difference between the energy level of the excited dye and the bottom of the conduction band and can be written as $\Delta G^0 = E_{CB} - E(D^+/D^*)$. To a first approximation, $\bar{H}(E)$ and λ are assumed to be the same for all the dye–TiO_2 systems given the analogous structure of the dyes and their expected identical

binding modes to the TiO_2 surface. Under these approximations and given that $E(2^+/2^*) > E(1^+/1^*)$, the rate constants for forward electron transfer are expected to follow the relationship $k_F(2) > k_F(1)$. The previous analysis suggests that the ~490 ps fluorescence quenching component seen on the 2-TiO_2 system is not due to the formation of the $2^{\bullet+}$-$TiO_2(e^-)$ state and that $k_F(2) > 4.8 \times 10^{12}\ s^{-1}$.

Models for k_B generally involve semiconductor effects such as charge trapping and transport which are not well-defined in our system, so no detailed analysis will be carried out for this case. It is noteworthy to mention that approaches entirely based on quantum-chemical calculations can be used to estimate dye–TiO_2 electron injection times.(76, 116) Such methods have been successfully applied to the study of perylene–TiO_2 systems with phosphonic and carboxylic acid anchoring groups and various spacer groups(76) and will therefore be interesting to apply to the systems described in this work.

CONCLUSIONS

We report the successful sensitization of TiO_2 nanoparticles inside reverse micelles by perylene dyes. These systems having well dispersed oxide nanoparticles of small diameter (<5 nm) spherical shape and relative narrow size distribution are good models for the study of dye–semiconductor photoinduced electron transfer reactions in solution. Steady state and transient absorption and emission spectroscopy indicate that perylenes 1 and 2 efficiently attach to TiO_2 nanoparticles inside reverse micelles. The binding of the dyes to the oxide surface involves the attachment of dicarboxylic acid groups produced

by hydrolysis of a cyclic anhydride. Binding of perylene 3 to the NPs was inefficient presumably due to steric hindrance resulting from the bulky *t*-butylphenoxy groups connected at bay positions of the dye. The 1-TiO_2 and 2-TiO_2 systems undergo fast photoinduced electron transfer (k_f < 210 fs) to form the dye$^{\bullet+}$–$TiO_2(e^-)$ charge separated state. The electron injected into the semiconductor NP recombines with the dye radical cation on a very long time scale ($k_b(1)$ > 14 μs and $k_b(2)$ = 30 ms).

It is clear from these observations that the molecular structure of the dye plays an important role in the phenomena we observed. In principle, it should be possible to use dyes with the required substitutions to target specific regions of micro-heterogeneous media; it is also possible to modulate the redox potential of the dyes and thereby control electron injection. Therefore, one could use these design parameters to envision applications of molecular systems to sensitize semiconductor nanoparticles located in specific regions of a micro-heterogeneous environment. Additionally, one could imagine other applications in which the dyes are used to map complex landscapes by means of their fluorescence.

Supporting Information

Figures S1–S6 and description for the estimation of the average number of dyes per micelle and per TiO_2 NP. This material is available free of charge via the Internet at http://pubs.acs.org.ezproxy1.lib.asu.edu.

The authors declare no competing financial interest.

ACKNOWLEDGMENT

This work has been supported in part by grants from the Agencia Nacional de Promoción Científica y Tecnológica (ANPCyT), Argentina (PICT 140/08, 2213/07, 2691/11, and PRH23 PME01); the Consejo Nacional de Investigaciones Científicas y Técnicas (CONICET), Argentina (PIP 11220090100839/10, 11220100100284/11, and CIAM/09); the Secretaría de Ciencia y Técnica, UNRC Argentina; the Ministerio de Ciencia y Tecnología Cordoba, Argentina (PID 2010); the National Science and Engineering Research Council (Canada) and a Tomlinson Award, McGill University; the National Science Foundation, USA (DMR-0908656); and the Consejo Nacional de Ciencia y Tecnología, México (CIAM-2008-101939). R.E.P., C.A.C., and S.B. are permanent research staff of CONICET. The research of L.I.H. was supported by the ANPCyT through a Ph.D. scholarship. R.G. thanks the NSERC of Canada for a postgraduate scholarship. D.D.M.-H. is supported by the National Science Foundation Graduate Research Fellowship Program (NSF-GRFP) under Grant No. DGE-0802261 and by the More Graduate Education at Mountain States Alliance (MGE@MSA) Alliance for Graduate Education and the Professoriate (AGEP) National Science Foundation (NSF) Cooperative Agreement No. HRD-0450137. R.E.P. thanks the CSACS of McGill University for a visiting professor scholarship. R.E.P. thanks Juan Palacios for his generous donation of optical components used in this work.

PHOTOINDUCED ELECTRON TRANSFER IN PERYLENE- TIO2 NANOASSEMBLIES†

Manuel J. Llansola-Portoles, Jesse J. Bergkamp, John Tomlin, Thomas A. Moore, Gerdenis Kodis, Ana L. Moore, Gonzalo Cosa, Rodrigo E. Palacios

First published: 8 July 2013

DOI: 10.1111/php.12108

†This article is part of the Special Issue dedicated to the memory of Elsa Abuin.

(This article was adapted with permission from a previously published article: Bergkamp, J. J.; Llansola-Portoles,; Tomlin, J.; Moore, T. A.; Kodis, G.; Moore, A. L.; Cosa, G.; Palacios, R. E. *J. Phys. Chem. B*, 2013, *117* (16), pp 4568–4581 doi: 10.1021/jp3086792. My contributions included synthesis. See Appendix D for permission details)

ABSTRACT

The photosensitization effect of three perylene dye derivatives on titanium dioxide nanoparticles (TiO_2 NPs) has been investigated. The dyes used, *1,7-dibromoperylene-3,4,9,10-tetracarboxy dianhydride* (1), *1,7-dipyrrolidinylperylene-3,4,9,10-tetracarboxy dianhydride* (2) and *1,7-bis(4-tert-butylphenyloxy)perylene-3,4,9,10-tetracarboxy dianhydride* (3) have in common bisanhydride groups that convert into TiO_2 binding groups upon hydrolysis. The different substituents on the bay position of the dyes enable tuning of their redox properties to yield significantly different driving forces for photoinduced electron transfer (P_{eT}). Recently developed TiO_2 NPs having a small average size and a narrow distribution (4 ± 1 nm) are used in this work to prepare the dye-TiO_2 systems under study. Whereas successful sensitization was obtained with 1 and 2 as evidenced by steady-state spectral shifts and transient absorption results, no evidence for the attachment of 3 to TiO_2 was observed. The comparison of the rates of P_{eT} ($k P_{eT}$) for 1- and 2- TiO_2 systems studied in this work with those obtained for previously reported analogous systems, having TiO_2 NPs covered by a surfactant layer, indicates that $k P_{eT}$ for the former systems is slower than that for the later. These results are interpreted in terms of the different energy values of the conduction band edge in each system.

Enhanced Article Feedback

INTRODUCTION

Photoinduced electron transfer (P_{eT}) at dye-semiconductor interfaces plays a central role in a number of technological applications such as solar cells [117-120], light-emitting diodes [121, 122], field effect transistors [123-125], advanced catalytic processes [126, 127], optoelectronic transducers, *etc*. The detailed study of photoinduced processes in

functioning devices is in general complicated by the spatial heterogeneity of the organic–inorganic interfaces at the nanoscale. The large number of possible dye to semiconductor binding geometries (including dye binding modes, nanoparticle size and distribution) and the potential for generation of dye aggregates are some of the main factors that contribute to the heterogeneity of these systems and limit the detailed study of P_{eT} processes.

One of the strategies used to try to understand and minimize the heterogeneity effect is to study electron transfer processes in well-defined model nanoassemblies comprised of organic dyes bound to metal oxide particles in suspension [128-137]. We recently published a study of P_{eT} processes on a system consisting of perylene dyes bound to TiO_2 NPs inside a micellar structure (dye-TiO_2@micelle) [138]. We selected perylene dyes because they are highly photostable and amenable to the tuning of both their redox and their TiO_2 binding properties through chemical functionalization [139-147]. To reduce the size distribution of the inorganic nanoparticles in our previous work, we performed the synthesis of TiO_2 particles inside the water pool of reverse micelles (which function as a controlled size nano-reactor). However, the presence of surfactant groups surrounding the titanium dioxide nanoparticles (TiO_2 NPs) (TiO_2@micelles) hindered the binding of some of the dyes due to steric effects and potentially affected the P_{eT} processes in dye- TiO_2@micelle nanoassemblies due to the electric field generated by the surfactant polar heads and corresponding counterions.

Herein we report on the study of P_{eT} on dye-TiO_2 systems assembled from TiO_2 NPs prepared without surfactant molecules and suspended in an organic solvent. Steady-state and transient absorption results indicate that in these systems a significant portion of dyes 1 and 2 can bind to TiO_2 NPs and undergo P_{eT} whereas dye 3 is observed to not bind to

naked TiO_2. The rate constants for charge injection and charge recombination for dye 1- and dye 2- TiO_2 systems are discussed and compared to those previously acquired with TiO_2 NPs prepared within micellar systems. Advantages and disadvantages for both preparations in terms of the dye-nanoparticle assembly and of charge injection and charge recombination rates are discussed.

MATERIALS AND METHODS

Materials

Titanium tetrachloride (≥97.0%) and dichloromethane (anhydrous, 99.5%) were purchased from Sigma-Aldrich and used as received, all other materials for the preparation of compounds 1, 2 and 3 were the same as reported in reference [138].

Synthesis

Perylenes 1 (*1,7-dibromoperylene-3,4,9,10-tetracarboxy dianhydride*), 2 (*1,7-dipyrrolidinylperylene-3,4,9,10-tetracarboxy dianhydride*) and 3 *1,7-bis(4-tert-butylphenyloxy)perylene-3,4,9,10-tetracarboxy dianhydride* were prepared following literature procedures [138, 146, 148].

Titanium dioxide nanoparticles of (4 ± 1) nm size (see Figure S1) were prepared by a nonhydrolytic condensation method involving the elimination of alkyl halide between metal alkoxides and metal halides [149-151] (M. J. Llansola-Portoles, unpublished). The resulting TiO_2 NPs were dried in ultrahigh vacuum at 25°C for 8 h to remove physisorbed HCl, which was produced in the synthesis, from the surface of the TiO_2 NPs. After drying, the resulting NP powder was added to freshly distilled THF to achieve the desired NP concentration. Small amounts of HCl remain present on the surface of the TiO_2 NPs

(see Supporting Information). Therefore, the NPs zeta potentials kept positive preventing agglomeration and further condensation of the NPs in THF.

Binding of perylenes 1 and 2 to TiO_2 NPs was carried out by addition of 100 μL of a stock solution of the dyes (~10−4 m) in THF to 3 mL of a TiO_2 NP suspension ([TiO_2] = 0.1 g L−1) in THF (for pump-probe experiments dye concentration was increased 10 times in an attempt to maximize the amount of dye attached and thus improve the signal corresponding to dye-TiO_2 assemblies). The system was left incubating for >12 h and absorption spectra were recorded at periodic time intervals immediately after addition of the dye.

Instruments and measurements

Absorption spectra were measured on a Shimadzu UV-3101PC UV-vis-NIR spectrometer. Steady-state fluorescence spectra were measured using a Photon Technology International MP-1 spectrometer, measurements were corrected for the detection system response. Excitation was provided by a 75 W xenon-arc lamp and a single grating monochromator. Fluorescence was collected at 90° to the excitation beam. Fluorescence was detected *via* a single grating monochromator and an R928 photomultiplier tube operating in the single photon counting mode.

Fluorescence decay measurements were performed by the time-correlated single-photon-counting method (TC-SPC). The excitation source was a fiber supercontinuum laser based on a passive modelocked fiber laser and a high-nonlinearity photonic crystal fiber supercontinuum generator (Fianium SC450). The laser provides 6-ps pulses at a repetition rate variable between 0.1 and 40 MHz. The laser output was sent through an Acousto-Optical Tunable Filer (Fianium AOTF) to obtain excitation pulses at desired

wavelength. Fluorescence emission was detected at the magic angle using a double grating monochromator (Jobin Yvon Gemini-180) and a microchannel plate photomultiplier tube (Hamamatsu R3809U-50). The instrument response function was 35–55 ps. The spectrometer was controlled by software based on the LabView programming language and data acquisition was done using a single photon counting card (Becker-Hickl, SPC-830). Fluorescence anisotropy decays were obtained by changing the detection polarization of the fluorescence path parallel or perpendicular to the polarization of the excitation light. The anisotropy decays then were calculated according to Eq. (1), where $I_{VV}(t)$ (or $I_{VH}(t)$) is the fluorescence decay when the excitation light is vertically polarized and only the vertically (or horizontally) polarized portion of fluorescence is detected, denoting that the first and second subscripts represent excitation and detection polarization, respectively. The factor G which is equal to the ratio of the sensitivities of the detection system for vertically and horizontally polarized light can be determined either by so-called tail matching of $I_{VV}(t)$ and $I_{VH}(t)$ or by $I_{HV}(t)/I_{HH}(t)$.

$$r(t) = \frac{I_{VV}(t) - GI_{VH}(t)}{I_{VV}(t) + 2GI_{VH}(t)} \tag{6}$$

The femtosecond transient absorption apparatus consisted of a kilohertz pulsed laser source and a pump-probe optical setup. Laser pulses of 100 fs at 800 nm were generated from an amplified, mode-locked Titanium Sapphire kilohertz laser system (Millennia/Tsunami/Spitfire; Spectra Physics). Part of the laser pulse energy was sent

through an optical delay line and focused on to a 3 mm sapphire plate to generate a white light continuum for the probe beam. The remainder of the pulse energy was used to pump an optical parametric amplifier (Spectra Physics) to generate excitation pulses, which were selected using a mechanical chopper. The white light generated was then compressed by prism pairs (CVI) before passing through the sample. The polarization of pump beam was set to the magic angle (54.7°) relative to the probe beam and its intensity adjusted using a continuously variable neutral density filter. The white light probe is dispersed by a spectrograph (300 line grating) onto a charge-coupled device camera (DU420; Andor Tech.). The final spectral resolution was about 2.3 nm for over a nearly 300 nm spectral region. The instrument response function was *ca* 150 fs.

The nanosecond–millisecond transient absorption measurements were made with excitation from an optical parametric oscillator driven by the third harmonic of a Nd:YAG laser (Ekspla NT342B). The pulse width was ~4–5 ns, and the repetition rate was 10 Hz. The detection portion of the spectrometer (Proteus) was manufactured by Ultrafast Systems. The instrument response function was *ca* 4.8 ns.

All TC-SPC and transient absorption data were globally analyzed using locally written software (ASUFIT) [152] developed under MATLAB (Mathworks Inc.) environment. The model and procedure for global fitting have been described in detail in reference [138]. Decay associated spectra (DAS) obtained from global analysis can have positive or negative amplitudes as a function of wavelength. Positive amplitudes are obtained where absorbance difference signals (ΔA) are: a) positive ($\Delta A>0$) and decreasing (becoming less positive) in time ($\delta(\Delta A)/\delta t<0$) or b) negative ($\Delta A<0$) and increasing (becoming more negative) in time ($\delta(\Delta A)/\delta t<0$). While negative DAS amplitudes occur where ΔA signals

are: a) positive ($\Delta A>0$) and increasing (becoming more positive) in time ($\delta(\Delta A)/\delta t>0$) or b) negative ($\Delta A<0$) and decreasing (becoming less negative) in time ($\delta(\Delta A)/\delta t>0$). These global analysis procedures have been extensively reviewed and random errors associated with the reported lifetimes obtained from fluorescence and transient absorption measurements are typically ≤5%.

Transmission electron microscopy (TEM) were collected using a Philips CM200 TEM at 200 kV/Cs 1.2 mm/PTP Resolution: 0.25 nm/Focused Probe: 0.5 nm/Imaging Modes: TEM/STEM.

Multivariate curve resolution (MCR)

MCR with alternating least squares (MCR-ALS) procedures were applied using a MATLAB-based routine developed by R. Tauler and A. de Juan. The software is available for free at www.ub.es/gesq/mcr/als2004.htm. Non-negativity (measured and estimated absorbances and concentrations in an experiment will always be nonnegative) and closure (sum of concentrations is forced to be equal to a constant value at each stage) constraints were used to obtain a unique solution. More details on the application of the method and program use can be found in the operating manual at http://www.ub.edu.ezproxy1.lib.asu.edu/mcr/als2004/manual.pdf.

RESULTS AND DISCUSSION

Dye structure and energetics

The molecular structures of the perylene derivatives used as sensitizers in this work are shown in Scheme 1a. All dyes have two anhydride groups that are subject to hydrolysis under basic conditions (see Scheme 1b) or in the presence of TiO_2 NPs to yield the corresponding dicarboxylate groups [138]. In their hydrolyzed "open form," the dyes are able to bind to the surface of TiO_2 NPs through the dicarboxylate anchoring group by chemical bonding and/or electrostatic attraction [138, 153, 154] to yield the open, bound dye species. The redox properties of the dyes were tuned by the attachment of electron donating or withdrawing groups at the bay positions. Scheme 1c shows the energy diagram of the dye- TiO_2 system taken from reference [138]. In this diagram, the energy for the conduction band edge (*E*CB) of the TiO_2 NPs was estimated as the flat band potential (V_{fb}) of polycrystalline TiO_2 in water at pH = 2 (V_{fb},W/pH=2 = −0.52 V, *vs* Standard calomel electrode, SCE) to account for the concentration of protons inside the micelle water pool (where the TiO_2 NPs were synthesized) [138, 155]. On the other hand, the TiO_2 NPs used for the experiments described in this work are suspended in a THF solution, which contains trace amounts of acidic water. The *V*fb of TiO_2 in neat THF has been reported as V_{fb},THF = −2.34 V (*vs* SCE) [155]. However, the V_{fb} in nonaqueous solutions is mainly determined by the potential establishment of proton adsorption–desorption equilibrium involving solvent molecules and TiO_2 [155]. As such equilibrium is not possible in nonaqueous aprotic solvents (*e.g.* THF) the V_{fb} value in these solvents is strongly affected by trace amounts of protic impurities (*e.g.* the presence of trace amounts of water leads to significantly positive shifts in V_{fb}) [155]. Considering these factors, the

effective *E*CB value for the TiO_2 NPs used in this study cannot be accurately defined, but it is estimated to fall between −0.52 and −2.34 V (*vs* SCE). As will be discussed, transient-absorption experiments show evidence for P_{eT} in 1- TiO_2 and 2- TiO_2 systems indicating that the effective *E*CB in these systems must be only slightly more negative than −0.52 V so that P_{eT} from the dyes excited state to the TiO_2 CB is thermodynamically favorable.

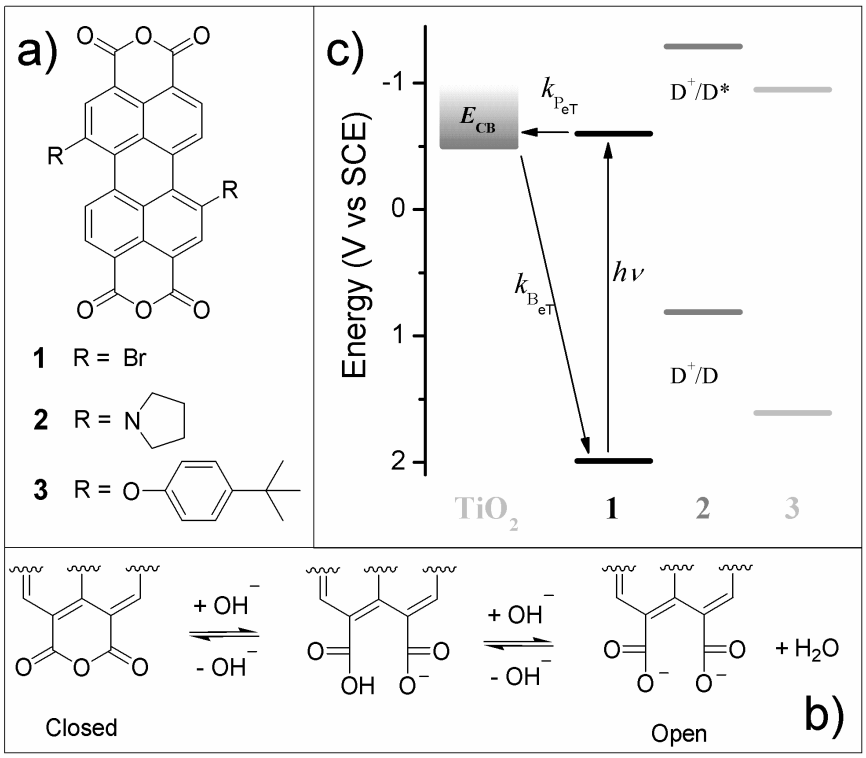

Scheme 3 – Perylene energy diagrams

Dye- TiO_2 nanoassemblies

Steady-state absorption

The binding of the dyes to TiO_2 NPs was followed by monitoring over time the shift of their absorption spectra in the presence of NPs. This is possible because upon opening of the anhydride ring and binding to TiO_2 the absorption spectra of the dyes shift to higher energies [141-143, 146, 156]. This shift can be associated with a reduction in the effective conjugation length of the chromophore [140, 141, 143, 157] and has been previously characterized for the dyes used in this work in ethanolic solution and upon binding of 1 and 2 to TiO_2 [138]. Figure 13 shows the absorption spectra as a function of time following addition of dye to a TiO_2 NP suspension in THF. For the 1-TiO_2 system a significant absorbance shift was observed after 12 h (Fig. 1a) indicating that binding of the dye is slow under the studied conditions. In contrast, significant changes in the absorption occurred within 30 min for the 2-TiO_2 system (Fig. 1b, inset). The magnitude of the absorption shift (~70 nm) observed upon incubation of dye 2 with surfactant-free ("naked") TiO_2 NPs (2-TiO_2) is significantly larger than that previously observed upon incubation with TiO_2 NP covered by a layer of surfactant molecules (2-TiO_2@micelle) (~24 nm) [138]. In addition, the absorption shift observed for the 2- TiO_2 system is similar to that previously observed upon exhaustive basic hydrolysis of dye 2 in ethanol solution (where presumably both anhydride groups are hydrolyzed yielding a maximum absorption shift of ~130 nm) [138]. These observations are consistent with the idea that binding of dye 2 to naked TiO_2 NPs can occur at least partly through both dicarboxylic acid groups (product of the hydrolysis of both anhydride rings) whereas dye 2 binds to TiO_2@micelle NPs *via* one dicarboxylic acid moiety (resulting from hydrolysis of only

one anhydride ring). The surfactant molecules on the TiO_2@micelle NPs presumably preclude the formation of dye-NP geometries where both anhydride rings are close enough to the NP surface (and/or remaining water pool) to hydrolyze and bind simultaneously. Thus, dye-NP binding geometries involving both dicarboxylic groups in one particle and others where the dye acts as a bridge between two NPs are in principle possible for naked TiO_2 NPs, but very unlikely for TiO_2@micelle NPs.

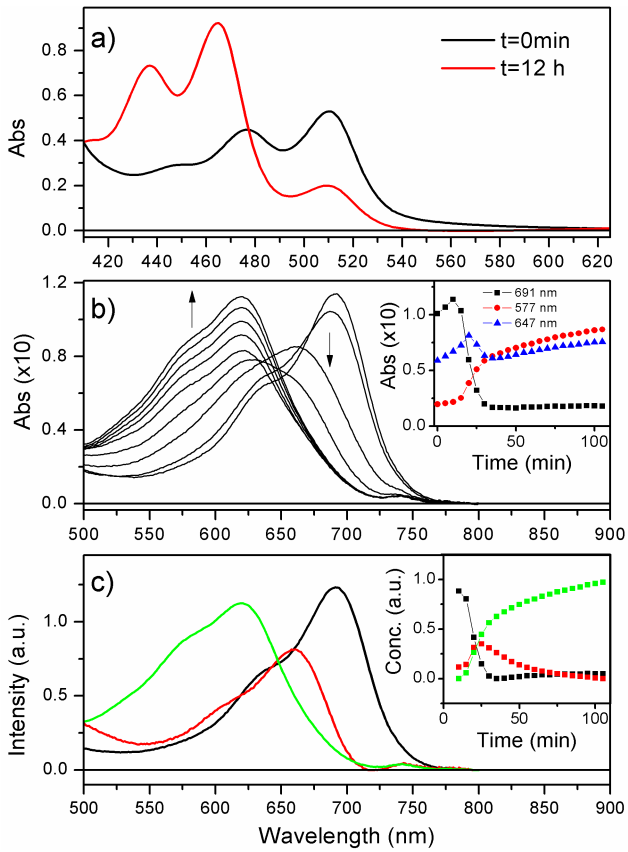

Figure 13 – Absorbtion spectra of perylenes as they attach to TiO_2 nanoparticles
(a) Time sequence of absorption spectra collected after addition of 1 to a suspension of titanium dioxide nanoparticles in THF. [Dye] = ~10−6 m, estimated
[NP] = ~0.1 mg mL−1. (b) Same as (a) for dye 2. The first and last spectra were collected at 0 and 105 min, respectively. The inset displays kinetic traces at specific wavelengths. (c) Species spectra obtained by multivariate curve resolution analysis of data in (b). The inset shows the concentration time evolution for each species (line style coded).

To identify the spectra of the different species present upon hydrolysis and subsequent binding of 2 to TiO_2 NPs we used MCR techniques. Analysis of the absorption spectra time sequence shown in Fig. 1b using the MCR-ALS method [158] is shown in Fig. 1c. The results indicate the presence of three species with distinct peak absorptions at 691 nm (Species A), 658 nm (Species B) and 620 nm (Species C) that can be in principle associated with the hydrolysis of none, one and both anhydride rings, respectively. The inset shows the concentration of each species as a function of time indicating a stepwise interconversion between species, *i.e.* A ↔ B ↔ C. The assignment of A, B and C species to the closed, mono-hydrolyzed and di-hydrolyzed dye species is further supported by MCR analysis of data corresponding to the basic hydrolysis of 2 in ethanol (see Figure S2a), which also shows the presence of three interconverting species (driven by basic titration) with spectral features analogous to the species shown in Fig. 1C. Similar analysis of the data corresponding to the incubation of dye 2 with TiO_2@micelle NPs [138] yields only two species with peak absorptions at 688 and 664 nm (see Figure S2b) presumably corresponding to the closed and mono-hydrolyzed species.

In contrast to the spectral shift observed for 1 and 2 in the presence of TiO_2 NPs, the absorption spectrum of dye 3 did not significantly shift over time under the same conditions (see Figure S3). This result suggests that dye 3 does not bind to naked TiO_2 NPs and thus no additional experiments to investigate P_{eT} were performed with this dye-TiO_2 NP system. Further evidence and discussion for the lack of binding of 3 is given in the time-resolved fluorescence anisotropy section (see below).

Steady-state and time-resolved emission

Recently we reported a large quenching of dye emission (due to P_{eT}) upon binding of 1 and 2 to TiO_2 in a micellar system [138]. Attempts to quantitatively determine dye emission quenching for 1 and 2 in solution by steady-state fluorescence measurements with and without naked TiO_2 NPs failed due to the presence of unattached dyes and of dye aggregates (see time-resolved fluorescence measurements below), which partially dissolve over time and then bind to the TiO_2 NPs.

Time-resolved fluorescence measurements (TC-SPC) were performed to investigate the kinetics of the emission of dyes 1 and 2 in the presence of TiO_2 NPs (see Figure S4a and b, respectively). Results for solutions of 1 incubated with TiO_2 NPs show fluorescence decay-associated spectra (DAS) with three components of 100 ps, 850 ps and 3.9 ns ($\chi^2 = 1.18$). The 100 and 850 ps components could be associated with dye aggregates where the dye is in the closed form suspended in solution and showing significant autoquenching. It is well known that perylenes are prone to aggregate and crystallize to afford typically weakly luminescent particles [159, 160]. The main driving force for aggregation comes from strong intermolecular π–π-stacking interactions resulting from the extended π-system and large quadrupole moment of perylenes. The most likely fluorescence quenching mechanisms in these putative aggregates are: (1) enhancement in the rate of internal conversion to the ground state due to increased coupling of electronic excitation to lattice vibrations, (2) exciton (dipole–dipole) interactions and (3) efficient energy transfer to nonemitting defects or impurities [161, 162]. Alternatively, the 100 and 850 ps components could be associated with the emission of the dye when physisorbed on the surface of NPs in its closed form and thus with a low electronic coupling for P_{eT}.

The 3.9 ns component is associated with the emission from 1 in its closed form and nonaggregated in solution. On the other hand, the fluorescence DAS of solutions of 2 incubated with TiO_2 NPs yielded two fluorescence DAS components ($\chi 2 = 1.12$) with lifetime of 71 ps and 2.5 ns. The 71 ps component with maximum at 740 nm could be associated with aggregates of 2 closed species, which show a short fluorescence lifetime due to autoquenching. The 2.5 ns component is associated with 2 in its closed form and nonaggregated in solution.

Time-resolved fluorescence anisotropy

To further investigate the diffusion rotational properties of the emitting species in the studied samples we performed time-resolved fluorescence anisotropy measurements. Figure 14 shows time-resolved fluorescence anisotropy decays of the dyes in THF solutions with and without the addition of TiO_2 NPs. As seen in Fig. 2a, the decay of dye 1 in solution can be fitted with a single exponential lifetime of 115 ps similar to that observed in n-heptane (81 ps) [138]. In the presence of TiO_2 NPs, the anisotropy decay can only be satisfactorily fitted with two exponential components (115 and 890 ps). The shorter component can be associated with the reorientation dynamics of free dye in solution or energy transfer among dyes in aggregates since both situations are possible and create a fast depolarization effect in the emission. The 890 ps component can be ascribed to the presence of dye molecules physisorbed on the surface of TiO_2 NPs or covalently bound to surface defects such that the effective dye-TiO_2 electronic coupling (H) for P_{eT} is very small and consequently the dye fluorescence is not significantly quenched. These putative dye-TiO_2 assemblies are significantly larger than a free dye in solution and consequently have much slower reorientation dynamics. To test this, we

calculated the radius of a sphere with an 890 ps rotational correlation time in THF (see Supporting Information); the obtained value, r = 1.2 nm, is in close agreement with the size of our TiO_2 NPs (diameter 4 ± 1 nm). An analogous situation, but with longer time constants, is observed for dye 2 (see Fig. 2b). The free dye in solution shows a mono-exponential decay with a lifetime of 253 ps and in the presence of NPs it shows a biexponential decay with 253 ps and 1.36 ns components. These results are consistent with the larger molecular size of 2 *vs* 1 [138] and consequently slower reorientation. In contrast to this, dye 3 shows fast mono-exponential decays for both situations, the free dye in solution (265 ps) and in the presence of TiO_2 NPs (188 ps) (see Fig. 2c). The results indicate that dye 3 does not exhibit physisorption or bind to TiO_2 NPs which is consistent with the lack of absorption shift observed when the dye is incubated in the presence of NPs (see Figure S3). The lack of binding of dye 3 to TiO_2@micelles NPs was previously reported by our group and rationalized invoking strong steric interactions between surfactant molecules and the bulky t-butylphenoxy groups of the dye which prevented the formation of geometries where one anhydride ring was close enough to the TiO_2 surface to achieve binding [138]. The new results presented herein indicate that even in absence of micelles in the system, the t-butylphenoxy groups present strong steric hindrance to reach dye- TiO_2 NPs geometries necessary for efficient attachment.

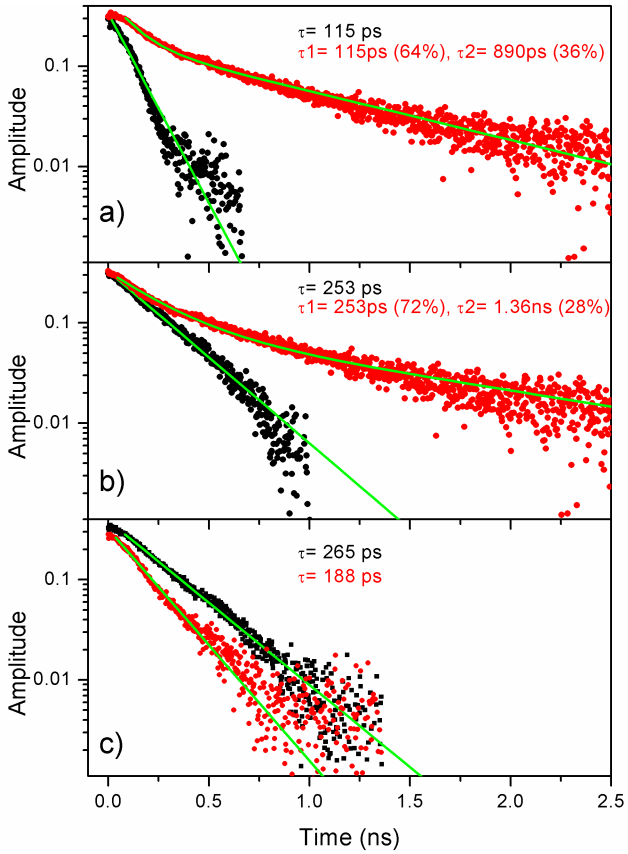

Figure 14 – Fluorescence anisotropy decays
(a) Fluorescence anisotropy decays (data points) of 1 in THF without (circles) and with titanium dioxide nanoparticles (triangles). Smooth lines show exponential fits to the data. Samples were excited and emission collected at the following wavelengths: λ_{ex} = 450 nm λ_{em} = 550 nm. (b) Same as (a) for dye 2: λ_{ex} = 600 nm λ_{em} = 760 nm. (c) Same as (a) for dye 3: λ_{ex} = 450 nm and λ_{em} = 550 nm. Dye concentration was ~10−6 m for all samples.

Time-resolved absorption

Time-resolved transient absorption techniques were used to investigate the kinetics of P_{eT} in the dye-TiO_2 nanoassemblies. Measurements in the femtosecond to nanosecond (pump-probe) and nanosecond to microsecond (flash-photolysis) time ranges were performed in an attempt to measure the kinetics of formation and recombination, respectively, of the dye$^{\bullet+}$-TiO_2 ($e-$) charge separated state.

Figure 15a and c shows pump-probe results for the 1-TiO_2 system with excitation at 490 nm. Global analysis of the kinetic data shows four decay components with lifetimes of ~500 fs, 2.3 ps, 45 ps, and 2.7 ns (see Fig. 3a). The DAS of the 500 fs component can be attributed to P_{eT} from 1 open, bound species to TiO_2 to form the $1^{\bullet+}$-TiO_2 ($e-$) state. The following spectral features support this assignment: (1) decay of stimulated emission (negative amplitude) corresponding to 1 open, bound at ~520 nm (see Figure S5a, red dashed line), (2) formation of 1 radical cation (negative amplitude) with characteristic induced absorption at ~630 nm and (3) formation of free carriers (injected electrons) in the TiO_2 semiconductor (TiO_2 ($e-$)) (negative amplitude) with absorption around 1000 nm. The 2.3 and 45 ps components show a mixture of two main processes: (1) decay of singlet excited state of the 1 closed species (as seen in the TC-SPC data, Figure S4a) and (2) decay of the $1^{\bullet+}$-TiO_2 ($e-$) charge separated state with positive amplitudes at ~630 nm ($1^{\bullet+}$ absorption) and 850−1000 nm (TiO_2 ($e-$) absorption). The last 2.7 ns DAS can be attributed mostly to the decay of singlet excited state of 1 closed form (presumably free in solution), showing ground state bleaching and stimulated emission from ~520 to 570 nm, and induced absorption at 470 and 750 nm.

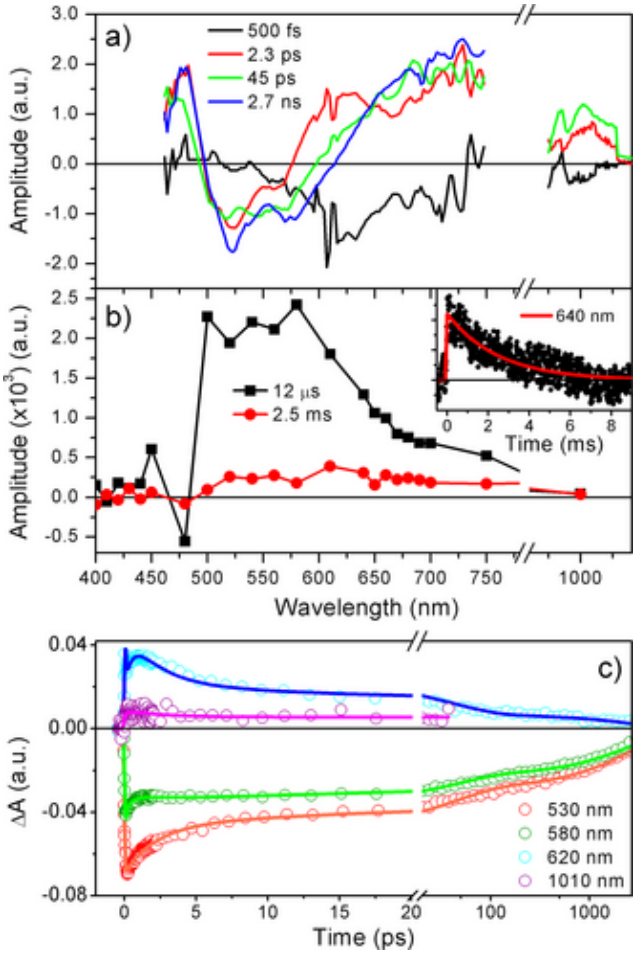

Figure 15 – Decay associated spectra of perylenes at 490 nm
(a) Decay associated spectra of 1-TiO_2 nano-assemblies in THF solution measured by pump-probe (fs to ns range). Data were acquired with pump laser excitation at λ_{ex} = 490 nm. (b) Same as (a) measured by flash-photolysis (ns to µs range) upon λ_{ex} = 440 nm. (c) Kinetics traces (data points) and fits (smooth lines) at selected wavelengths corresponding to the data shown in (a).

Transient absorption measurements on the 1-TiO_2 system in the nanosecond to millisecond time range were performed to complement the pump−probe data; the results are shown in Fig. 3b. Global analysis of the kinetics in argon-saturated solution yields two components, 2.5 ms and 12 μs (excitation at 440 nm). The 2.5 ms component is associated with the decay of the $1^{\bullet+}$-TiO_2 ($e-$) state showing positive amplitude signals around 630 nm ($1^{\bullet+}$ absorption, see kinetic trace in Fig. 3b inset) and up to ~950 nm (TiO_2 ($e-$)). The 12 μs component is oxygen sensitive and it is associated with the decay of triplet excited states of 1 (in open and closed forms) showing transient absorption in the ~500–700 nm range and ground state bleaching at 450 and 520 nm (small dip). Figure 16a and c show pump-probe results with excitation at 650 nm for 2-TiO_2 nanoassemblies. Global fit to the data yields four DAS components of 260 fs, 3.4 ps, 130 ps and 1.9 ns (see Fig. 4a). The 260 fs component is mainly associated with singlet energy transfer from the open form of the dye to the closed one and possibly, to some extent, to the formation of the $2^{\bullet+}$-TiO_2 ($e-$) charge separated state. This component shows the following spectral features: (1) stimulated emission decay (negative amplitude) of 2 open species in the 660–730 nm region (consistent with the red dashed spectra in Figure S5b), (2) formation of stimulated emission of the dye in its closed form with a positive amplitude around 760 nm and (3) $2^{\bullet+}$ transient absorption formation (negative amplitude) above 650 nm. In addition to this, the ground state bleaching of open dye 2 (around 600 nm) decays to some extent with the same lifetime (260 fs) and there is no rise with 260 fs at 1000 nm. Therefore, we do not have strong spectral evidence of $2^{\bullet+}$-TiO_2 ($e-$) formation on the time scales measured. It is likely that charge separation is very fast and occurs in less than 150 fs (instrument response time of our apparatus).

Transient absorption at 1015 nm supports this assumption showing a kinetic trace with instantaneous rise, limited by instrument response (see Fig. 4c, violet data points). The 3.4 ps DAS component is assigned to solvation-induced band-shift of the emission band of 2 closed species. The 130 ps and 1.9 ns components show a mixture of two main processes: (1) recovery of ground state bleaching and stimulated emission of 2 closed species (presumably slightly aggregated and/or physisorbed on the NPs) consistent with its close temporal match to the emission DAS components shown in Figure S4b (71 ps and 2.5 ns) and (2) recovery of ground state bleaching of the open-bound form of 2 (due to recombination of the $2^{\bullet+}$-TiO_2 ($e-$) state) showing negative amplitude in the region around 640 nm.

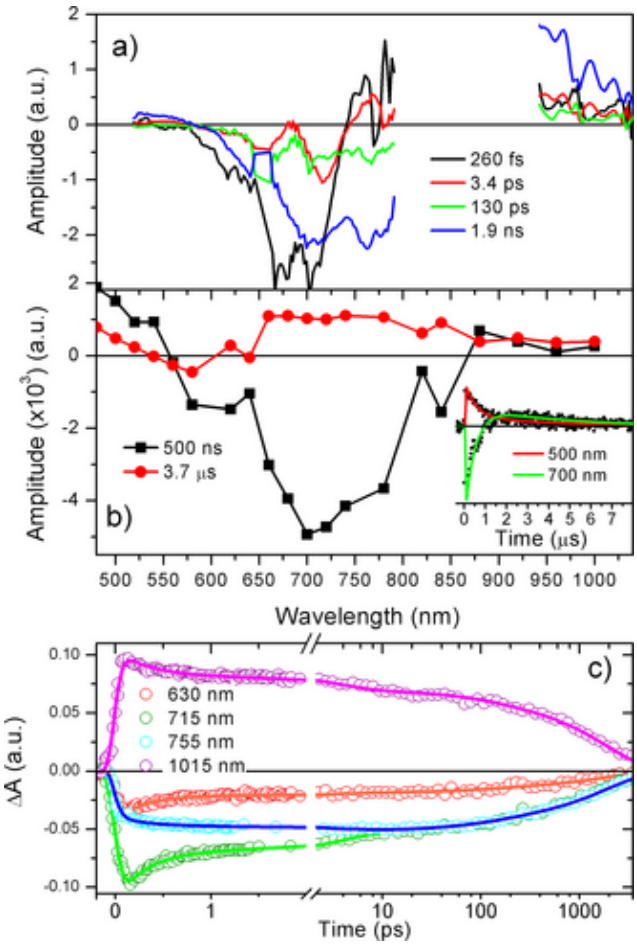

Figure 16 – Decay associated spectra of perylenes at 650 nm
(a) Decay associated spectra of 2-TiO_2 nano-assemblies in THF solution measured by pump-probe (fs to ns range). Data were acquired with pump laser excitation at λ_{ex} = 650 nm. (b) Same as (a) measured by flash-photolysis (ns to µs range). λ_{ex} = 640 nm. (c) Kinetic traces (data points) and fits (smooth line) at selected wavelengths corresponding to the data shown in (a).

Figure 16b shows flash-photolysis results with excitation at 640 nm for the 2-TiO_2 system. Global analysis of the data yields two DAS components of ~500 ns and 3.7 μs. The shorter component is associated with the triplet state of the dye in its closed and open forms showing ground state absorption bleaching recovery (negative amplitude) from 570 to ~800 nm (2 closed species, see Fig. 4a, solid black spectrum) and triplet state transient absorption decay (positive amplitude) below 550 nm. The 3.7 μs component is associated with the decay of the $2^{\bullet+}$-TiO_2 ($e-$) charge separated state. This long component shows ground state bleaching of 2 fully open bound species in the 500–650 nm region (consistent with the solid red spectra, Figure S5b) and $2^{\bullet+}$ transient absorption above 650 nm (consistent with previously reported transient features of $2^{\bullet+}$ [138]).

A comparison of the dynamics of P_{eT} in dye-TiO_2@micelle NPs *vs* dye-TiO_2 systems shows that the P_{eT} rate (kP_{eT} Scheme 1c) for 1-TiO_2 (kP_{eT} [1, naked] = 1/500 fs) is slower than that for 1-TiO_2@micelle (kP_{eT} [1, micelle] = 1/210 fs). On the other hand, for both the 2-TiO_2@micelle and 2-TiO_2 systems, the corresponding kP_{eT} rates are faster than the time resolution of our pump-probe instrument, so no comparison can be made in this case. Regarding the kinetics of recombination of the dye$^{\bullet+}$-TiO_2 ($e-$) state (kB_{eT}, Scheme 1c), kB_{eT} (1, naked) = 1/2.5 ms is slower than kB_{eT} (1, micelle) ~1/1.5 ms and kB_{eT} (2, naked) = 1/3.7 μs is faster than kB_{eT} (2, micelle) ~1/30 ms.

The measured P_{eT} rate constants can be discussed in terms of Eq. (2) [128,163-167], where ρ (E) is the effective density of states at the energy E relative to the conduction band edge (ECB), *f(E)* represents the Fermi distribution function, $\overline{H}(E)$ is the average electronic coupling between the dye excited state and all k states in the semiconductor, λ is the total reorganization energy, and $\Delta G0 = E\mathrm{CB} - E(D^+/D^*)$. To a first approximation

$\overline{H}(E)$ and λ are assumed to be the same for all the dye-TiO_2 systems given the analogous structure of the dyes and their expected identical binding modes to the TiO_2 surface.

$$k_{PeT} = \frac{2\pi}{\hbar}\int_{-\infty}^{\infty}\rho(E)(1-f(E)\,|\overline{H}(E)|^2(4\pi\lambda k_B T)^{-\frac{1}{2}}e^{\frac{(\lambda+\Delta G^0+E)^2}{4\pi\lambda k_B T}}\,dE$$

(7)

As was discussed before, the *E*CB (naked) is more negative than *E*CB (micelle), thus $|\Delta G^0(\text{naked})| < |\Delta G^0(\text{micelle})|$ and $k\text{P}_{\text{eT}}$ (naked) < $k\text{P}_{\text{eT}}$ (micelle) (assuming P_{eT} in the normal Marcus region [52]), which is consistent with the experimental results.

Since models for $k\text{B}_{\text{eT}}$ involve charge trapping and transport effects which are not well defined in our NPs no detailed analysis is presented for this case.

CONCLUSIONS

The main objective of this work was to study the sensitization effect of perylene dyes in surfactant-free TiO_2 NPs with small average size and relatively narrow size distribution in THF. In principle, these particles present the opportunity to construct simple dye-TiO_2 systems, as compared to the previously reported dye-TiO_2@micelle assemblies, to investigate P_{eT} processes. The added surfactant layer in the later systems presumably affects the dye-TiO_2 P_{eT} processes due to the highly directional electric field produced by the surfactant polar groups and corresponding counterions. Thus, in this sense the dye-TiO_2@micelle systems are complex ones characterized by a larger number of variables as compared to the dye-TiO_2 systems used in this study. However, problems related to dye aggregation in THF and the potential formation of dye-NP aggregates in which two NPs can be linked by bridging perylenes (due to its ability to function as bifunctional anchors) created unanticipated complications in the formation of the dye-TiO_2 systems studied

herein. In the case of bridging, the micelle structure provides an organizing scaffold that prevents the formation of NPs aggregates. The results of this study highlight the importance of several factors including solubility, the presence of multiple anchoring groups and steric hindrance of bay groups that affect binding geometries that must be considered in the design of perylene derivative dyes as P_{eT} sensitizers for inorganic semiconductor NPs.

ACKNOWLEDGEMENTS

This work has been supported in part by the National Science Foundation, USA, DMR-0908656 (synthetic studies) and as part of the Center for Bio-Inspired Solar Fuel Production, an Energy Frontier Research Center funded by the U.S. Department of Energy, Office of Science, Office of Basic Energy Sciences under Award Number DE-SC0001016 (transient spectroscopic studies). Additional support was given by grants from the following: the Agencia Nacional de Promoción Científica y Tecnológica (ANPCyT), Argentina (PICT 140/08, 2213/07, 2691/11 and PRH23 PME01); the Consejo Nacional de Investigaciones Científicas y Técnicas (CONICET), Argentina (PIP 11220090100839/10, 11220100100284/11 and CIAM/09); the Secretaría de Ciencia y Técnica, UNRC Argentina; the Ministerio de Ciencia y Tecnología Cordoba, Argentina (PID 033/2010). We also thank funding from the National Science and Engineering Research Council (Canada) and a Tomlinson Award, McGill University. R.E.P. is permanent research staff of CONICET.

METAL-FREE ORGANIC SENSITIZERS FOR USE IN WATER-SPLITTING DYE-SENSITIZED PHOTOELECTROCHEMICAL CELLS

John R. Swierk[a], Dalvin D. Méndez-Hernández[b], Nicholas S. McCool[a], Paul Liddell[b], Yuichi Terazono[b], Ian Pahk[b], John J. Tomlin[b], Nolan V. Oster[b], Thomas A. Moore[b], Ana L. Moore[b],Devens Gust[b], and Thomas E. Mallouk[a,c,1]

Edited by Richard Eisenberg, University of Rochester, Rochester, NY, and approved December 12, 2014 (received for review August 4, 2014)

(This article was adapted with permission from a previously published article: Swierk, J. R.; Méndez-Hernández, D. D.; McCool, N. S., Liddell, P.; Terazono, Y.; Pahk, I.;Tomlin, J. J.; Oster, N. V.; Moore, T. A.; Moore, A. L.; Gust, D.; Mallouk, T. E. *Proc. Natl. Acad. Sci. U. S. A.* , 2015, 112(6), 1681–1686. doi:10.1073/pnas.1414901112. My contributions included synthesis. See Appendix D for permission details)

SIGNIFICANCE

The capture and conversion of sunlight into a useful chemical fuel (H_2, CH_4, CH_3OH, etc.) is a central goal of the field of artificial photosynthesis. Water oxidation to generate O_2 and protons stands as the major bottleneck in these processes. Relatively few stable photosensitizers can generate sufficient oxidizing power to drive water oxidation, and those that do contain rare elements such as ruthenium. In this paper, we show that metal-free organic photosensitizers are capable of driving photoelectrochemical water oxidation. Significantly, these photosensitizers exhibit comparable activity to that of ruthenium-containing photosensitizers under broadband illumination. In addition, we

report to our knowledge the first demonstration of a molecular photosensitizer, outside of natural photosynthesis, that can drive water oxidation utilizing only red light.

ABSTRACT

Solar fuel generation requires the efficient capture and conversion of visible light. In both natural and artificial systems, molecular sensitizers can be tuned to capture, convert, and transfer visible light energy. We demonstrate that a series of metal-free porphyrins can drive photoelectrochemical water splitting under broadband and red light ($\lambda > 590$ nm) illumination in a dye-sensitized TiO_2 solar cell. We report the synthesis, spectral, and electrochemical properties of the sensitizers. Despite slow recombination of photoinjected electrons with oxidized porphyrins, photocurrents are low because of low injection yields and slow electron self-exchange between oxidized porphyrins. The free-base porphyrins are stable under conditions of water photoelectrolysis and in some cases photovoltages in excess of 1 V are observed.

The capture of solar energy and storage as reduced chemical fuels is a significant challenge for a future renewable energy economy. Solar fuels may take the form of H_2 or reduced carbon-containing molecules (CH_4, C_2H_6, CH_3OH, etc.). Large-scale reduction of water or CO_2 requires an abundant electron donor to provide the reducing equivalents. Natural photosynthesis uses water as the electron source, generating oxygen as a byproduct. Most artificial photosynthetic systems also seek to use water as the electron donor, even though the kinetically slow oxygen evolution step is a performance bottleneck (169).

The thermodynamic requirements for water oxidation are relatively modest. A minimum potential of 1.23 V is required, although practical systems need higher voltages because of catalytic overpotentials and series losses in photoelectrolysis cells. This minimum thermodynamic requirement can be satisfied by light of all wavelengths shorter than 1

μm. Allowing for reasonable overpotentials and series losses, the minimum onset for light absorption in a one-photon-per-electron system is near 650 nm, and the maximum theoretical power conversion efficiency is about 20% (170). Although many molecular sensitizers and solid-state semiconductors absorb in this range, finding stable sensitizers with redox or band potentials that span the water oxidation and reduction potentials is a significant challenge.

Light harvesting in natural photosynthesis is accomplished by a hierarchical assembly of accessory pigments that funnel their excitation energy to chlorophyll molecules (171). The core of chlorophyll-*a* is a substituted chlorin (172), a porphyrin ring with a reduced exo double bond (173). Because porphyrins are synthetically more accessible than chlorins and bacteriochlorins, many groups have studied them as light-harvesting molecules in dye-sensitized solar cells (DSSCs) (174, 175). Unlike ruthenium polypyridyl dyes, porphyrins contain only abundant elements and strongly absorb across most of the visible spectrum (176). Grätzel and coworkers recently demonstrated a 12.3% efficient DSSC for electricity generation, using a push–pull Zn porphyrin (177).

In contrast to conventional DSSCs, water-splitting dye-sensitized photoelectrochemical cells (WS-DSPECs) use molecular sensitizers and water oxidation catalysts that are coadsorbed onto a mesoporous TiO_2 electrode. The sensitizer absorbs visible light, injects an electron into the conduction band of TiO_2, and is then re-reduced by the water oxidation catalyst, which oxidizes water to give molecular oxygen and protons. The photoinjected electron migrates through the TiO_2 film to a dark cathode where protons are reduced to molecular hydrogen (168). At high light intensity in the blue part of the

visible spectrum, incident photon current efficiencies (IPCEs) up to 14% have been demonstrated with WS-DSPECs (178).

Earth-abundant catalysts and sensitizers will be needed for large-scale deployment of artificial photosynthesis. Much effort has been devoted to the development of earth-abundant water oxidation catalysts (179–182), including a recently reported completely organic catalyst (183). Less attention has been paid to the development of earth-abundant sensitizers—an important problem for WS-DSPECs where absorber-to-catalyst ratios can exceed 1,000:1. Ruthenium polypyridyl sensitizers are most commonly used in WS-DSPECs (10, 184–187), although Moore et al. (188) demonstrated a WS-DSPEC sensitized with a zinc porphyrin that produced modest photocurrent (~30 $\mu A/cm^2$). Organic sensitizers (containing C, H, N, and O) are earth abundant and offer the possibility of being low cost. The viability of organic sensitizers has been studied in conventional DSSCs (189, 190) and organic solar cells (191, 192), but is largely unexplored in the context of water splitting. Tachan et al. recently proposed type II sensitization with catechol on TiO_2 (193). They observed current enhancement, although the Faradaic efficiency of oxygen generation was not measured and it is unclear how much of the enhancement was specific to visible light sensitization.

In this paper, we demonstrate overall water splitting using metal-free organic sensitizers. We show that a series of free-base porphyrins can drive the photoelectrochemical water-splitting reaction, using only visible light illumination at photocurrents comparable to those of Ru polypyridyl sensitizers. TiO_2 electrodes sensitized with these porphyrins generate photocurrent corresponding to water oxidation, even when illuminated with red light ($\lambda > 590$ nm). Although hole transport and injection yields are poor, back electron

transfer recombination is much slower than it is with the most widely used Ru polypyridyl sensitizer.

METHODS

Detailed syntheses and characterization data for the compounds used in this study, along with additional details of the photoelectrochemical experiments, can be found in *SI Appendix*.

Preparation of WS-DSPEC Electrodes

IrO_2-catalyzed TiO_2 photoanodes were made as described elsewhere (187). An aqueous paste of anatase TiO_2 nanoparticles was applied to an 8-Ω/cm^2 fluorine-doped tin oxide-coated glass slide via a doctor blading technique. After sintering, the electrodes were soaked in 100 μM citrate-capped IrO_x solution for 14 h and then sintered for 3 h at 450 °C to form crystalline IrO_2. Electrical contact was made with a conducting silver paste and protected with Hysol C Loctite white epoxy. The electrodes were then soaked in a 200-μM solution of sensitizer in ethyl acetate for 22 h in the dark, rinsed with fresh ethyl acetate, and stored in the dark.

Characterization of Electrodes

Sensitizer surface coverages on TiO_2 were determined using the Q-band absorbance in solution and on dry TiO_2 films. Emission data were collected on TiO_2 coated with an insulating ZrO_2 shell applied by atomic layer deposition (ALD) via excitation of the Qy(1,0) peak. Photoelectrochemical measurements were made using a 150-W Xe lamp fitted with air mass (AM) 0, AM 1.5, and 410-nm or 590-nm long-pass filters, which prevented band gap excitation of the TiO_2. Short-circuit absorbed photon-to-current

efficiency (APCE) measurements were made with a Metrohm Autolab potentiostat with a 1-ms time resolution. A 470-nm light-emitting diode (LED) (Thorlabs M470L3) was used as the illumination source. Open-circuit photovoltage decay measurements also used the 470-nm LED to provide bias illumination, with a 532-nm pulse (5 mJ, 7–10 ns) from a Nd:YAG laser (SpectraPhysics INDI-40-10) used to pump the system. The voltage decay was monitored on an oscilloscope (Tektronix TDS 540A). The current efficiency for oxygen generation at the photoanodes was measured using a calibrated Pt collector electrode as previously described (186, 187). For each value reported, standard errors were calculated from measurements of six replicate samples. Detailed characterization procedures are reported in *SI Appendix*.

RESULTS

Absorption and Emission Spectra

Free-base porphyrins exhibit a strong Soret band absorption in the near-UV/blue portion of the spectrum and four lower-intensity Q bands at longer wavelengths (194). The Soret bands for the sensitizers studied in this work (Fig. 1) typically had maxima at ~410 nm, with extinction coefficients in excess of 105 $M{-}1{\cdot}cm^{-1}$. As the light source used for photoelectrochemical measurements is equipped with a 410-nm long-pass filter, it is the Q bands of the sensitizers that are of particular importance in this study. *SI Appendix*, Table S1 gives the absorbance maxima and molar extinction coefficients for the Q bands f each sensitizer.

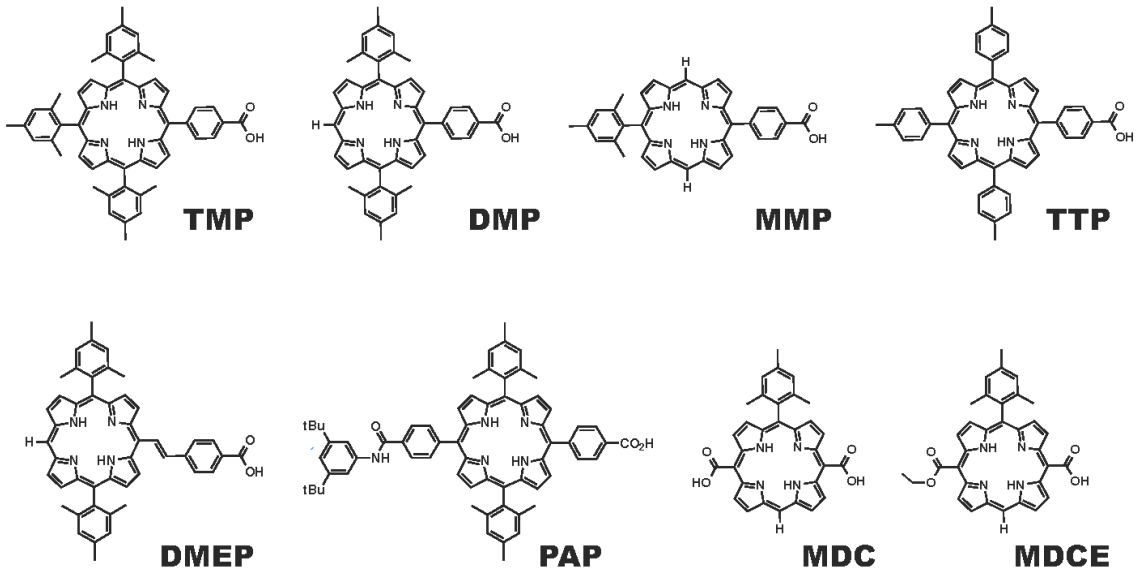

Figure 17 – Free-base porphyrin sensitizers used in this study.
Compound acronyms are defined in *SI Appendix*.

An analysis of the absorbance maxima in *SI Appendix*, Table S1 shows that the position of the Q bands is influenced by the type and number of substituents at the meso positions of the porphyrin ring. TMP, TTP, and PAP have alkylphenyl substituents at each meso position and have nearly identical absorbance maxima. The MMP, DMP, and TMP series exhibits a 6- to 8-nm red shift with each additional mesityl group. With MDC and MDCE, the four Q bands appear at nearly identical positions. Molar extinction coefficients also show some general trends, with fully substituted porphyrins generally having larger values. On the dry, sensitized TiO_2 films, the positions of the Q bands show a slight red shift (~1–3 nm) (*SI Appendix*, Table S2). Typically, the absorbance at the Qy(1,0) peak was between 1 and 2 absorbance units, with the subsequent Q bands following the trends in extinction coefficient measured in solution. The surface coverage (*SI Appendix*, Table S2) was calculated using the absorbance of the Qy(1,0) maximum.

The fluorescence spectra of the porphyrin sensitizers contained two well-defined peaks, the higher-energy emission assigned to the Q(0,0) transition and the lower-energy one assigned to Q(1,0) (Table 1). As in the absorption spectra, the emission maxima shifted to the red as the number of meso-mesityl groups increased from MMP to TMP (*SI Appendix*, Fig. S1). For the fully substituted sensitizers (TMP, TTP, and PAP), the position of the Q(1,0) fluorescence peak was consistent; however, for TTP the Q(0,0) peak (663 nm) was shifted 9 nm to the red relative to TMP and PAP (654 nm). These porphyrins, as well as DMEP, show a mirror image relationship in the relative intensities of the Q(0,0) and Q(1,0) absorption and emission bands.

Table 3 – Properties of dyes
Emission maxima (nm), singlet energy gap (eV), ground state oxidation (E_{ox}) and excited state reduction potentials (E^*_{red}) (V. vs. Ag/AgCl) of sensitizers

Porphyrin	Q(0,0)[a]	Q(0,1)[a]	E(0,0)	E_{ox}	E^*_{red}
TMP	654 (1.0)	721 (0.9)	1.91	1.05	-0.86
DMP	645 (1.0)	710 (1.6)	1.94	1.04	-0.90
MMP	641 (1.0)	702 (1.5)	1.96	1.02	-0.94
DMEP	683 (1.0)	738 (0.6)	1.87	1.18	-0.67
TTP	663 (1.0)	721 (0.8)	1.90	1.18	-0.72
PAP	655 (1.0)	720 (0.8)	1.91	1.29	-0.62
MDCE	677 (1.0)	700 (1.1)	1.92	1.03	-0.89

[a.] Relative intensity of the peaks in parentheses. Emission maxima (nm), singlet energy gap (eV), ground-state peak of anodic wave (E_{pa}), and excited-state reduction potentials (E^*_{red}) (V vs. Ag/AgCl) of sensitizers

Electrochemistry

The peak of the anodic wave (E_{pa}) for the sensitizers on TiO_2 is presented in Table 1. MDC is not included as it rapidly desorbed during the experiment. We determined E_{pa} by cyclic voltammetry (*SI Appendix*, Fig. S2). On TiO_2 the oxidation of the sensitizers was electrochemically irreversible, as previously reported (188). The trends in E_{pa} differed from the observed spectral trends. For example, increasing the number of mesityl substituents introduces a very slight positive shift in E_{pa}, while exerting a more significant effect on the spectral properties. The E_{pa} value for TMP is in close agreement with the value (1.09 V vs. Ag/AgCl) measured by Watson et al. (195). Although TMP, TTP, and PAP have similar spectral characteristics, their Epa values are markedly different, with TMP and PAP separated by 240 mV (*SI Appendix*, Fig. S2).

The excited-state reduction potential E^*_{red} was estimated as the difference between E_{pa} of the ground state and the lowest-energy singlet (E_{00}), determined by the crossing point of the normalized emission and absorption spectra. The porphyrins studied had very similar E_{00} values, so E^*_{red} was largely determined by the position of E_{pa}. E^*_{red} has direct implications for the ability of the excited sensitizer to inject an electron into in the conduction band of TiO_2. For anatase, the conduction band edge potential is about −0.81 V vs. Ag/AgCl at pH 6.8 (196).

In addition to absorbing visible light, the sensitizer must also conduct holes across the surface to a catalytic IrO_2 particle. Intermolecular hole transfer between sensitizers on TiO_2 has been well studied in the context of conventional DSSCs (197-199). Focusing on sensitizers relevant to WS-DSPECs, Hanson et al. (200) measured the cross-surface electron diffusion coefficients (D_{app}) for a series of ruthenium polypyridyl complexes by

polarizing the electrode positive of their formal potential and then monitoring the bleaching of the metal-to-ligand charge transfer (MLCT) absorbance. The absorbance-time curve was fitted to a modified Cottrell equation to give the apparent cross-surface electron diffusion coefficient. Using the same method, we found that D_{app} for the porphyrin sensitizers used in this study was too slow to measure ($\leq 10-11$ $cm^2 \cdot s^{-1}$). By comparison, ruthenium polypyridyl complexes typically have D_{app} values on the order of 10^{-9}–10^{-11} $cm^2 \cdot s^{-1}$ (200, 201).

Photoelectrochemistry

For WS-DSPECs, the photovoltage is defined as the difference between the potential of water oxidation (+0.63 V vs. Ag/AgCl at pH 6.8) and the Fermi level of the TiO_2 under illumination (187). We previously determined the optimal IrO_2 loading to be 0.5 pmol/cm^2 (187). At this loading, we measured open-circuit photovoltages of 1.07 ± 0.01 V and 1.11 ± 0.03 V with the $[Ru(bpy)_2(4,4'\text{-}(PO_3H_2)_2bpy)]$ sensitizer (187, 201). The photovoltages we observed in this study were generally similar and fell between 1.00 V and 1.10 V (Table 2). MDC exhibited a significantly lower photovoltage (0.88 ± 0.01 V); however, it desorbed from the TiO_2 at a significant rate under illumination (*SI Appendix*, Fig. S4). Under red light illumination (AM 1.5 simulated solar spectrum with a 590-nm long-pass filter), a photovoltage drop of ~0.10 V was observed.

Table 4 – Photoelectrochemical data for various sensitizers

Photoelectrochemical data for various sensitizers, open-circuit voltage (mV), integrated photocurrent (mC cm^{-2}), and incident photon to current efficiency (IPCE)

	410 nm long-pass				590 nm long-pass			
Porphyrin	V_{oc}	Integrated photocurrent	IPCE		V_{oc}	Integrated photocurrent	IPCE	
TMP	1045 ± 5	5.1 ± 0.1	0.028 ± 0.005%	±	909 ± 21	0.8 ± 0.0	0.009 ± 0.001%	±
DMP	1088 ± 5	3.7 ± 0.9	0.018 ± 0.005%	±	1004 ± 7	2.5 ± 0.2	0.029 ± 0.002%	±
MMP	1054 ± 17	6.4 ± 0.6	0.032 ± 0.003%	±	910 ± 5	1.6 ± 0.3	0.018 ± 0.003%	±
DMEP	1020 ± 15	7.2 ± 1.5	0.036 ± 0.007%	±	945 ± 16	1.6 ± 0.5	0.019 ± 0.006%	±
TTP	1080 ± 4	5.7 ± 1.0	0.028 ± 0.005%	±	953 ± 12	2.5 ± 0.2	0.030 ± 0.006%	±
PAP	1008 ± 15	2.8 ± 0.8	0.014 ± 0.004%	±	878 ± 15	1.0 ± 0.0	0.011 ± 0.001%	±
MDC	879 ± 12	0.5 ± 0.0	0.006 ± 0.000%	±	700 ± 12	0.1 ± 0.0	0.001 ± 0.000%	±
MDCE	1078 ± 7	6.6 ± 0.3	0.032 ± 0.002%	±	982 ± 14	2.2 ± 0.0	0.025 ± 0.000%	±

We measured the photocurrent at +0.10 V vs. Ag/AgCl applied bias for 10 min under illumination. For ready comparison between sensitizers, we integrated the current to find the charged passed (*SI Appendix*, Fig. S3). For the majority of sensitizers there was little difference in the integrated charge under illumination with a 410-nm long-pass filter (Table 1). PAP and DMP were notable exceptions, passing about half the charge of the other sensitizers. Integrating the photon flux from 410 nm to 700 nm, we calculated IPCE values of 0.014–0.032% for the 10 min of illumination. Under red light (590-nm long-pass filter), the charge passed decreased although IPCE values generally remained constant. Samples that lacked sensitizer or IrO2 showed no measurable photocurrent (<1 $\mu A \cdot cm^{-2}$) with either the 410-nm or the 590-nm long-pass filter. A small transient current that decays within 100 ms can be observed when a sensitizer is present but no IrO_2 is present.

We determined the Coulombic efficiency for oxygen evolution of a TMP-sensitized photoanode (Fig. 2), as previously described (186, 187). When the cell was degassed with Ar, the collector electrode showed a small cathodic background current (~60 μA) before illumination. Once the cell was exposed to light, the photoanode generated photocurrent that was mirrored in time on the collector electrode. Using the collection efficiency (81%) determined by calibration with a Pt film generator electrode, we calculated a Faradaic efficiency of 102 ± 5%, (i.e., near unity) for water oxidation at the WS-DSPEC photoanode.

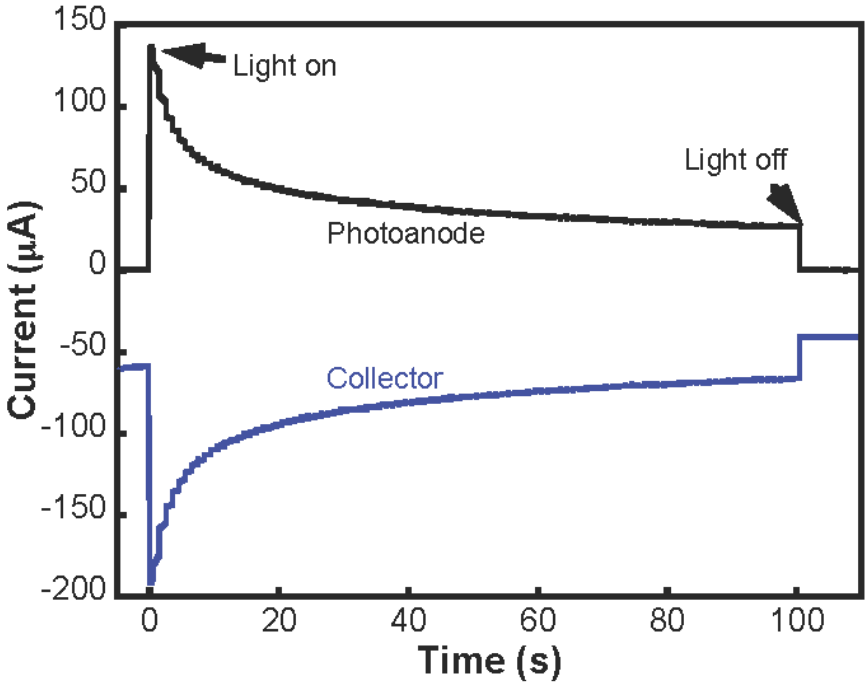

Figure 18 – Collector–generator experiment to monitor O_2 Faradaic efficiency. The generator electrode is a TMP-sensitized photoanode at +100 mV vs. Ag/AgCl, and the collector electrode is a planar Pt film at −640 mV vs. Ag/AgCl (3 M NaCl). Faradaic efficiency is calculated as ~100%, and collection efficiency previously determined is 81%.

To better understand the IPCE values of the various sensitizers on TiO_2, we sought to measure the quantum yield of injection. Meyer and coworkers (202) used a poly(methylmethacrylate) actinometer to measure quantum yields for injection of electrons from excited ruthenium polypyridyl dyes into TiO_2; however, we were unable to accurately determine the molar extinction coefficient of the porphyrin radical cation following injection. Thus, instead of directly determining the injection yield, we measured the APCE under short-circuit conditions. Electrodes with 4-μm-thick TiO_2 films were used to promote efficient charge collection. These films were not functionalized with catalyst, so the APCE was calculated from the photocurrent in the first millisecond of illumination in pH 6.8, 100-mM phosphate buffer. To minimize recombination effects the system was held at short circuit and the measurement was performed over a short time period (1 ms). $[Ru(bpy)_2(4,4'\text{-}(PO_3H_2)_2bpy)]$ was used as a comparison sensitizer, as quantum yields for injection by ruthenium polypyridyl sensitizers are typically high. Table 3 reports the short-circuit APCE values for the sensitizers. Surprisingly, the APCE values in the TMP, DMP, and MMP series were in the reverse order of the overpotential for charge injection. PAP had the lowest APCE value (2.4 ± 0.2%), consistent with its more positive excited-state reduction potential. By contrast, $[Ru(bpy)_2(4,4'\text{-}(PO_3H_2)_2bpy)]$ had an APCE 3–10 times higher than that of the porphyrin sensitizers.

Table 5 – Short-circuit absorbed photon to current efficiency (APCE) and open-circuit photovoltage decay time (ms)

Porphyrin	APCE	t_r
TMP	0.074 ± 0.011	59 ± 5
DMP	0.066 ± 0.005	29 ± 6
MMP	0.031 ± 0.004	25 ± 2
DMEP	0.044 ± 0.002	30 ± 4
TTP	0.052 ± 0.017	38 ± 1
PAP	0.024 ± 0.002	33 ± 1
MDCE	0.038 ± 0.006	59 ± 2
$[Ru(bpy)_2(4,4'\text{-}(PO_3H_2)_2bpy)]$	0.209 ± 0.017	4 ± 1

We also compared the transient open-circuit photovoltage decay rates for each sensitizer and [$Ru(bpy)_2(4,4'\text{-}(PO_3H_2)_2bpy)$] (Table 3). Photovoltage decay curves were fitted to a stretched exponential function to extract the recombination time constant, τ_r (Fig. 3). For the porphyrin sensitizers, values of τ_r were on the order of tens of milliseconds, with some correlation between longer recombination time and the number of substituents. Interestingly, the porphyrins exhibited a τ_r roughly one order of magnitude longer than that of [$Ru(bpy)_2(4,4'\text{-}(PO_3H_2)_2bpy)$]. It is important to note that illumination intensity and not V_{oc} was kept constant for each sensitizer, although V_{oc} values were consistent with values measured under broadband illumination.

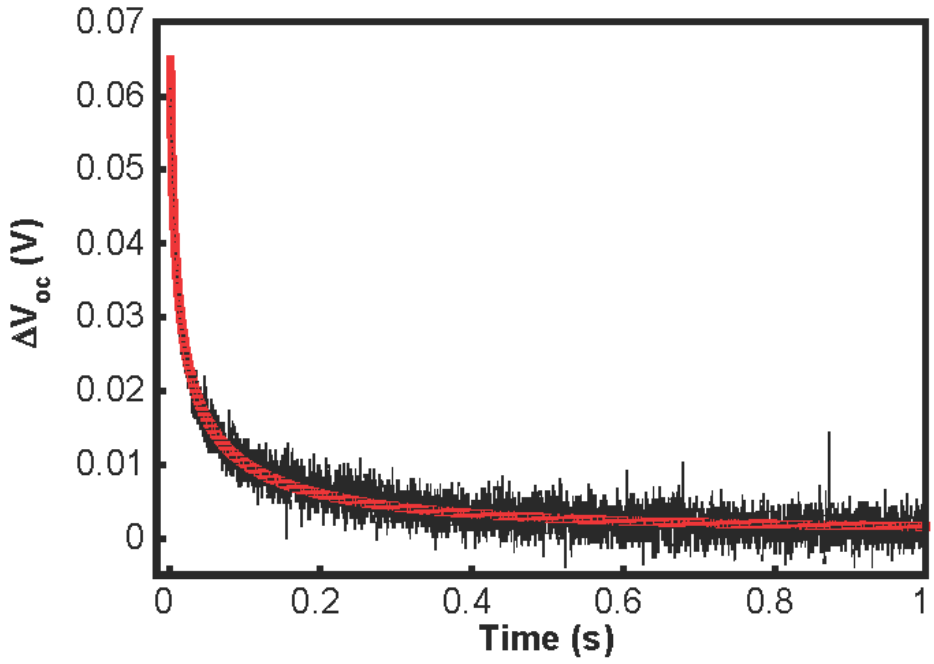

Figure 19 – Representative transient open-circuit photovoltage decay for a DMP-sensitized electrode.
Steady-state bias was provided by a 470-nm LED and the pump was generated by a 532-nm ND:YAG laser pulse (t = 0). Red line, fit to $\Delta V_{oc} = \Delta V_{oc,0} \exp[(\tau/t)^{\beta}]$.

DISCUSSION

The open-circuit photovoltages and integrated photocurrents are quite similar for most of the free-base porphyrin sensitizers. However, a deeper analysis of the spectral and electrochemical properties of the sensitizers reveals significant differences. To properly understand the photoelectrochemical results, it is crucial to understand these differences and to develop a kinetic picture so we can rationally design strategies to improve the system.

Analysis of the spectral and electrochemical data reveals that these properties are directly affected by substitution on the porphyrin core. Symmetry, inductive, and resonance effects may cause these differences. We can observe the effect of symmetry if we compare TMP, DMP, and MMP. Generally, the four-orbital model is used to describe the absorption spectra of porphyrins (194, 203). With free-base porphyrins, the N-H protons on the pyrrole core reduce the overall symmetry of the molecule and split the Q bands into Q_x and Q_y components. This band splitting functionally extends the absorption into the red. Substitution at the meso position shifts the energy of one highest occupied molecular orbital (HOMO) and both lowest unoccupied molecular orbitals (LUMOs). The other HOMO orbital has a nodal plane at the meso position and is unaffected (194). With each additional mesityl group, the molecule becomes more symmetric electronically, the Q bands shift by 6–8 nm to the red, and the molar extinction coefficients increase. Although TMP does not strictly have D_{4h} symmetry, we assume that the aryl groups at each meso position give it quasi-D_{4h} symmetry.

Porphyrin electrochemistry is classically described by the Hammett linear free energy relationship, with the potential of the radical π cation sensitive to the inductive electron

donating/withdrawing character of the substituent and the stabilizing/destabilizing character of any π bonds (204). Inductive effects in this study are hard to elucidate as mesityl, tolyl, and hydrogen are electron-donating groups (204). Resonance between aryl substituents and the π system of the macrocycle core in this study would be expected to stabilize the radical cation.

Resonance stabilization effects can be clearly seen when comparing TMP, TTP, and PAP. From a symmetry standpoint, these compounds are similar with aryl groups at each meso position; the similarity in Q-band absorbance maxima reflects this shared symmetry. Additionally, the inductive effects of the substituents are expected to be similar (204). We might expect TMP to have the least resonance stabilization as steric effects between mesityl and the macrocycle core typically result in a dihedral angle close to 90°. In contrast the aryl groups on TTP and PAP are less hindered and closer to coplanarity with the porphyrin core, thus allowing resonance stabilization effects to cathodically shift E_{pa}. Surprisingly, we see an anodic shift in E_{pa} for TTP and PAP, with TTP shifted by 130 mV and PAP by 240 mV relative to TMP. McLendon and coworkers offer a possible explanation for this behavior (205). In bridged porphyrin adducts, they observe maximum rates of intramolecular electron transfer at 0° and 90°, with the minimum rate near 45°. They attribute this result to orbital symmetry considerations. As we noted, mesityl groups exhibit dihedral angles of ~90°, whereas tolyl groups sit at an angle closer to 60° (206).

The combined effects of substitution on the spectral and electrochemical properties of the porphyrins are reflected in the excited-state reduction potential, E^*_{red}. A sensitizer with an E^*_{red} that is too positive will have low yields of electron injection into TiO_2. Thus, more

efficient cells should incorporate sensitizers that have resonance stabilization and cathodically shifted E_{pa}. However, the picture is more complicated. For example, the excited-state reduction potential of TTP is 220 mV more positive than that of MMP, yet within error both sensitizers generate the same amount of integrated photocurrent. Part of this is certainly related to differences in E_{pa}. The E_{pa} of TTP is 160 mV more positive than that of MMP and the former should exhibit a more rapid rate of electron transfer from the IrO_2 catalyst. It is important to be cautious about shifting the potential of the radical cation too positive as PAP demonstrates. Despite being the most strongly oxidizing of the sensitizers tested, E^*_{red} for PAP is too positive for efficient injection into TiO_2 as the APCE results indicate. The overall effect leads to low photocurrent.

We would expect that the wider coverage of the visible spectrum by free-base porphyrin sensitizers would lead to higher photocurrents relative to $[Ru(bpy)_2(4,4'\text{-}(PO_3H_2)_2bpy)]$. In fact, we see the opposite: Porphyrin-modified electrodes generated roughly half the photocurrent of analogous $[Ru(bpy)_2(4,4'\text{-}(PO_3H_2)_2bpy)]$ cells. As a starting point to understand this difference, we first consider surface coverage. $[Ru(bpy)_2(4,4'\text{-}(PO_3H_2)_2bpy)]$ has a surface coverage on the order of $1 \times 10{-}7$ mol/cm^2 (201). In the current study, the bulky sensitizers TMP and PAP had the lowest surface coverages (0.45×10^{-7} mol/cm^2 and 0.42×10^{-7} mol/cm^2); however, TTP exhibited a higher surface coverage, possibly because the tolyl groups can achieve greater planarity, and the lack of ortho-methyl groups would allow closer approach of the macrocycles. MDC exhibited a high surface coverage relative to MDCE (0.61×10^{-7} mol/cm^2), possibly due to electrostatic effects. An increase in surface coverage is observed in going from TMP to DMP (0.92×10^{-7} mol/cm^2) with a very significant increase in coverage observed with

MMP (2.8×10^{-7} mol/cm^2). Steric effects are probably at work in this case. With every sensitizer the surface coverage is comparable to typical [$Ru(bpy)_2(4,4'\text{-}(PO_3H_2)_2bpy)$] coverages and thus the coverage trends cannot explain the differences in photocurrent.

A second possibility is that the porphyrin sensitizers are not electrochemically stable. As noted above, the oxidation of the sensitizers on TiO_2 is electrochemically irreversible, which could indicate a side reaction of the radical cation or desorption of the oxidized species from the electrode. Several lines of evidence argue for photoelectrochemical stability and authentic water oxidation activity. First, as noted above, irreversibility of porphyrins on TiO_2 has been previously observed (188). Also, we have observed that films of [$Ru(bpy)_2(4,4'\text{-}(PO_3H_2)_2bpy)$] with poor hole transport characteristics also exhibit electrochemical irreversibility on TiO_2 (201). Second, in nonaqueous solutions TMP (195) and TTP (207) are reversible, suggesting that the irreversibility we observe is not due to fundamental chemical instability of the sensitizers. Third, UV-Vis spectra of the electrodes before and after photoelectrolysis generally show no change in absorption, except for MDC (*SI Appendix*, Fig. S4). If the sensitizers are unstable, we would expect to see a change both in peak absorbances and in the shape of the absorption spectrum. Although we do see some increase in absorbance after electrolysis, we suggest that this is related to residual water within the mesoporous TiO_2 and not to sensitizer modification. Finally, we directly observe oxygen generation and determine a Faradaic efficiency close to 100%.

As surface coverages, electrochemical stabilities, and excited-state potentials of these sensitizers are comparable to those of [$Ru(bpy)_2(4,4'\text{-}(PO_3H_2)_2bpy)$], we identify two major differences: injection into TiO_2 and cross-surface hole transport (Fig. 4). Although

we do not directly measure a quantum yield of injection, the APCE for [$Ru(bpy)_2$(4,4′-$(PO_3H_2)_2$bpy)] is 3–10 times larger than APCEs of the porphyrin sensitizers. For some of the porphyrin sensitizers, E^*_{red} is positive of the conduction band edge potential of TiO_2. From that perspective it is surprising that some sensitizers, PAP for example, inject into TiO_2. In this case, it is possible that hot injection may occur from the higher-energy Q(1,0) transitions (208). Under 590-nm long-pass illumination, only a portion of the Q_y(1,0) band is typically illuminated, which could allow for hot injection. Also, fast deactivation pathways may contribute to poor injection. Finally, the anchoring group can have an important effect on electron injection (209, 210). This likely can explain the high photocurrents observed for DMEP and MDCE. In these two molecules, the orbital overlap between the porphyrin macrocycle and the carboxyl group is not impeded by a large dihedral angle between the macrocycle and a meso phenyl ring, as it is in the other compounds.

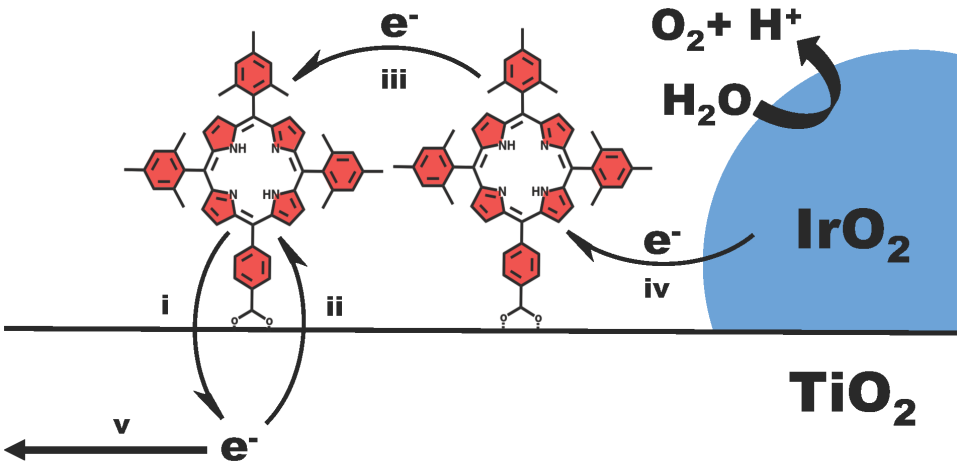

Figure 20 – Selected electron transfer processes in WS-DSPEC
(*i*) injection, (*ii*) recombination, (*iii*) hole transfer, (*iv*) regeneration of oxidized sensitizer, and (*v*) transport to the fluorine-doped tin oxide anode.

The other significant difference we observe compared with [Ru(bpy)$_2$(4,4′-(PO$_3$H$_2$)$_2$bpy)] electrodes is hole transport by the sensitizer layer. For [Ru(bpy)$_2$(4,4′-(PO$_3$H$_2$)$_2$bpy)] at a surface coverage of 10^{-7} mol·cm^{-2}, typical values for D_{app} are in the range of 10^{-9}–10^{-10} cm^2·s^{-1}. Based on the limit of detection of our system, the D_{app} values of the sensitizers we explore in this study are two or more orders of magnitude lower than that of [Ru(bpy)$_2$(4,4′-(PO$_3$H$_2$)$_2$bpy)]. The difference in D_{app} may be related to the difference in charge between [Ru(bpy)$_2$(4,4′-(PO$_3$H$_2$)$_2$bpy)] and the porphyrin sensitizers. Both the Ru(II) and Ru(III) forms of [Ru(bpy)$_2$(4,4′-(PO$_3$H$_2$)$_2$bpy)] are charged and water soluble, whereas only the oxidized form of the porphyrin sensitizers is charged. Oxidation of the neutral porphyrin may induce a significant solvent reorganization energy. Also, the hole on the porphyrin cation is ligand centered, whereas on the Ru(III) complexes it is metal centered, which may play some additional role. Efficient hole transport by the sensitizer is crucial to photocurrent generation, so the low D_{app} values of these sensitizers suggest low or negligible photocurrent. As the distance the hole can travel is a function of both D_{app} and τ_r, the order of magnitude increase in recombination time apparently mitigates the low D_{app} values for the porphyrins. The high surface coverages observed for these sensitizers will also help to mitigate a low D_{app}.

On a final note, the porphyrin-sensitized electrodes are active under red light illumination, whereas [Ru(bpy)$_2$(4,4′-(PO$_3$H$_2$)$_2$bpy)]-sensitized electrodes do not show any photocurrent in the red portion of the spectrum. Most notably the IPCE values for full-spectrum illumination (410 nm long-pass) and for red light illumination (590 nm long-pass) are very similar. Thus, although the actual currents are low, the electrodes use the red photons as well as the rest of the spectrum. The utilization of red light to drive

water splitting represents a significant step forward for molecular photoelectrochemical water-splitting systems.

CONCLUSION

In this study we demonstrate a functioning WS-DSPEC, using organic free-base porphyrin sensitizers. The spectral and electrochemical behavior of the free-base porphyrins can be tuned both by the number and by the type of substituents. Fully substituted porphyrins at the meso position exhibit the most red-shifted spectra and are strongly absorbing. Electron-donating substituents that extend the core π system shift E_{pa} to more cathodic values. Although a negative shift of E_{pa} is desirable for injection into TiO_2, it lowers the driving force for oxidation of IrO_2. Although this study has focused mostly on electron-donating aryl substituents, pentafluorophenyl or cyano substituents are electron withdrawing and would provide an alternative pathway for tuning sensitizer energetics.

Despite the variability in their spectral and electrochemical properties, the majority of the porphyrins exhibited significant photocurrent under illumination. Under full visible and red light illumination, the electrodes produced measurable photocurrents and had open-circuit voltages in excess of 1 V, although the photocurrent was lower than that of electrodes sensitized with $[Ru(bpy)_2(4,4'\text{-}(PO_3H_2)_2bpy)]$. The porphyrin sensitizers have lower injection yields and slower hole transport than $[Ru(bpy)_2(4,4'\text{-}(PO_3H_2)_2bpy)]$. The slow hole transport is partially mitigated by an increase in the recombination time.

ACKNOWLEDGMENTS

We thank Prof. Mark Maroncelli for assistance with emission measurements. Work at Pennsylvania State University was supported by the Office of Basic Energy Sciences, Division of Chemical Sciences, Geosciences, and Energy Biosciences, Department of Energy under Contract DE-FG02-07ER15911, and work at Arizona State University was supported as part of the Center for Bio-Inspired Solar Fuel Production, an Energy Frontier Research Center funded by the US Department of Energy, Office of Science, Office of Basic Energy Sciences under Award DE-SC0001016. N.S.M. and D.D.M.-H. thank the National Science Foundation (NSF) for support as graduate fellows under Grant DGE1255832. Instrumentation and facilities used in this project were supported by the Pennsylvania State University Materials Research Institute Nanofabrication Laboratory under NSF Cooperative Agreement ECS-0335765.

FOOTNOTES

[1]To whom correspondence should be addressed. Email: tem5@psu.edu.

Author contributions: J.R.S., D.D.M.-H., T.A.M., A.L.M., D.G., and T.E.M. designed research; J.R.S., D.D.M.-H., N.S.M., P.L., Y.T., I.P., J.J.T., and N.V.O. performed research; J.R.S., D.D.M.-H., N.S.M., P.L., Y.T., I.P., J.J.T., N.V.O., T.A.M., A.L.M., D.G., and T.E.M. analyzed data; and J.R.S. and D.D.M.-H. wrote the paper.

The authors declare no conflict of interest.

This article is a PNAS Direct Submission.

This article contains supporting information online at

www.pnas.org/lookup/suppl/doi:10.1073/pnas.1414901112/-/DCSupplemental.

KINETIC ISOTOPE EFFECT STUDIES OF BENZIMIDAZOLE-PHENOLS

John J. Tomlin, Anne-Lucie Teillot, Marely Tejeda, Dalvin D. Méndez-Hernández, Dillon Dugan, Christopher Forschino, Alexander Soudakov, Sharon Hammes-Schiffer Thomas A. Moore, Devens Gust, Ana L. Moore

(A manuscript with the subject of this chapter is presently in preparation.)

ABSTRACT

Proton coupled electron transfer (PCET) is an important process in many biological systems. Of specific interest is the tyrosine-histidine couple in photosystem II. Several benzimidazole-phenol (BIP) analogues of this systems have been studied electrochemically, and the standard rate constants and kinetic isotope effects (KIE) have been determined. In addition two of these BIPs include hydrogen bonding moieties as analogues of the asparagine moiety present in natural photosynthesis, in order to introduce a secondary proton acceptor. In one case the KIE was determined utilizing a computational methodology utilizing proton vibrational wave functions.

INTRODUCTION

The electron transfer from the oxygen evolving complex of photosystem II to the oxidized P680 pigment complex is known to be coupled to proton movement between the nearby tyrosine (Tyr_Z) and histidine (His-190), possibly resulting in an increase in the charge separation lifetime. This is an important step in the functioning of photosystem II since an increase in charge separation lifetime can aid in the accumulation of sufficient oxidizing equivalents on the oxygen evolving complex to oxidize water. In the natural system this occurs through the oxidation of the Tyr_Z moiety, followed by proton transfer to the nearby hydrogen bonded His-190 moiety. In addition, there is a asparagine moiety hydrogen bonded to the other side of the histidine ring which could help to provide another site for proton transfer.(217-220)

Benzimidazole-phenols (BIPs) have been studied as synthetic mimics of the tyrosine-histidine pair.(221) It is expected that, for the PCET step to work optimally the proton transfer and electron transfer should occur in a concerted fashion. If this is the case then the proton transfer should occur as part of the rate-limiting step. Therefore the kinetic isotope effect (KIE) of the proton transfer should be larger than 1. The KIE of several BIP models, as shown in figure 21, have been studied by either computational or electrochemical methods, and the effect of the inclusion of a hydrogen bonding substituent at the 4-position of the benzimidazole on the KIE has been studied.

BIP-H

BIP-COOH

BIP-COOMe

BIP-CONEt$_2$

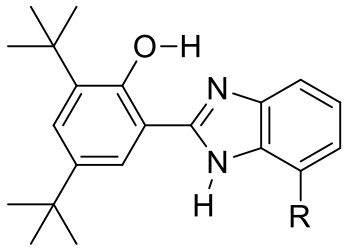

Figure 21 – Studied compounds

EXPERIMENTAL AND THEORETICAL METHODS

Materials:

Methyl 2,3-diaminobenzoate was obtained from Combi-Blocks, and all other chemicals were obtained from Alfa Aesar. Deuterated solvents for NMR were obtained from Cambridge Isotopes.

Synthetic Methods

2-(3',5'-Di-tert-butyl-2'-hydroxyphenyl)-7-carboxybenzimidazole

To a solution of 3,5-di-tert-butyl-2-hydroxybenzaldehyde (1.17165 g, 5 mmol) in nitrobenzene (35 ml) was added drop-wise a suspension of 2,3-diaminobenzoic acid (.76075 mg, 5mmol) in nitrobenzene (35 ml). The mixture was maintained at reflux under argon for 5 hours, after which the nitrobenzene was removed under reduced pressure. The crude material was purified by extraction with 0.1 M potassium hydroxide, followed by neutralization with 1.0 M citric acid to pH 7, and extracting the solution with dichloromethane. The material was purified by column chromatography on silica using 5% methanol in dichloromethane. The material was then crystalized from methanol/hexanes to give (451mg, 1.23 mmol) a 24.6% yield. ^{1}H NMR (400 MHz DMSO-d6): δ_H, ppm 1.32 (s, 9 H) 1.40 (s, 9 H) 7.89 (t, J=8.8 Hz, 1 H) 7.90 (s, 1 H) 7.99 (s, 1 H) 8.02 (d, J=7 Hz, 1 H) 8.29 (s, 1 H) 13.42 (s, 1 H) 13.87 (s, 1 H) 14.39 (s, 1 H); MALDI-TOF: *m/z* calcd for $C_{23}H_{28}N_2O_3$, 366.2, obsd, 367.4

2-(3',5'-Di-tert-butyl-2'-hydroxyphenyl)-7-carbomethoxybenzimidazole

To a solution of 3,5-di-tert-butyl-2-hydroxybenzaldehyde (325 mg, 1.5 mmol) in nitrobenzene (15 ml) was added drop-wise a suspension of methyl 2,3-diaminobenzoate (249 mg, 1.50 mmol) in nitrobenzene (15 ml.) The mixture was maintained at reflux under argon for 16 hours, after witch the nitrobenzene was removed under reduced pressure. The crude material was purified by silica pad using hexanes/dichloromethane, giving a fluorescent yellow solution. The solvent was removed under reduced pressure, and the product was further purified by crystallization from isopropanol/hexanes to give a tan crystalline product (245 mg, 0.644 mmol) a 43 % yield. ^{1}H NMR (400 MHz Benzene-d6): δ_{H}, ppm 1.28 (s, 9 H) 1.72 (s, 9 H) 3.45 (s, 3 H) 6.96 (t, J=7.83 Hz, 1 H) 7.39 (d, J=2.35 Hz, 1 H) 7.64 (d, J=2.35 Hz, 1 H) 7.67 (d, J=7.83 Hz, 1 H) 7.77 (d, J=7.83 Hz, 1 H) 10.55 (br. s., 1 H) 13.79 (s, 1 H) ; MALDI-TOF: *m/z* calcd for $C_{23}H_{28}N_2O_3$, 380.2, obsd, 381.6

Electrochemical Methods

Experimental Conditions

Cyclic Voltammetry

Cyclic Voltammetry was performed with a Potentiostat/Galvanostat Model 273A (EG&G Princeton Applied Research) using a glassy carbon rod (Tokaï 3mm diameter or 1mm diameter) as working electrode, a platinum grid as counter electrode and an Ag/AgCl pseudoreference electrode in a conventional three-electrode cell. Anhydrous acetonitrile (Aldrich) was used as solvent for the electrochemical measurements. The

supporting electrolyte was 0.5M tetrabutylammonium hexafluorophosphate and the solution was deoxygenated by bubbling with argon. The working electrode was cleaned by polishing followed by rinsing with acetone, then dried with hot air. The voltammograms were recorded at 100mV/s. The potential of the pseudoreference electrode was determined using the ferrocenium/ferrocene redox couple as an internal standard (its standard potential being 0.31 V vs SCE (222)).

Controlled Potential Coulometry

Controlled Potential Coulometry was performed with a Potentiostat/Galvanostat Model 273A (EG&G Princeton Applied Research) using a glassy carbon stick (Carbone Lorraine) as working electrode, a platinum grid as counter electrode and an Ag/AgCl pseudoreference electrode in a conventional three-electrode cell. Anhydrous acetonitrile (Aldrich) was used as solvent for the electrochemical measurements. The supporting electrolyte was 0.1M tetrabutylammonium hexafluorophosphate and the solution was deoxygenated by bubbling with argon. The working electrode was cleaned by polishing followed by rinsing with acetone, then dried with hot air. The voltammograms were recorded at 100mV/s. The potential of the pseudoreference electrode was determined using the ferrocenium/ferrocene redox couple as an internal standard.

Cyclic Voltammetry of BiP-COOH in Acetonitrile

BiP-COOH has been investigated by cyclic voltammetry in acetonitrile. As can be seen in Figure 21, the compound exhibits a first reversible wave assigned to the phenol/phenoxyl couple at an apparent standard potential of 0.9V vs SCE. At higher potentials, two irreversible waves are observed possibly characterizing the oxidation of the phenoxyl radical involving an ECE mechanism.

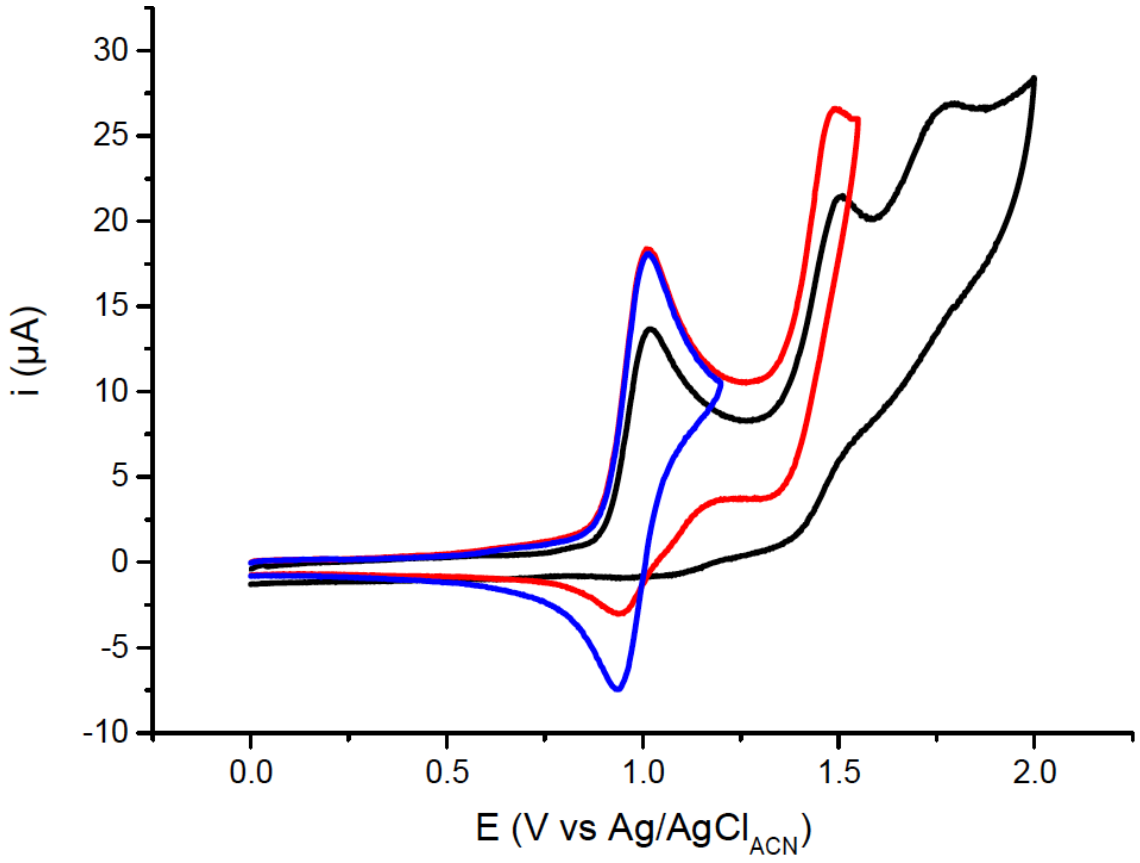

Figure 22 – Cyclic voltammogram of BiP-COOH in Acetonitrile

Cyclic Voltammetry of BiP-COOMe in Acetonitrile

BiP-COOMe has been investigated by cyclic voltammetry in acetonitrile. As can be seen in Figure 22, the compound exhibits a first reversible wave assigned to the phenol/phenoxyl couple at an apparent standard potential of 0.931V vs SCE. At higher potentials, two irreversible waves are observed possibly characterizing the oxidation of the phenoxyl radical involving an ECE mechanism.

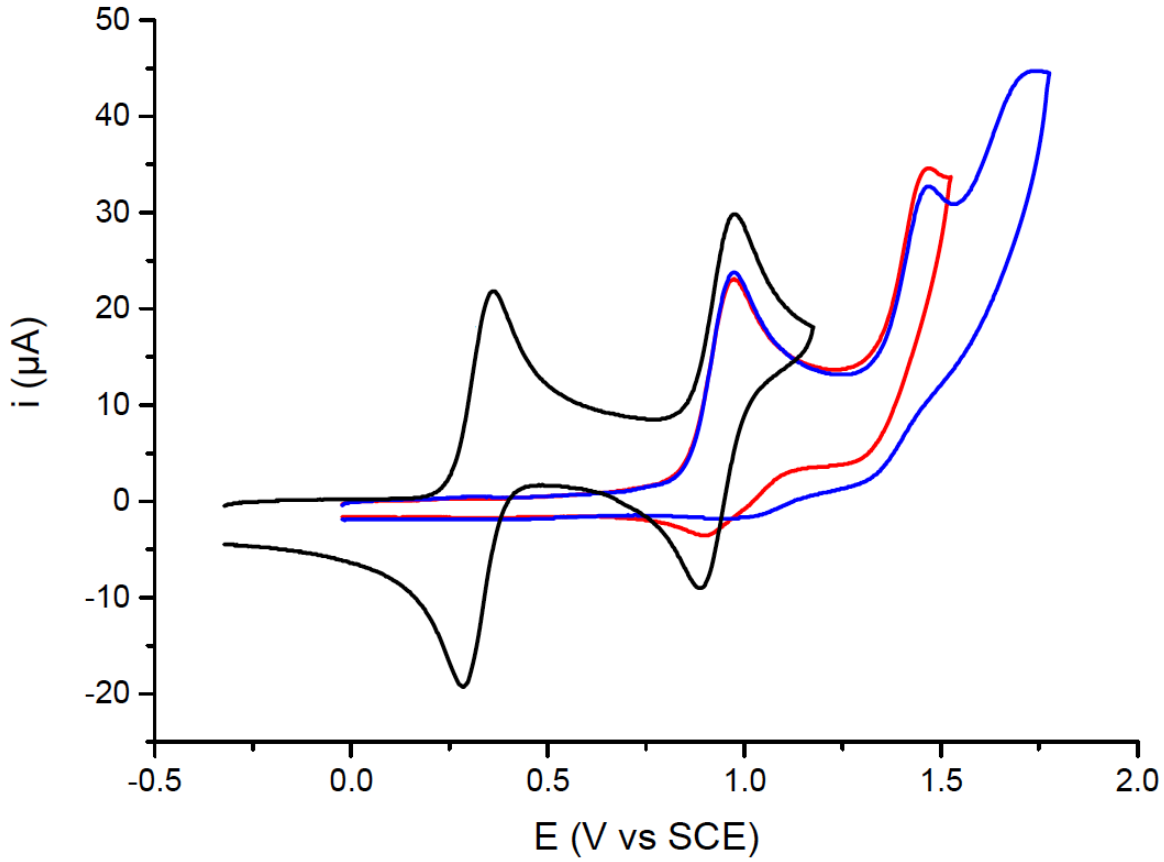

Figure 23 – Cyclic voltammogram of BiP-COOMe in Acetonitrile
The ferrocenium/ferrocene redox couple is re presented by the black line

Determination of Electron Transfer Kinetics using Cyclic Voltammetry

With the assumption that surface phenomenon are not present, electron transfer at an electrode can be represented as the competition of two different rates. that of the electron transfer and that of the diffusion of the species. During the experiment the cyclic voltammogram is recorded at several different rates, and compared to a simulation performed with the DigiSim software package. A trumpet plot is then generated for each system. Equation 2 (which is derived from equation 1) with the assumption the diffusion rate of the compound being measured is substantially similar to that of ferrocene (D = 5 x 10^{-6} cm/s) allows us to determine the apparent standard rate constant.(211)

$$\log(v_{\exp}) = \log(v_{sim}) + \log(\left(\frac{k_s^{exp}}{k_s^{sim}}\right)^2 \frac{D_{sim}}{D_{exp}})$$

(1)

$$\boldsymbol{k_s^{exp} = k_s^{sim} \times 10^{\frac{x - \log 2}{2}}}$$

(2)

Computational Methods

As rates could not be determined by us for the PCET process involved in electron transfer in the BIP-H system studied, it was assumed for the sake of calculation that the electron transfer happened in a concerted fashion with the proton transfer. With this assumption, and following the procedure described in Hammes-Schiffer et al. (211) we can describe the PCET process as a nonadiabatic transition between the electron-proton vibronic states of the ground state and oxidized BIP-solvent complex. The electron-proton vibronic states are represented by the product of the appropriate diabatic electronic state and the associated proton vibronic state.

If the donor-acceptor distance is fixed, the The anodic and cathotic rate constants are as defined in equations 3 and 4 respectively.

$$k_a(\eta;R) = \sum_{\mu,\nu} P_\mu \frac{(V^{el}S_{\mu\nu})^2}{\beta'\hbar}\sqrt{\frac{\pi}{k_BT\lambda}}\rho_M \int d\varepsilon[1-f(\varepsilon)]\, exp\left[\frac{(\Delta\widetilde{U}_{\mu\nu} + \varepsilon - e\eta + \lambda)^2}{4\lambda k_BT}\right]$$

(3)

$$k_c(\eta;R) = \sum_{\mu,\nu} P_\mu \frac{(V^{el}S_{\mu\nu})^2}{\beta'\hbar}\sqrt{\frac{\pi}{k_BT\lambda}}\rho_M \int d\varepsilon f(\varepsilon)\, exp\left[-\frac{(-\Delta\widetilde{U}_{\mu\nu} - \varepsilon + e\eta + \lambda)^2}{4\lambda k_BT}\right]$$

(4)

$$\Delta\widetilde{U}_{\mu\nu} = \Delta U_{\mu\nu} + k_BT\ \ln\frac{Q^{II}}{Q^{I}}$$

(5)

For vibronic states represented by μ for the reduced solute complex and ν for the oxidized solute complex. P_μ and P_ν are the Boltzmann probabilities for the associated vibronic states. $f(\varepsilon)$ is the Fermi distribution function of the electrodes electronic states.

The density of states at the Fermi level is ρ_M, and the electronic coupling is V^{el} and β' is a parameter representing the exponential decay of the electronic coupling for the distance between the molecule and the electrode (~ 1 -3 $\dot{A^{-1}}$). $S_{\mu\nu}$ is the overlap integral, and λ is the reorganization energy. $\Delta U_{\mu\nu}$ is the difference in energy between the vibronic states. Q^I and Q^{II} are the partition functions of the reduced and oxidized solute complexes.

In many systems, it is not appropriate to make the assumption that overlap integral decreases exponentially with R therefore we can include the R mode by thermally averaging over the proton donor acceptor distance.

$$k_a(\eta) = \int P_a(R) k_a(\eta; R) dR$$

(6)

$$k_C(\eta) = \int P_C(R) k_C(\eta; R) dR$$

(7)

Where P_a and P_c are probability distribution functions represented by equation 8.

$$P(R) = \frac{exp\left[-k_{eff}(R-\bar{R})^2/2k_BT\right]}{\int_{-\infty}^{\infty} exp\left[-k_{eff}(R-\bar{R})^2/2k_BT\right] dR}$$

(8)

Where k_{eff} is the effective force constant, and $\bar{R}$ is the equilibrium donor acceptor distance. k_{eff} is calculated from the expansion coefficients c_i which is determined by projecting the normal mode vectors onto the proton-proton axis.

$$k_{eff} = \left[\sum_{i=1}^{3N} \frac{c_i^2}{k_i}\right]^{-1}$$

(9)

The calculations to determine the rate constants were determined utilizing the computational methodology described in Hammes-Schiffer et al.(211) using the reorganization energy of 5.74 kcal/mol found in Mayer et al. (197).

DFT calculations were performed using the unrestricted B3LYP Functional with the 6-31g(d, p) basis set. The calculations were performed with Gaussian 09 on the Saguaro Cluster at Arizona state university, and other calculations were performed using Mathematica 10, with notebooks supplied by Alex Sudakov. Effective force constants were calculated using a script written in python for the purpose.

DISCUSSION

Electrochemical results:

To measure the apparent rate constant, we take advantage of the competition between ET and diffusion. Upon raising the scan rate, the latter becomes faster and faster leading to a situation where ET is rate determining. As shown in Figure 24, the peak potential separation increases from 80mV at 2V/s to more than 140mV at 500V/s for BIP-COOH and to more than 150mv at 500V/s for BIP-COOMe. As may be shown by the oscillations on the CVs in Figure 24 and Figure 25, special attention has been accorded for ohmic drop compensation.

The knowledge of this separation allows the construction of a trumpet plot (Figure 26 and Figure 27) from which the apparent standard rate constant can be easily determined. This study has been performed in two kinds of solution: ACN + 2% MeOH and ACN + 2% MeOD.

The determined apparent electron transfer rate constants in both solutions have been found to be, 0.085 ± 0.007 cm/s and 0.055 ± 0.005 cm/s, respectively, leading to a KIE of 1.5 ± 0.3 for BIP-COOH. The determined apparent electron transfer rate constants in both solutions have been found to be, 0.128 ± 0.005 cm/s and 0.071 ± 0.007 cm/s, respectively, leading to a KIE of 1.8 ± 0.3 for BIP-COOMe.

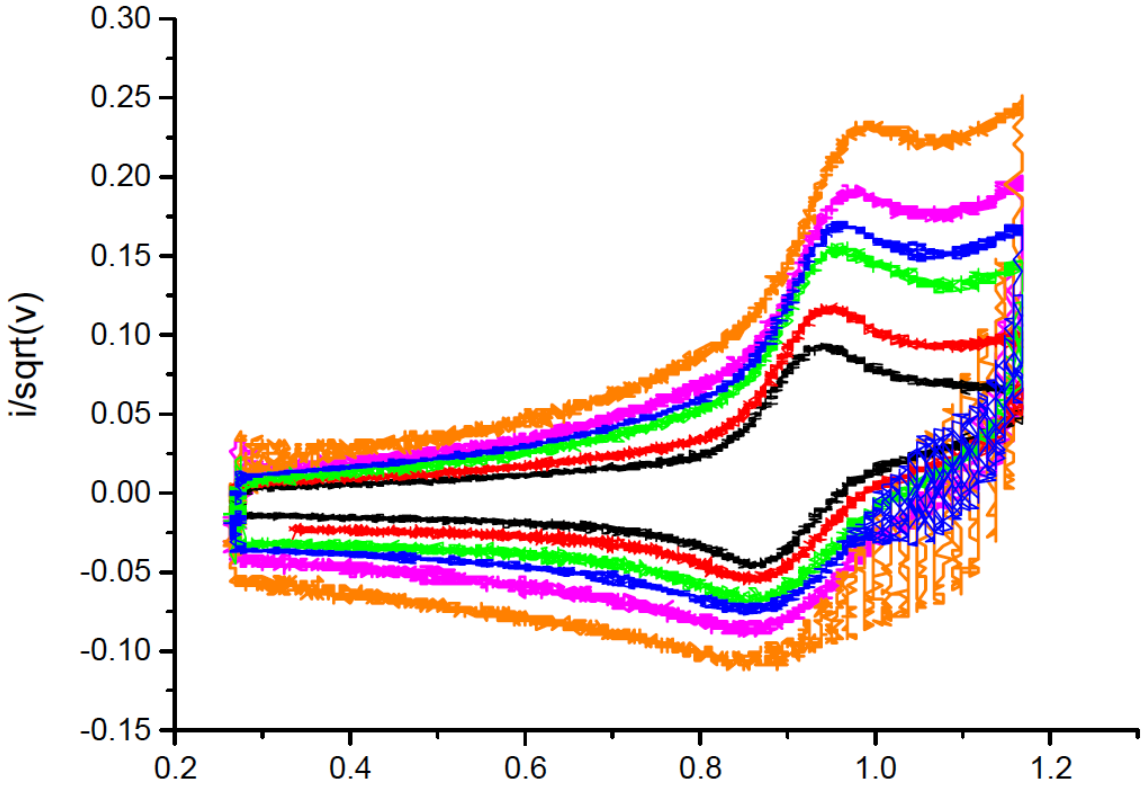

Figure 24 – Normalized cyclic voltammograms of BiP-COOH at a glassy carbon electrode

The Electrode is 1mm diameter, taken in ACN + 2% MeOH 0.5V/s (black), 10 V/s (red), 50V/s (green), 100V/s (blue), 200V/s (pink), 500V/s (orange)

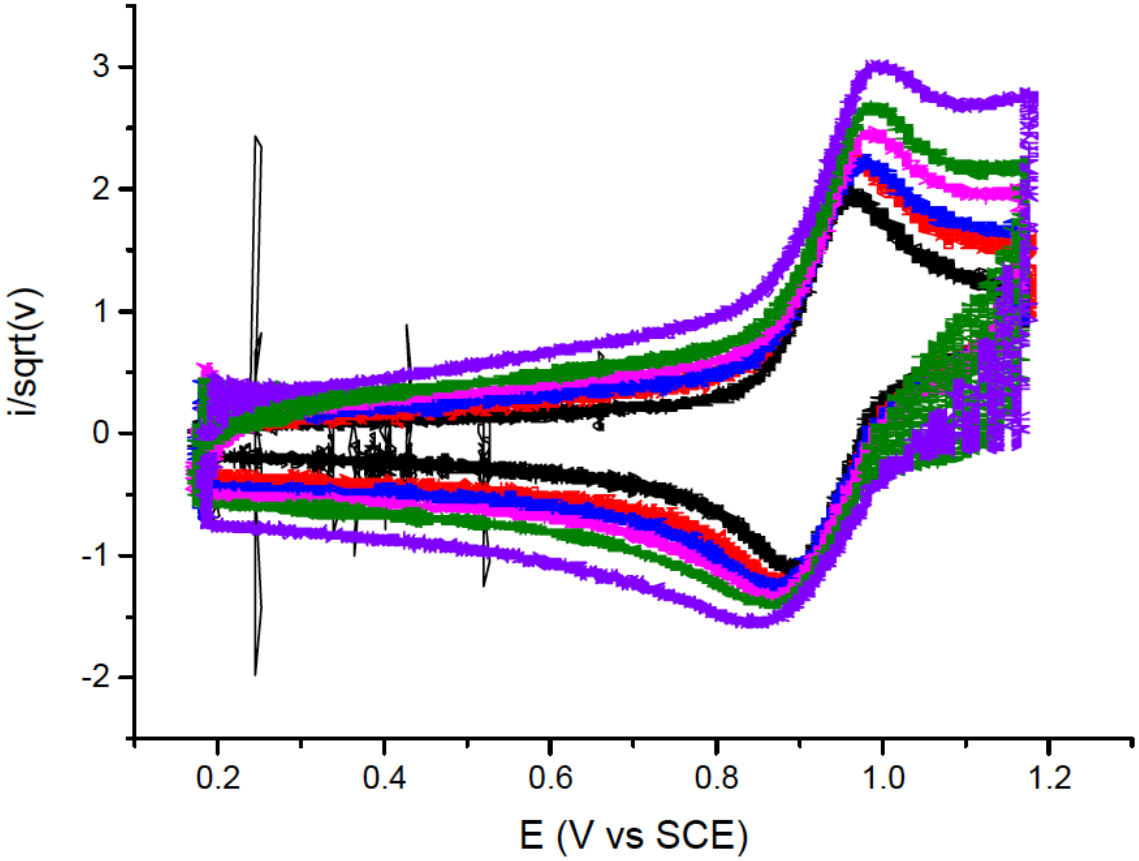

Figure 25 – Normalized cyclic voltammograms of BIP-COOMe
normalized cyclic voltammograms of BIP-COOMe (i is the current and v is the scan rate) of BiP-ester at a glassy carbon electrode (1mm diameter) in ACN + 2% MeOH 2V/s (black), 20 V/s (red), 50V/s (blue), 100V/s (pink), 200V/s (green), 500V/s (purple)

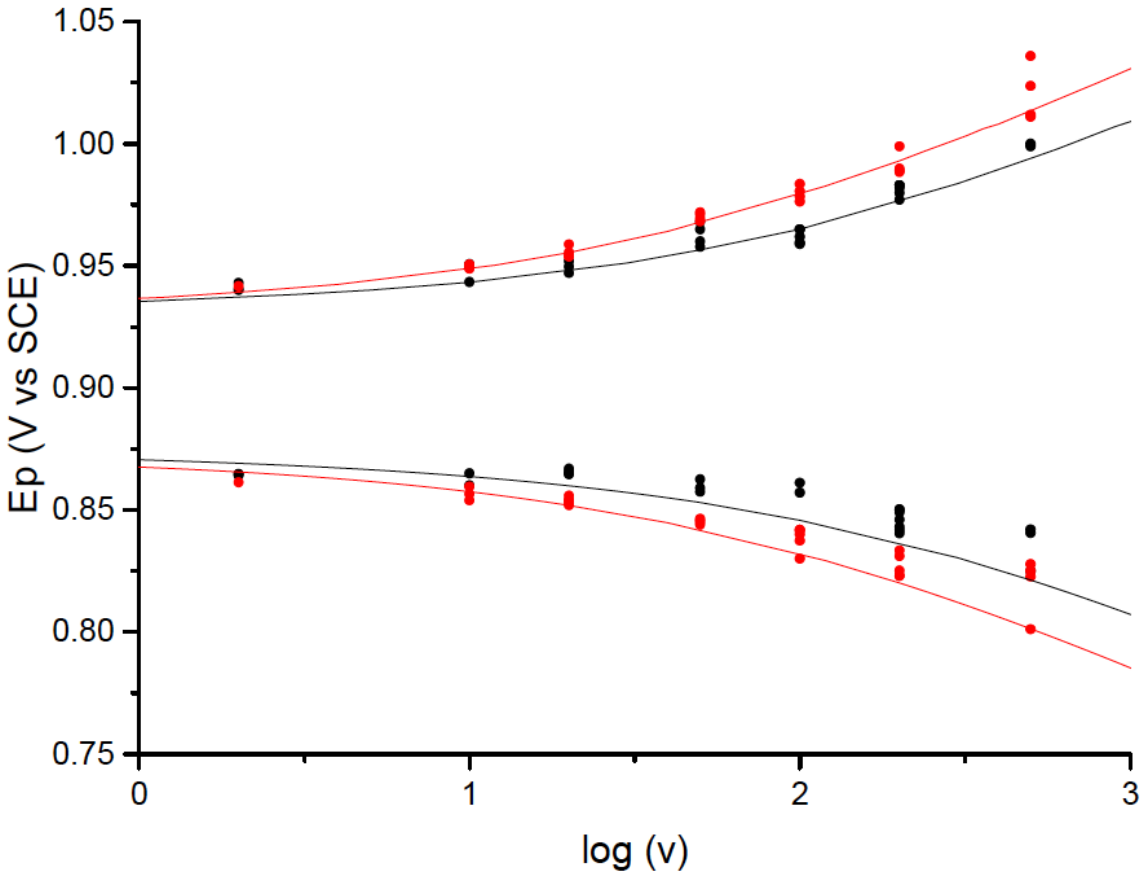

Figure 26 – Trumpet plot for BIP-COOH.
Anodic (upper symbol) and cathodic (lower symbol) peak potentials as a function of the log of scan rate. Simulation of the ‘‘trumpet plot’’ (full line) leads to the determination of the apparent standard rate constant. In ACN + 2% MeOH, experimental peak potential (black circle) and corresponding simulation with k_{app}= 0.089 cm/s (black full line). In ACN + 2% MeOD, experimental peak potential (red circle) and corresponding simulation with k_{app}= 0.050 cm/s (red full line).

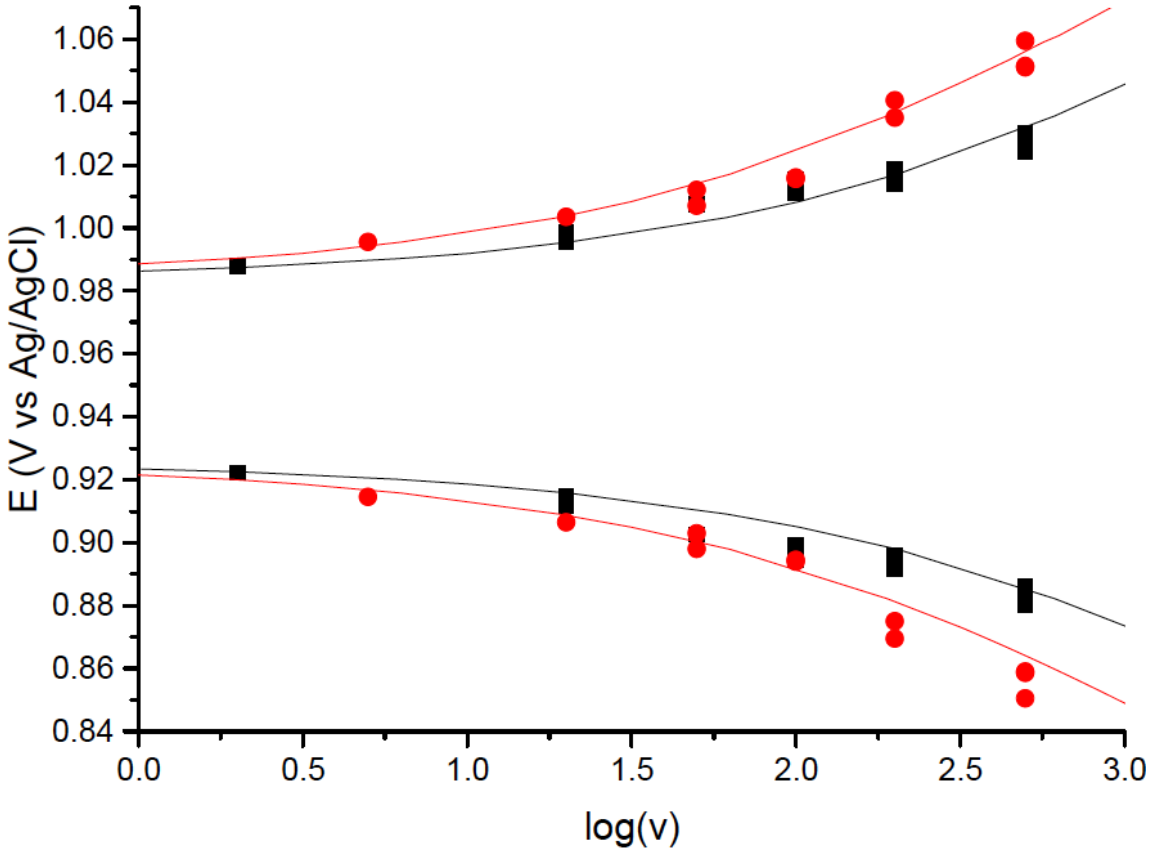

Figure 27 – Trumpet plot for BIP-COOMe.
Anodic (upper symbol) and cathodic (lower symbol) peak potentials as a function of the log of scan rate. Simulation of the ‘‘trumpet plot’’ (full line) leads to the determination of the apparent standard rate constant. In ACN + 2% MeOH, experimental peak potential (black circle) and corresponding simulation with kapp= 0.089 cm/s (black full line). In ACN + 2% MeOD, experimental peak potential (red circle) and corresponding simulation with kapp= 0.050 cm/s (red full line).

Computational results

The energy profiles for the proton movement between the donor and acceptor atoms are shown in Figure 28 for different donor acceptor distances. Calculated Tafel Plots for both the protonated (BIP-H) and deuterated (BIP-D) molecules, Figures 29 and 30 respectively. The rates for both proton transfers were determined to be $k_H = 2.61645 \times 10^7 sec^{-1}$ and $k_D = 2.66442 \times 10^7 sec^{-1}$. The KIE=0.98 determined from Equation 10.

$$KIE = \frac{k_H}{k_D} \tag{10}$$

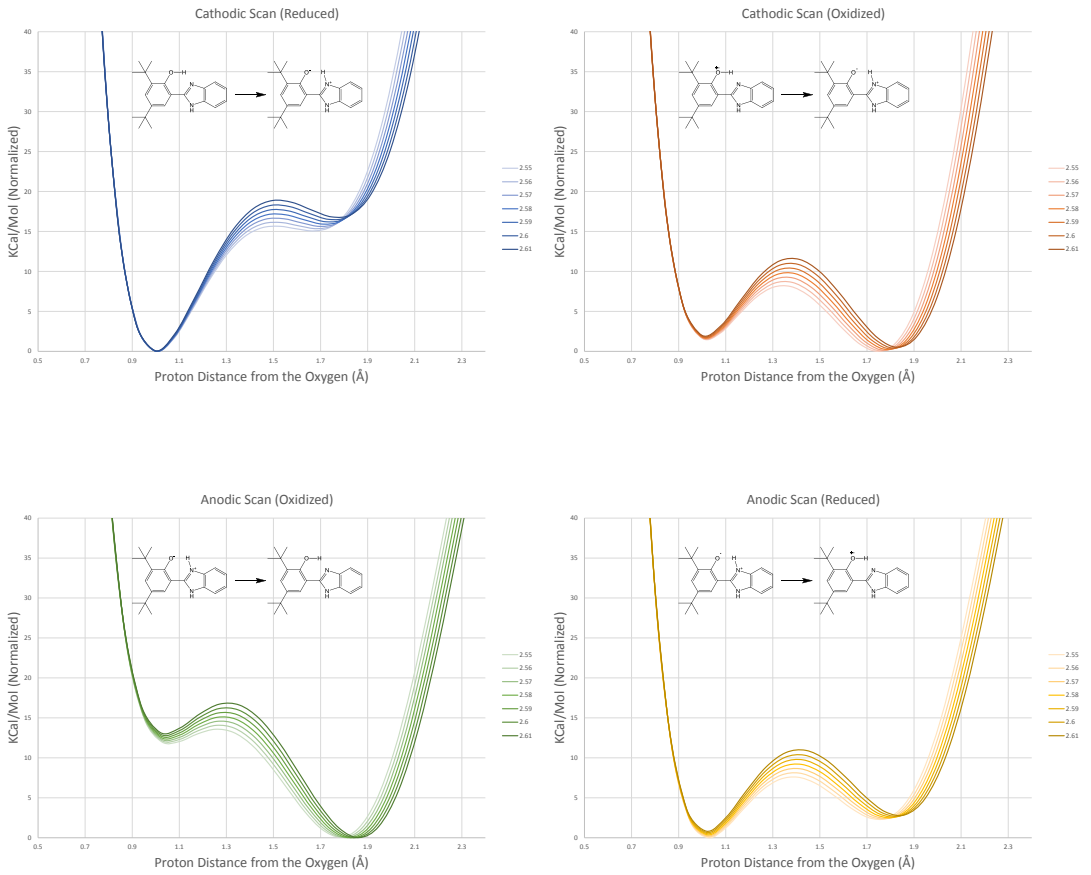

Figure 28 – Proton energy profiles for the cathodic and anodic oxidized and reduced molecules

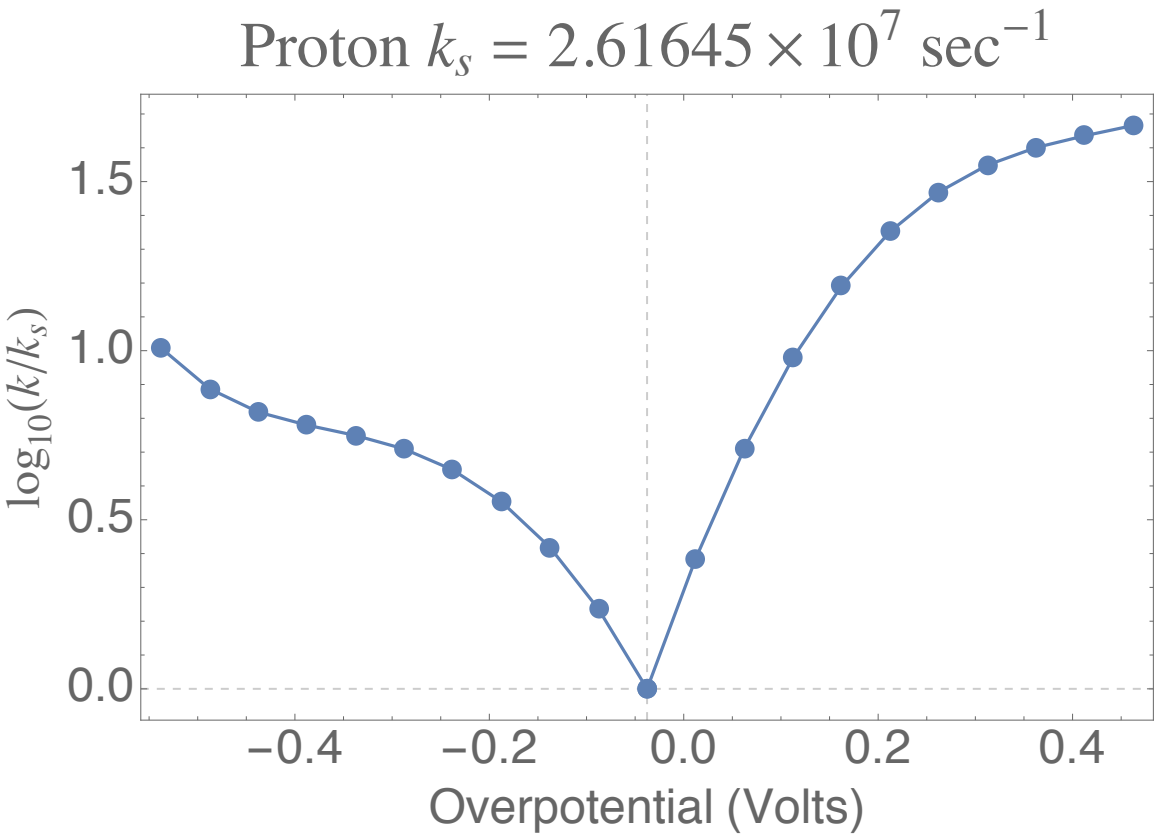

Figure 29 – Tafel plot for BIP-H

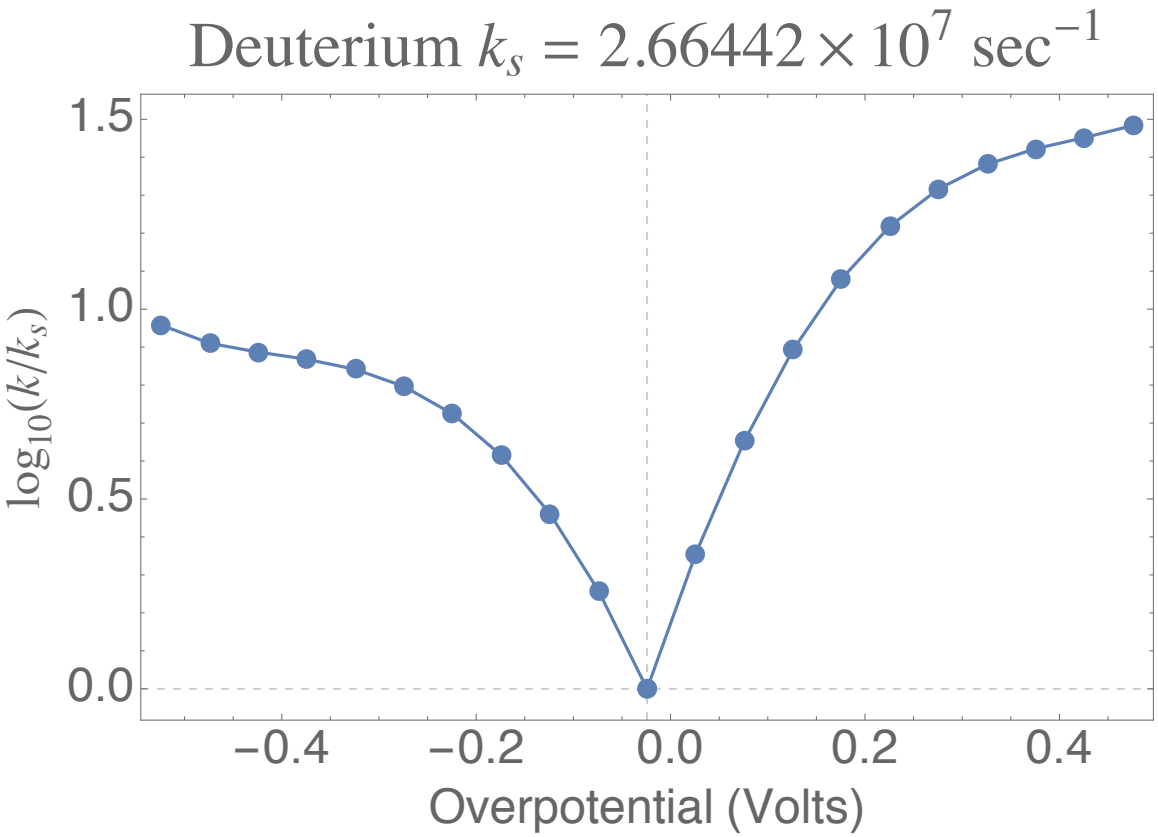

Figure 30 – Tafel Plot for BIP-D

CONCLUSION

In Chapters 2 and 3, titanium dioxide nanoparticles were successfully sensitized by perylene dyes. For both systems with and without reverse micelles surrounding the nanoparticle, perylene dyes **1** and **2** were able to be attached to the titanium dioxide nanoparticles. In both situations, nanoparticles were synthesized with a narrow size distribution. In both cases binding of perylene **3** was inefficient, likely due to steric effects due to the large *t*-butylphenoxyl moieties. Also in both cases photoinduced electron transfer was observed for both perylene **1** and perylene **2**.

In Chapter 4, water splitting dye-sensitized solar cells were successfully demonstrated using metal-free porphyrin sensitizers. Although the porphyrins in question had widely variable electrochemical and spectral characteristics, most of them were able to produce a significant amount of photocurrent when illuminated. Open circuit voltages in excess of 1 V were observed under illumination with both white and red light. The free-base porphyrin sensitizers demonstrated lower injection yields, and slower hole transport than some ruthenium dyes, but these problems were somewhat mitigated by the observed increase in recombination time.

In Chapter 5, a series of benzimidazole-phenol mimics of the tyrosine-histidine complex in photosystem II were synthesized, and the associated kinetic isotope effect was studied utilizing both computational, and electrochemical methods. It was determined that the inclusion of a secondary proton acceptor on the 4-postion of the benzimidazole substantially increased the kinetic isotope effect from approximately 1 for BIP-H up to approximately 1.8 for BIP-COOMe.

References

1. Anderson, N. A.; Lian, T. Q., *Annu. Rev. Phys. Chem.* **2005,** *56*, 491-519.

2. Argazzi, R.; Iha, N. Y. M.; Zabri, H.; Odobel, F.; Bignozzi, C. A., *Coord. Chem. Rev.* **2004,** *248*, 1299-1316.

3. Neouze, M. A.; Schubert, U., *Monatsh. Chem.* **2008,** *139*, 183-195.

4. Stipkala, J. M.; Castellano, F. N.; Heimer, T. A.; Kelly, C. A.; Livi, K. J. T.; Meyer, G. J., *Chem. Mater.* **1997,** *9*, 2341-2353.

5. Zhang, J. Z., *J. Phys. Chem. B* **2000,** *104*, 7239-7253.

6. Zhang, Y. Y.; Galoppini, E., *Chemsuschem* **2010,** *3*, 410-428.

7. Clifford, J. N.; Martinez-Ferrero, E.; Viterisi, A.; Palomares, E., *Chem. Soc. Rev.* **2011,** *40*, 1635-1646.

8. Gratzel, M., *J. Photochem. Photobiol. C-Photochem. Rev.* **2003,** *4*, 145-153.

9. Gratzel, M., *Acc. Chem. Res.* **2009,** *42*, 1788-1798.

10. Hagfeldt, A.; Boschloo, G.; Sun, L. C.; Kloo, L.; Pettersson, H., *Chem. Rev.* **2010,** *110*, 6595-6663.

11. Hagfeldt, A.; Gratzel, M., *Acc. Chem. Res.* **2000,** *33*, 269-277.

12. Listorti, A.; O'Regan, B.; Durrant, J. R., *Chem. Mater.* **2011,** *23*, 3381-3399.

13. Escalada, J. P.; Pajares, A.; Gianotti, J.; Massad, W. A.; Bertolotti, S.; Amat-Guerri, F.; Garcia, N. A., *Chemosphere* **2006,** *65*, 237-244.

14. Henderson, M. A., *Surf. Sci. Rep.* **2011,** *66*, 185-297.

15. Jin, Z. L.; Zhang, X. J.; Lu, G. X.; Li, S. B., *J. Mol. Catal. A-Chem.* **2006,** *259*, 275-280.

16. Kamat, P. V., *Prog. React. Kinet.* **1994,** *19*, 277-316.

17. Kumar, S. G.; Devi, L. G., *J. Phys. Chem. A* **2011,** *115*, 13211-13241.

18. Pei, D. H.; Luan, J. F., *Int. J. Photoen.* **2012**.

19. Beltran-Perez, G.; Lopez-Huerta, F.; Munoz-Aguirre, S.; Castillo-Mixcoatl, J.; Palomino-Merino, R.; Lozada-Morales, R.; Portillo-Moreno, O., *Sens. Actuators, B* **2006,** *120*, 74-78.

20. Stux, A. M.; Meyer, G. J., *J. Fluoresc.* **2002,** *12*, 419-423.

21. Tokudome, H.; Yamada, Y.; Sonezaki, S.; Ishikawa, H.; Bekki, M.; Kanehira, K.; Miyauchi, M., *Appl. Phys. Lett.* **2005,** *87*.

22. Yimit, A.; Itoh, K.; Murabayashi, M., *Sens. Actuators, B* **2003,** *88*, 239-245.

23. Yusoff, N. H.; Salleh, M. M.; Yahaya, M., *Sains Malays.* **2008,** *37*, 249-253.

24. Gundlach, L.; Ernstorfer, R.; Willig, F., *Prog. Surf. Sci.* **2007,** *82*, 355-377.

25. Hilgendorff, M.; Sundström, V., *J. Phys. Chem. B* **1998,** *102*, 10505-10514.

26. Katoh, R.; Furube, A.; Barzykin, A. V.; Arakawa, H.; Tachiya, M., *Coord. Chem. Rev.* **2004,** *248*, 1195-1213.

27. Prezhdo, O. V.; Duncan, W. R.; Prezhdo, V. V., *Acc. Chem. Res.* **2008,** *41*, 339-348.

28. Stergiopoulos, T.; Bernard, M. C.; Goff, A. H. L.; Falaras, P., *Coord. Chem. Rev.* **2004,** *248*, 1407-1420.

29. Bell, T. D. M.; Pagba, C.; Myahkostupov, M.; Hofkens, J.; Piotrowiak, P., *J. Phys. Chem. B* **2006,** *110*, 25314-25321.

30. Durrant, J. R.; Haque, S. A.; Palomares, E., *Coord. Chem. Rev.* **2004,** *248*, 1247-1257.

31. Haque, S. A.; Palomares, E.; Cho, B. M.; Green, A. N. M.; Hirata, N.; Klug, D. R.; Durrant, J. R., *J. Am. Chem. Soc.* **2005,** *127*, 3456-3462.

32. Tachibana, Y.; Nazeeruddin, M. K.; Gratzel, M.; Klug, D. R.; Durrant, J. R., *Chem. Phys.* **2002,** *285*, 127-132.

33. Anandan, S.; Yoon, M., *Spectrochim. Acta, Part A* **2004,** *60*, 885-888.

34. Chen, C.; Qi, X.; Zhou, B., *J. Photochem. Photobiol., A* **1997,** *109*, 155-158.

35. He, J.; Chen, F.; Zhao, J.; Hidaka, H., *Colloids Surf., A* **1998,** *142*, 49-57.

36. He, J.; Zhao, J.; Shen, T.; Hidaka, H.; Serpone, N., *J. Phys. Chem. B* **1997,** *101*, 9027-9034.

37. Huang, H.; Zhou, J.; Zhou, Y.; Zhou, Y.; Feng, Y., *Int. J. Photoen.* **2010,** *2010*, 1-5.

38. Huber, R.; Moser, J. E.; Grätzel, M.; Wachtveitl, J., *Chem. Phys.* **2002,** *285*, 39-45.

39. Joselevich, E.; Willner, I., *J. Phys. Chem.* **1994,** *98*, 7628-7635.

40. Kamat, P. V.; Chauvet, J. P.; Fessenden, R. W., *J. Phys. Chem.* **1986,** *90*, 1389-1394.

41. Kamat, P. V.; Fox, M. A., *Chem. Phys. Lett.* **1983,** *102*, 379-384.

42. Kathiravan, A.; Anbazhagan, V.; Asha Jhonsi, M.; Renganathan, R., *Spectrochim. Acta, Part A* **2008,** *70*, 615-618.

43. Kathiravan, A.; Chandramohan, M.; Renganathan, R.; Sekar, S., *Spectrochim. Acta, Part A* **2009,** *71*, 1783-1787.

44. Kathiravan, A.; Chandramohan, M.; Renganathan, R.; Sekar, S., *Spectrochim. Acta, Part A* **2009,** *72*, 496-501.

45. Kathiravan, A.; Kumar, P. S.; Renganathan, R.; Anandan, S., *Colloids Surf., A* **2009,** *333*, 175-181.

46. Kathiravan, A.; Renganathan, R., *Spectrochim. Acta, Part A* **2008,** *71*, 1106-1109.

47. Kathiravan, A.; Renganathan, R., *Spectrochim. Acta, Part A* **2008,** *71*, 1080-1083.

48. Kathiravan, A.; Renganathan, R., *J. Colloid Interface Sci.* **2009,** *331*, 401-407.

49. Moser, J.; Graetzel, M., *J. Am. Chem. Soc.* **1984,** *106*, 6557-6564.

50. Prashant V, K., *J. Photochem.* **1985,** *28*, 513-524.

51. Qu, P.; Zhao, J.; Zang, L.; Shen, T.; Hidaka, H., *Colloids Surf., A* **1998,** *138*, 39-50.

52. Rath, M. C.; Palit, D. K.; Mukherjee, T.; Ghosh, H. N., *J. Photochem. Photobiol., A* **2009,** *204*, 209-216.

53. Sant, P. A.; Kamat, P. V., *PCCP* **2002,** *4*, 198-203.

54. Walters, K. A.; Gaal, D. A.; Hupp, J. T., *J. Phys. Chem. B* **2002,** *106*, 5139-5142.

55. Wang, C.-y.; Liu, C.-y.; Wang, W.-q.; Shen, T., *J. Photochem. Photobiol., A* **1997,** *109*, 159-164.

56. Wang, C.-y.; Liu, C.-y.; Wang, Y.; Shen, T., *J. Colloid Interface Sci.* **1998,** *197*, 126-132.

57. Wu, T.; Xu, S.-J.; Shen, J.-Q.; Chen, S.; Zhang, M.-H.; Shen, T., *J. Photochem. Photobiol., A* **2000,** *137*, 191-196.

58. Zang, L.; Liu, C.-Y.; Ren, X.-M., *J. Photochem. Photobiol., A* **1995,** *88*, 47-51.

59. Zang, L.; Qu, P.; Zhao, J.; Shen, T.; Hidaka, H., *Chem. Lett.* **1997,** *26*, 791-792.

60. Zhang, H.; Zhou, Y.; Zhang, M.; Shen, T.; Xiang, J.; Feng, J., *J. Colloid Interface Sci.* **2003,** *263*, 669-673.

61. Zhou, Z.-X.; Qian, S.-P.; Yao, S.-D.; Zhang, Z.-Y., *Dyes and Pigments* **2001,** *51*, 137-144.

62. Zhou, Z.; Qian, S.; Yao, S.; Zhang, Z., *Radiat. Phys. Chem.* **2002,** *65*, 241-248.

63. Zuo, P.; Li, C.; Wu, Y.-S.; Ai, X.-C.; Wang, X.-S.; Zhang, B.-W.; Zhang, J.-P., *J. Photochem. Photobiol., A* **2006,** *183*, 138-145.

64. Avlasevich, Y.; Li, C.; Mullen, K., *J. Mater. Chem.* **2010,** *20*.

65. Cappel, U. B.; Karlsson, M. H.; Pschirer, N. G.; Eickemeyer, F.; Schöneboom, J.; Erk, P.; Boschloo, G.; Hagfeldt, A., *J. Phys. Chem. C* **2009,** *113*, 14595-14597.

66. Edvinsson, T.; Li, C.; Pschirer, N.; Schöneboom, J.; Eickemeyer, F.; Sens, R.; Boschloo, G.; Herrmann, A.; Müllen, K.; Hagfeldt, A., *J. Phys. Chem. C* **2007,** *111*, 15137-15140.

67. Ferrere, S.; Gregg, B. A., *New J. Chem.* **2002,** *26*.

68. Ferrere, S.; Zaban, A.; Gregg, B. A., *J. Phys. Chem. B* **1997,** *101*, 4490-4493.

69. Fortage, J.; Séverac, M.; Houarner-Rassin, C.; Pellegrin, Y.; Blart, E.; Odobel, F., *J. Photochem. Photobiol., A* **2008,** *197*, 156-169.

70. Li, C.; Liu, Z.; Schoneboom, J.; Eickemeyer, F.; Pschirer, N. G.; Erk, P.; Herrmann, A.; Mullen, K., *J. Mater. Chem.* **2009,** *19*.

71. Li, C.; Yum, J.-H.; Moon, S.-J.; Herrmann, A.; Eickemeyer, F.; Pschirer, N. G.; Erk, P.; Schöneboom, J.; Müllen, K.; Grätzel, M*., et al.*, *Chemsuschem* **2008,** *1*, 573-573.

72. Mathew, S.; Imahori, H., *J. Mater. Chem.* **2011,** *21*.

73. Planells, M.; Cespedes-Guirao, F. J.; Forneli, A.; Sastre-Santos, A.; Fernandez-Lazaro, F.; Palomares, E., *J. Mater. Chem.* **2008,** *18*.

74. Shibano, Y.; Umeyama, T.; Matano, Y.; Imahori, H., *Org. Lett.* **2007,** *9*, 1971-1974.

75. Szarko, J. M.; Neubauer, A.; Bartelt, A.; Socaciu-Siebert, L.; Birkner, F.; Schwarzburg, K.; Hannappel, T.; Eichberger, R., *J. Phys. Chem. C* **2008,** *112*, 10542-10552.

76. Nilsing, M.; Persson, P.; Lunell, S.; Ojamae, L., *J. Phys. Chem. C* **2007,** *111*, 12116-12123.

77. Liu, H. B.; Xu, J. L.; Li, Y. J.; Li, Y. L., *Acc. Chem. Res.* **2010,** *43*, 1496-1508.

78. Liu, H. B.; Zuo, Z. C.; Guo, Y. B.; Li, Y. J.; Li, Y. L., *Angew. Chem. Int. Ed.* **2010,** *49*, 2705-2707.

79. Zheng, H. Y.; Li, Y. J.; Liu, H. B. A.; Yin, X. D.; Li, Y. L., *Chem. Soc. Rev.* **2011,** *40*, 4506-4524.

80. Dubey, R. K.; Efimov, A.; Lemmetyinen, H., *Chem. Mater.* **2011,** *23*, 778-788.

81. Kohl, C.; Weil, T.; Qu, J. Q.; Mullen, K., *Chem. Eur. J.* **2004,** *10*, 5297-5310.

82. Crans, D. C.; Levinger, N. E., *Acc. Chem. Res.* **2012**.

83. Lakowicz, J. R., *Principles of Fluorescence Spectroscopy*. Third ed.; Springer: 2006; p 961.

84. www.public.asu.edu/~laserweb/asufit/asufit.html.

85. Rasband, W. S. *ImageJ*, U. S. National Institutes of Health: Bethesda, Maryland, USA. http://imagej.nih.gov/ij/, 1997-2012.

86. Frisch, M. J.; Trucks, G. W.; Schlegel, H. B.; Scuseria, G. E.; Robb, M. A.; Cheeseman, J. R.; Scalmani, G.; Barone, V.; Mennucci, B.; Petersson, G. A.*, et al. Gaussian 09*, Revision A.02; Wallingford, CT, 2009.

87. Fukuda, T.; Homma, S.; Kobayashi, N., *Chem. Eur. J.* **2005,** *11*, 5205-5216.

88. Mack, J.; Asano, Y.; Kobayashi, N.; Stillman, M. J., *J. Am. Chem. Soc.* **2005,** *127*, 17697-17711.

89. Mack, J.; Bunya, M.; Lansky, D.; Goldberg, D. P.; Kobayashi, N., *Heterocycles* **2008,** *76*, 1369-1380.

90. Clark, A. E.; Qin, C. Y.; Li, A. D. Q., *J. Am. Chem. Soc.* **2007,** *129*, 7586-7595.

91. Francl, M. M.; Pietro, W. J.; Hehre, W. J.; Binkley, J. S.; Gordon, M. S.; Defrees, D. J.; Pople, J. A., *J. Chem. Phys.* **1982,** *77*, 3654-3665.

92. Harihan, P. C.; Pople, J. A., *Theor. Chim. Acta* **1973,** *28*, 213-222.

93. Rassolov, V. A.; Pople, J. A.; Ratner, M. A.; Windus, T. L., *J. Chem. Phys.* **1998,** *109*, 1223-1229.

94. Shibano, Y.; Imahori, H.; Adachi, C., *J. Phys. Chem. C* **2009,** *113*, 15454-15466.

95. Barone, V.; Cossi, M., *J. Phys. Chem. A* **1998,** *102*, 1995-2001.

96. Cossi, M.; Rega, N.; Scalmani, G.; Barone, V., *J. Comput. Chem.* **2003,** *24*, 669-681.

97. Weng, Y.-X.; Li, L.; Liu, Y.; Wang, L.; Yang, G.-Z., *J. Phys. Chem. B* **2003,** *107*, 4356-4363.

98. Sakata, T.; Hashimoto, K.; Hiramoto, M., *J. Phys. Chem.* **1990,** *94*, 3040-3045.

99. Redmond, G.; Fitzmaurice, D., *J. Phys. Chem.* **1993,** *97*, 1426-1430.

100. Wang, Y.; Herron, N., *J. Phys. Chem.* **1991,** *95*, 525-532.

101. Bawendi, M. G.; Steigerwald, M. L.; Brus, L. E., *Annu. Rev. Phys. Chem.* **1990,** *41*, 477-496.

102. Monticone, S.; Tufeu, R.; Kanaev, A. V.; Scolan, E.; Sanchez, C., *Appl. Surf. Sci.* **2000,** *162–163*, 565-570.

103. Kaniyankandy, S.; Ghosh, H. N., *J. Mater. Chem.* **2009,** *19*, 3523-3528.

104. Vayssieres, L.; Persson, C.; Guo, J. H., *Appl. Phys. Lett.* **2011,** *99*.

105. Hegazy, A.; Prouzet, E., *Chem. Mater.* **2012,** *24*, 245-254.

106. Yacaman, M. J.; Ascencio, J. A.; Liu, H. B.; Gardea-Torresdey, J., *J. Vac. Sci. Thechnol., B* **2001,** *19*, 1091-1103.

107. Falaras, P., *Sol. Energy Mater. Sol. Cells* **1998,** *53*, 163-175.

108. Finnie, K. S.; Bartlett, J. R.; Woolfrey, J. L., *Langmuir* **1998,** *14*, 2744-2749.

109. Neubauer, A.; Szarko, J. M.; Bartelt, A. F.; Eichberger, R.; Hannappel, T., *J. Phys. Chem. C* **2011,** *115*, 5683-5691.

110. Pankove, J. I., *Optical Processes in Semiconductors*. Courier Dover Publications: 2010.

111. Atik, S. S.; Thomas, J. K., *J. Am. Chem. Soc.* **1981,** *103*, 3543-3550.

112. Stockwell, D.; Yang, Y.; Huang, J.; Anfuso, C.; Huang, Z. Q.; Lian, T. Q., *J. Phys. Chem. C* **2010,** *114*, 6560-6566.

113. Gao, Y. Q.; Georgievskii, Y.; Marcus, R. A., *J. Chem. Phys.* **2000,** *112*, 3358-3369.

114. Ai, X.; Anderson, N. A.; Guo, J. C.; Lian, T. Q., *J. Phys. Chem. B* **2005,** *109*, 7088-7094.

115. Ai, X.; Guo, J. C.; Anderson, N. A.; Lian, T. Q., *J. Phys. Chem. B* **2004,** *108*, 12795-12803.

116. Lundqvist, M. J.; Nilsing, M.; Lunell, S.; Akermark, B.; Persson, P., *J. Phys. Chem. B* **2006,** *110*, 20513-20525.

117. Gratzel, M., *Dye-sensitized solar cells.* Journal of Photochemistry and Photobiology C-Photochemistry Reviews, 2003. **4**(2): p. 145-153.

118. Gratzel, M., *Recent Advances in Sensitized Mesoscopic Solar Cells.* Accounts of Chemical Research, 2009. **42**(11): p. 1788-1798.

119. Hagfeldt, A., et al., *Dye-Sensitized Solar Cells.* Chemical Reviews, 2010. **110**(11): p. 6595-6663.

120. Hagfeldt, A. and M. Gratzel, *Molecular photovoltaics.* Accounts of Chemical Research, 2000. **33**(5): p. 269-277.

121. Anikeeva, P.O., et al., *Electronic and excitonic processes in light-emitting devices based on organic materials and colloidal quantum dots.* Physical Review B, 2008. **78**(8).

122. Zhu, X.Y., *Electronic structure and electron dynamics at molecule-metal interfaces: implications for molecule-based electronics.* Surface Science Reports, 2004. **56**(1-2): p. 1-83.

123. Lindstrom, C.D. and X.Y. Zhu, *Photoinduced electron transfer at molecule-metal interfaces.* Chemical Reviews (Washington, DC, United States), 2006. **106**(10): p. 4281-4300.

124. Zhu, X.Y., *Charge transport at metal-molecule interfaces: A spectroscopic view.* Journal of Physical Chemistry B, 2004. **108**(26): p. 8778-8793.

125. Coropceanu, V., et al., *Charge transport in organic semiconductors.* Chemical Reviews, 2007. **107**(4): p. 926-952.

126. Tulevski, G.S., et al., *Formation of catalytic metal-molecule contacts.* Science (Washington, DC, United States), 2005. **309**(5734): p. 591-594.

127. Kamat, P.V., *Interfacial charge transfer processes in colloidal semiconductor systems.* Progress in Reaction Kinetics, 1994. **19**(3): p. 277-316.

128. Anderson, N.A. and T.Q. Lian, *Ultrafast electron transfer at the molecule-semiconductor nanoparticle interface.* Annual Review of Physical Chemistry, 2005. **56**: p. 491-519.

129. Stipkala, J.M., et al., *Light-Induced Charge Separation at Sensitized Sol−Gel Processed Semiconductors.* Chem. Mater., 1997. **9**(11): p. 2341-2353.

130. Zhang, J.Z., *Interfacial Charge Carrier Dynamics of Colloidal Semiconductor Nanoparticles.* J. Phys. Chem. B, 2000. **104**(31): p. 7239-7253.

131. Zhang, Y.Y. and E. Galoppini, *Organic Polyaromatic Hydrocarbons as Sensitizing Model Dyes for Semiconductor Nanoparticles.* Chemsuschem, 2010. **3**(4): p. 410-428.

132. Hilgendorff, M. and V. Sundström, *Dynamics of Electron Injection and Recombination of Dye-Sensitized TiO2 Particles.* J. Phys. Chem. B, 1998. **102**(51): p. 10505-10514.

133. He, J., et al., *Photosensitization of Colloidal Titania Particles by Electron Injection from an Excited Organic Dye−Antennae Function.* J. Phys. Chem. B, 1997. **101**(44): p. 9027-9034.

134. Joselevich, E. and I. Willner, *Photosensitization of Quantum-Size TiO2 Particles in Water-in-Oil Microemulsions.* The Journal of Physical Chemistry, 1994. **98**(31): p. 7628-7635.

135. Moser, J. and M. Graetzel, *Photosensitized electron injection in colloidal semiconductors.* J. Am. Chem. Soc., 1984. **106**(22): p. 6557-6564.

136. Sant, P.A. and P.V. Kamat, *Interparticle electron transfer between size-quantized CdS and TiO2 semiconductor nanoclusters.* Physical Chemistry Chemical Physics, 2002. **4**(2): p. 198-203.

137. Zhang, H., et al., *Nanosecond time-resolved studies of long-lived photoinduced charge separation in the dyad fluorescein–anthraquinone–methyl ester adsorbed on TiO2 colloids.* Journal of Colloid and Interface Science, 2003. **263**(2): p. 669-673.

138. Hernández, L.I., et al., *Spectral Characteristics and Photosensitization of TiO2 Nanoparticles in Reverse Micelles by Perylenes.* The Journal of Physical Chemistry B, 2012: p. doi: 10.1021/jp3086792.

139. Avlasevich, Y., C. Li, and K. Mullen, *Synthesis and applications of core-enlarged perylene dyes.* Journal of Materials Chemistry, 2010. **20**(19): p. 3814-3826.

140. Cappel, U.B., et al., *A Broadly Absorbing Perylene Dye for Solid-State Dye-Sensitized Solar Cells.* The Journal of Physical Chemistry C, 2009. **113**(33): p. 14595-14597.

141. Edvinsson, T., et al., *Intramolecular Charge-Transfer Tuning of Perylenes: Spectroscopic Features and Performance in Dye-Sensitized Solar Cells.* The Journal of Physical Chemistry C, 2007. **111**(42): p. 15137-15140.

142. Fortage, J., et al., *Synthesis of new perylene imide dyes and their photovoltaic performances in nanocrystalline TiO2 dye-sensitized solar cells.* Journal of Photochemistry and Photobiology A: Chemistry, 2008. **197**(2–3): p. 156-169.

143. Li, C., et al., *An Improved Perylene Sensitizer for Solar Cell Applications.* Chemsuschem, 2008. **1**(7): p. 573-573.

144. Mathew, S. and H. Imahori, *Tunable, strongly-donating perylene photosensitizers for dye-sensitized solar cells.* Journal of Materials Chemistry, 2011. **21**(20): p. 7166-7174.

145. Planells, M., et al., *Interfacial photo-induced charge transfer reactions in perylene imide dye sensitised solar cells.* Journal of Materials Chemistry, 2008. **18**(47): p. 5802-5808.

146. Shibano, Y., et al., *Electron-donating perylene tetracarboxylic acids for dye-sensitized solar cells.* Organic Letters, 2007. **9**(10): p. 1971-1974.

147. Shibano, Y., H. Imahori, and C. Adachi, *Organic Thin-Film Solar Cells Using Electron-Donating Perylene Tetracarboxylic Acid Derivatives.* Journal of Physical Chemistry C, 2009. **113**(34): p. 15454-15466.

148. Kohl, C., et al., *Towards highly fluorescent and water-soluble perylene dyes.* Chemistry-a European Journal, 2004. **10**(21): p. 5297-5310.

149. Mutin, P.H. and A. Vioux, *Nonhydrolytic Processing of Oxide-Based Materials: Simple Routes to Control Homogeneity, Morphology, and Nanostructure.* Chemistry of Materials, 2009. **21**(4): p. 582-596.

150. Arnal, P., et al., *A Solution Chemistry Study of Nonhydrolytic Sol−Gel Routes to Titania.* Chemistry of Materials, 1997. **9**(3): p. 694-698.

151. Vioux, A., *Nonhydrolytic Sol−Gel Routes to Oxides.* Chemistry of Materials, 1997. **9**(11): p. 2292-2299.

152. Time-resolved absorption and emission global-analysis software. Available at: www.public.asu.edu/~laserweb/asufit/asufit.html. Accessed on 1 Jun 2013

153. Nilsing, M., et al., *Dye-sensitization of the TiO2 rutile (110) surface by perylene dyes: Quantum-chemical periodic B3LYP computations.* Journal of Physical Chemistry C, 2007. **111**(32): p. 12116-12123.

154. Weng, Y.-X., et al., *Surface-Binding Forms of Carboxylic Groups on Nanoparticulate TiO2 Surface Studied by the Interface-Sensitive Transient Triplet-State Molecular Probe.* The Journal of Physical Chemistry B, 2003. **107**(18): p. 4356-4363.

155. Redmond, G. and D. Fitzmaurice (1993) Spectroscopic determination of flatband potentials for polycrystalline titania electrodes in nonaqu- eous solvents. J. Phys. Chem. 97, 1426–1430.

156. Ferrere, S. and B.A. Gregg, *New perylenes for dye sensitization of TiO2.* New Journal of Chemistry, 2002. **26**(9).

157. Li, C., et al., *Perylenes as sensitizers in hybrid solar cells: how molecular size influences performance.* Journal of Materials Chemistry, 2009. **19**(30): p. 5405-5415.

158. *Multivariate Curve Resolution software MCR-ALS GUI*. Available from: http://www.ub.edu/mcr/web_mcr/download.html.

159. Wurthner, F. (2006) Bay-substituted perylene bisimides: Twisted fluorophores for supramolecular chemistry. Pure Appl. Chem. 78, 2341–2349.

160. Wurthner, F. (2004) Perylene bisimide dyes as versatile building blocks for functional supramolecular architectures. Chem. Commun. 1564–1579.

161. Birks, J. B. (1970) Photophysics of Aromatic Molecules. John Wiley & Sons Ltd, London. Langhals, H., S. Demmig and T. Potrawa (1991) The relation

between packing effects and solid state fluorescence of dyes. Journal f€ur Praktische Chemie 333, 733–748.

162. Langhals, H., S. Demmig and T. Potrawa (1991) The relation between packing effects and solid state fluorescence of dyes. Journal f€ur Praktische Chemie 333, 733–748.

163. Sakata, T., K. Hashimoto and M. Hiramoto (1990) New aspects of electron-transfer on semiconductor surface – dye-sensitization sys- tem. J. Phys. Chem. 94, 3040–3045.

164. Stockwell, D., Y. Yang, J. Huang, C. Anfuso, Z. Q. Huang and T. Q. Lian (2010) Comparison of electron-transfer dynamics from coumarin 343 to TiO_2, SnO_2, and ZnO nanocrystalline thin films: Role of inter- face-bound charge-separated pairs. J. Phys. Chem. C 114, 6560–6566.

165. Gao, Y. Q., Y. Georgievskii and R. A. Marcus (2000) On the theory of electron transfer reactions at semiconductor electrode/liquid inter- faces. J. Chem. Phys. 112, 3358–3369.

166. Ai, X., N. A. Anderson, J. C. Guo and T. Q. Lian (2005) Electron injection dynamics of Ru polypyridyl complexes on SnO_2 nanocrys- talline thin films. J. Phys. Chem. B 109, 7088–7094.

167. Ai, X., J. C. Guo, N. A. Anderson and T. Q. Lian (2004) Ultrafast electron transfer from Ru polypyridyl complexes to Nb_2O_5 nanopor- ous thin films. J. Phys. Chem. B 108, 12795–12803.

168. Kuciauskas, D., M. S. Freund, H. B. Gray, J. R. Winkler and N. S. Lewis (2001) Electron transfer dynamics in nanocrystalline titanium dioxide solar cells sensitized with ruthenium or osmium polypyridyl complexes. J. Phys. Chem. B 105, 392–403.

169. Swierk JR, Mallouk TE (2013) Design and development of photoanodes for water-splitting dye-sensitized photoelectrochemical cells. *Chem Soc Rev* 42:2357–2387.

170. McDaniel ND, Bernhard S (2010) Solar fuels: thermodynamics, candidates, tactics, and figures of merit. *Dalton Trans* 39:10021–10030.

171. McConnell I, Li G, Brudvig GW (2010) Energy Conversion in Natural and Artificial Photosynthesis. *Chemistry & biology* 17:434–447.

172. Sundholm D (1999) Density functional theory calculations of the visible spectrum of chlorophyll a. *Chemical Physics Letters* 302:480–484.

173. Gouterman M (1978) in *The Porphyrins*, ed Dolphin D (Academic Press, New York), pp 1–165.

174. Li L-L, Diau EW-G (2013) Porphyrin-sensitized solar cells. *Chem Soc Rev* 42:291–304.

175. Imahori H, Umeyama T, Ito S (2009) Large pi-aromatic molecules as potential sensitizers for highly efficient dye-sensitized solar cells. *Acc Chem Res* 42:1809–1818.

176. Giribabu L, Kanaparthi RK (2013) Are porphyrins an alternative to ruthenium(II) sensitizers for dye-sensitized solar cells? *Current Science* 104:847–855.

177. Yella A et al. (2011) Porphyrin-sensitized solar cells with cobalt (II/III)-based redox electrolyte exceed 12 percent efficiency. *Science* 334:629–634.

178. Gao Y et al. (2013) Visible light driven water splitting in a molecular device with unprecedentedly high photocurrent density. *J Am Chem Soc* 135:4219–4222.

179. McAlpin JG, Stich TA, Casey WH, Britt RD (2012) Comparison of cobalt and manganese in the chemistry of water oxidation. *Coordination Chemistry Reviews* 256:2445–2452.

180. Du P, Eisenberg R (2012) Catalysts made of earth-abundant elements (Co, Ni, Fe) for water splitting: Recent progress and future challenges. *Energy Environ Sci* 5:6012–6021.

181. Wiechen M, Berends H-M, Kurz P (2012) Water oxidation catalysed by manganese compounds: from complexes to 'biomimetic rocks'. *Dalton Trans* 41:21–31.

182. Fillol JL et al. (2011) Efficient water oxidation catalysts based on readily available iron coordination complexes. *Nature Chem* 3:807–813.

183. Mirzakulova E et al. (2012) Electrode-assisted catalytic water oxidation by a flavin derivative. *Nature Chem* 4:794–801.

184. Youngblood WJ et al. (2009) Photoassisted overall water splitting in a visible light-absorbing dye-sensitized photoelectrochemical cell. *J Am Chem Soc* 131:926–927.

185. Brimblecombe R, Koo A, Dismukes GC, Swiegers GF, Spiccia L (2010) Solar driven water oxidation by a bioinspired manganese molecular catalyst. *J Am Chem Soc* 132:2892–2894.

186. Zhao Y et al. (2012) Improving the efficiency of water splitting in dye-sensitized solar cells by using a biomimetic electron transfer mediator. *Proceedings of the National Academy of Sciences* 109:15612–15615.

187. Swierk JR et al. (2014) Photovoltage effects of sintered IrO_2 nanoparticle catalysts in water-splitting dye-sensitized photoelectrochemical cells. *J Phys Chem C*. 118: 17046-17053.

188. Moore GF et al. (2011) A visible light water-splitting cell with a photoanode formed by codeposition of a high-potential porphyrin and an iridium water-oxidation catalyst. *Energy Environ Sci* 4:2389–2392.

189. Mishra A, Fischer MKR, Bäuerle P (2009) Metal-free organic dyes for dye-sensitized solar cells: from structure: property relationships to design rules. *Angew Chem Intl Ed* 48:2474–2499.

190. Ooyama Y, Harima Y (2009) Molecular designs and syntheses of organic dyes for dye-sensitized solar cells. *Eur J Org Chem* 2009:2903–2934.

191. Thompson BC, Fréchet JMJ (2008) Polymer–fullerene composite solar cells. *Angew Chem Intl Ed* 47:58–77.

192. Dennler G, Scharber MC, Brabec CJ (2009) Polymer-Fullerene Bulk-Heterojunction Solar Cells. *Adv Mater* 21:1323–1338.

193. Tachan Z, Hod I, Zaban A (2013) The TiO_2-catechol complex: coupling type ii sensitization with efficient catalysis of water oxidation. *Adv Energy Mater* 4: 1301249.

194. Gouterman M (1961) Spectra of porphyrins. *Journal of Molecular Spectroscopy* 6:138–163.

195. Watson DF, Marton A, Stux AM, Meyer GJ (2003) Insights into dye-sensitization of planar TiO_2: evidence for involvement of a protonated surface state. *J Phys Chem B* 107:10971–10973.

196. Kavan L, Grätzel M, Gilbert SE, Klemenz C, Scheel HJ (1996) Electrochemical and photoelectrochemical investigation of single-crystal anatase. J Am Chem Soc 118: 6716–6723.

197. Qu P, Meyer GJ (2001) Proton-controlled electron injection from molecular excited states to the empty states in nanocrystalline TiO 2. Langmuir 17:6720–6728.

198. Galoppini E, et al. (2002) Long-range electron transfer across molecule-nanocrystal- line semiconductor interfaces using tripodal sensitizers. J Am Chem Soc 124(26): 7801–7811.

199. Bonhôte P, et al. (1998) Efficient lateral electron transport inside a monolayer of aromatic amines anchored on nanocrystalline metal oxide films. J Phys Chem B 102: 1498–1507.

200. Hanson K et al. (2012) Structure-property relationships in phosphonate-derivatized, ru iipolypyridyl dyes on metal oxide surfaces in an aqueous environment. *J Phys Chem C* 116:14837–14847.

201. Swierk JR, McCool NS, Saunders TP, Barber GD, Mallouk TE Effects of electron trapping and protonation on the efficiency of water-splitting dye-sensitized solar cells. *J Am Chem Soc*., ASAP article.

202. Bergeron BV, Kelly CA, Meyer GJ (2003) Thin film actinometers for transient absorption spectroscopy: applications to dye-sensitized solar cells. *Langmuir* 19:8389–8394.

203. Spellane PJ, Gouterman M, Antipas A, Kim S, Liu YC (1980) Porphyrins. 40. Electronic spectra and four-orbital energies of free-base, zinc, copper, and palladium tetrakis(perfluorophenyl)porphyrins. *Inorg Chem* 19:386–391.

204. Kadish KM, Morrison MM (1976) Solvent and substituent effects on the redox reactions of para-substituted tetraphenylporphyrin. *J Am Chem Soc* 98:3326–3328.

205. Helms A, Heiler D, McLendon G (1991) Dependence of electron transfer rates on donor-acceptor angle in bis-porphyrin adducts. *J Am Chem Soc* 113:4325–4327.

206. Fonda HN et al. (1993) Spectroscopic, photophysical, and redox properties of some meso-substituted free-base porphyrins. *J Phys Chem* 97:7024–7033.

207. Fungo F, Otero L, Durantini EN, Silber JJ, Sereno LE (2000) Photosensitization of thin sno 2nanocrystalline semiconductor film electrodes with metallodiporphyrin. *J Phys Chem B* 104:7644–7651.

208. Asbury JB, Hao E, Wang Y, Ghosh HN, Lian T (2001) Ultrafast electron transfer dynamics from molecular adsorbates to semiconductor nanocrystalline thin films. *J Phys Chem B* 105:4545–4557.

209. Martini LA et al. (2013) Modular assembly of high-potential zn-porphyrin photosensitizers attached to TiO_2 with a series of anchoring groups. *J Phys Chem C* 117:14526–14533.

210. Brennan BJ et al. (2013) Comparison of silatrane, phosphonic acid, and carboxylic acid functional groups for attachment of porphyrin sensitizers to TiO_2 in photoelectrochemical cells. *Phys Chem Chem Phys* 15:16605–16614.

211. *Hammes-Schiffer et all ;J. Am. Chem. Soc.*, **2011**, *133* (21), pp 8282–8292Costentin, C.; Robert, M.; Saveant, J.-M. J. Am. Chem. Soc. 2006 , 128 , 4552

212. Richards, J. A.; Whitson, P. E.; Evans, D. H. J. Electroanal. Chem. Interfacial Electrochem. 1975 , 63 , 311.

213. Rockström J, Steffen W, Noone K, Persson A, Chapin FS, Lambin EF, Lenton TM, Scheffer M, Folke C, Schellnhuber HJ, Nykvist B, de Wit CA, Hughes T, van der Leeuw S, Rodhe H, Sörlin S, Snyder PK, Costanza R, Svedin U, Falkenmark M, Karlberg L, Corell RW, Fabry VJ, Hansen J, Walker B, Liverman D, Richardson K, Crutzen P, Foley JA (2009) A safe operating space for humanity. Nature 461:472–475. doi: 10.1038/461472a

214. Armaroli N, Balzani V (2007) The future of energy supply: challenges and opportunities. Angew Chem Int Ed Engl 46:52–66. doi: 10.1002/anie.200602373

215. Sorensen BS (2010) Renewable energy, fourth edition: physics, engineering, environmental impacts, economics & planning, 4 ed. Academic Press

216. Umena Y, Kawakami K, Shen JR, Kamiya N (2011) Crystal structure of oxygen-evolving photosystem II at a resolution of 1.9 Å Nature 473:55-60. doi: 10.1038/nature09913

217. Yachandra V.K.; Sauer, K.; Klein, M. P.; Manganese Cluster in Photosynthesis: Where Plants Oxidize Water to Dioxygen *Chem. Rev.*, **1996**, 96, 2927-2950

218. Mc Evoy, J. P.; Brudvig, G. W. Water-splitting chemistry of photosystem II *Chem. Rev.* **2006**, 106, 4455-4483

219. Barry, B. A.; Babcock, G. T. Tyrosine radicals are involved in the photosynthetic oxygen-evolving system *Proc. Natl. Acad. Sci. U. S. A.* **1987**, 84, 7099-7103

220. Debus, R. J.; Barry, B. A.; Babcock, G. T.; McIntosh, L. Site-directed mutagenesis identifies a tyrosine radical involved in the photosynthetic oxygen-evolving system *Proc. Natl. Acad. Sci. U. S. A.* **1988**, 85, 427-430

221. Jackson D. Megiatto, Jr., Antaeres Antoniuk-Pablant, Benjamin D. Sherman, Gerdenis Kodis, Miguel Gervaldo, Thomas A. Moore, Ana L. Moore, and Devens Gust, Mimicking the electron transfer chain in photosystem II with a molecular triad thermodynamically capable of water oxidation *PNAS,* **2012**, 109 (39) 15578-15583

Bard, A. J.; Faulner, L. R. Electrochemical Methods: Fundamentals and Applications, *Wiley*, **2000**

APPENDIX A

SUPPLEMENTARY INFORMATION FOR CHAPTER 2

Steady state absorption and emission in ethanol solution.

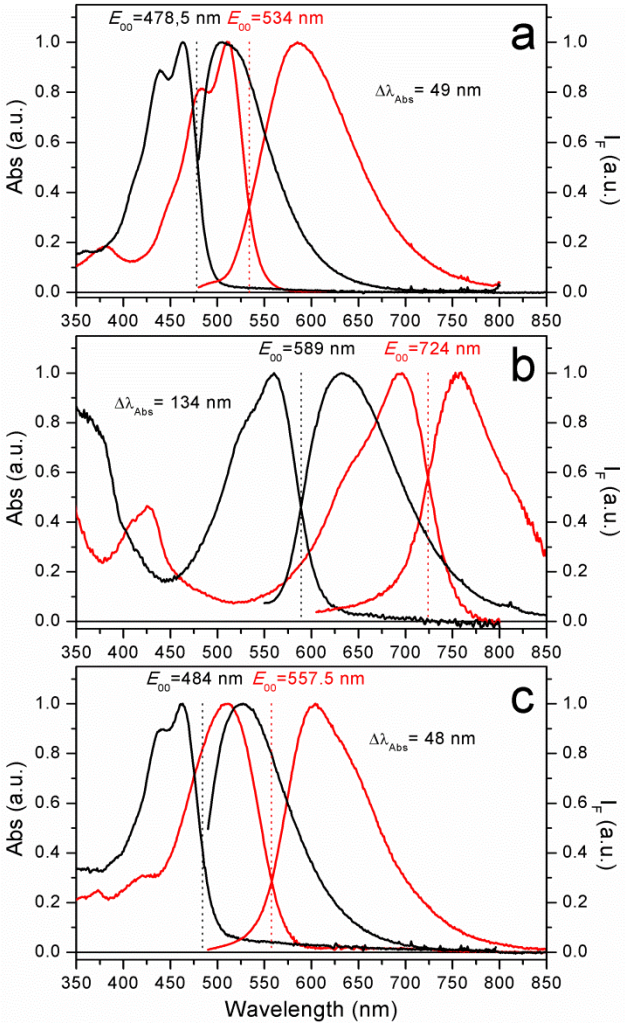

Figure S1 –Absorption and emission spectra of perylenes

Absorption and emission spectra of 1 (a), 2 (b), and 3 (c) in ethanol without (red, C species) and with (black, O species) 3.3 mM KOH. Emission spectra were taken with excitation at 472 nm, 530 nm, and 475 nm, for 1, 2, and 3 respectively. Dye concentration was ~ 10^{-6} M for all samples.

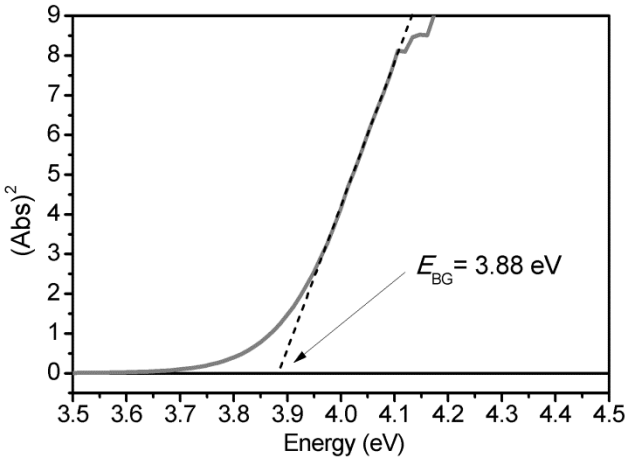

Figure S2 – Absorption onset value of the first direct allowed transition in TiO_2 NPs

Absorption onset value of the first direct allowed transition in TiO_2 NPs. Intersection of the dotted line at y = 0 indicates the estimated E_{BG} of the TiO_2 NPs. [1]

Optimized molecular structure of the dyes.

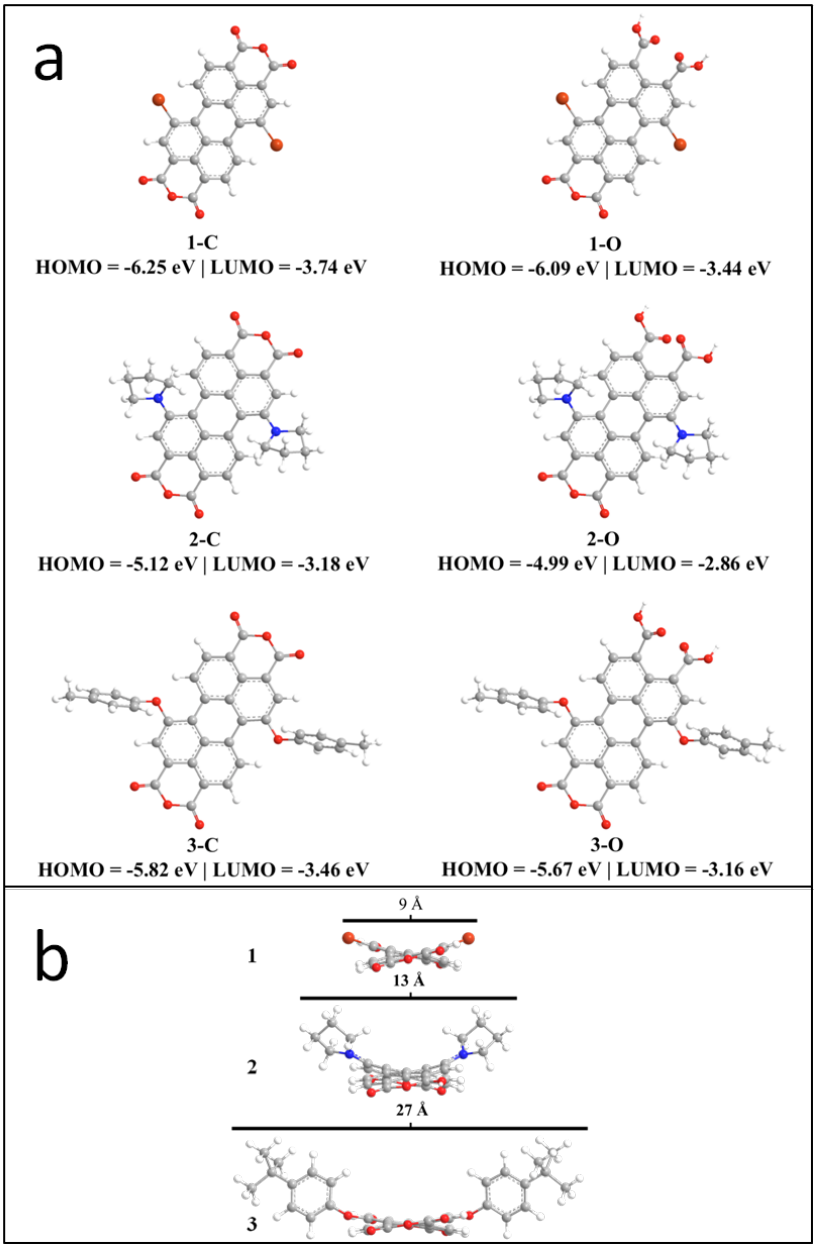

Figure S3 – Optimized structures of perylenes

a) Optimized structures of perylenes 1-3 in their closed (C) and open (O) form along with their corresponding HOMO and LUMO energies (eV vs. vacuum). The calculations were done with Gaussian 09 at the B3LYP/6-31G(d) level of theory using acetonitrile as a solvent simulated with the Conductor-like Polarizable Continuum Model (CPCM). b) Optimized molecular structure of dyes 1, 2 and 3 indicating the largest molecular dimension (D) across the perylenes' bay substituents.

TC-SPC results for dyes 1 and 2 on control samples of micelles without TiO_2 NPs.

Figure S4 shows the TC-SPC results of the 1-micelle system, global analysis yields three decay components ($\chi^2 = 1.14$) with lifetimes of 730 ps, 3.04 ns, and 6.63 ns. The first and second fluorescence DAS are associated with small fractions of 1-O species in different environments whereas the third fluorescence DAS is associated with the 1-C species. The small negative amplitudes seen at the red side of the 730 ps and 3.04 ns components suggest energy transfer from 1-O to 1-C species and indicate the presence of more of one dye per micelle.

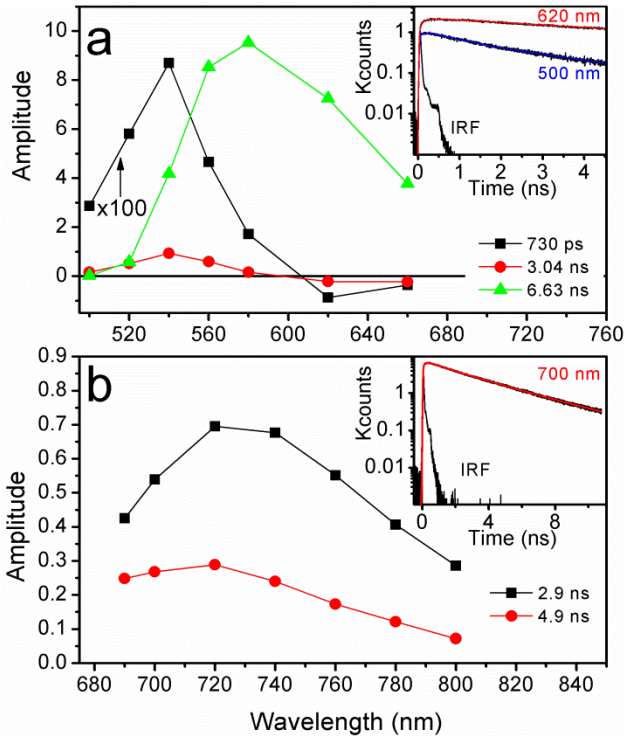

Figure S4 – Emission decay associated spectra of the micelle system

a) Emission decay associated spectra of the 1-micelle system, data was acquired with excitation at 480 nm. Data was globally fit (χ^2= 1.14) as described in the experimental section. Insert: kinetic traces and corresponding fits (smooth line) at selected wavelengths and the Instrument Response Function (IRF). b) same as (a) for the 2-micelle system (χ^2= 1.09). data was aquired with excitation at 640 nm. Dye concentration was ~ 10^{-6} M for all samples.

Flash photolysis results of the 2-TiO_2 system in air and argon saturated solutions.

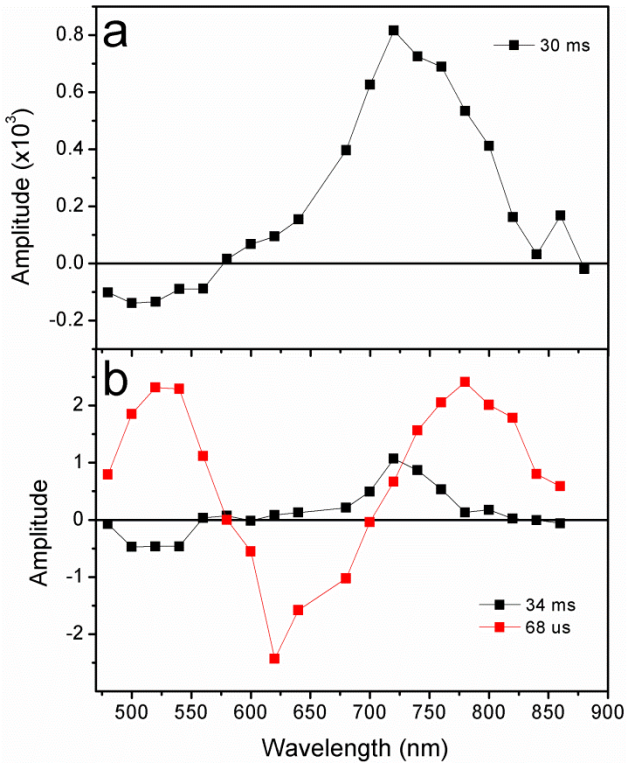

Figure S5 – Decay associtated spectra of the TiO_2 system

Decay associated spectra of the 2-TiO_2 system in air (a) and argon (b) saturated solutions measured by flash photolysis (ns-μs range). Data was acquired with laser excitation at 660 nm.

Pump-probe results of the 2-TiO_2 system in air and argon saturated solutions.

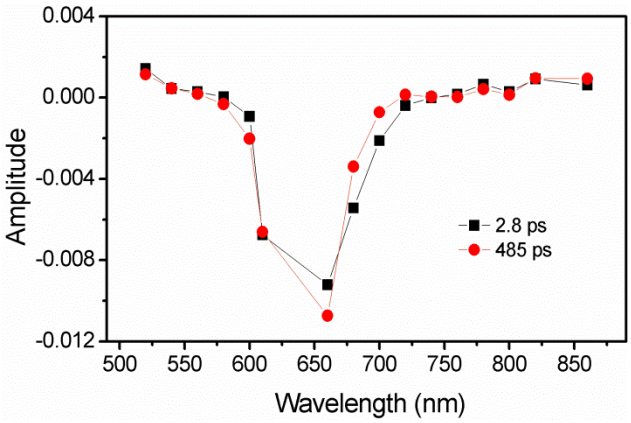

Figure S6 – Decay associated spectra measured by pump-probe
a) Decay associated spectra of the 2-TiO_2 system measured by pump-probe (fs-ps range). Data was acquired with laser excitation at 640 nm.

Estimation of the average number of dyes per micelle and per TiO_2 NP.

The average number of dyes per micelle is calculated as $\lambda_m = C_{dye}/C_m$ and the average number of dyes per TiO_2 NP is estimated as $\lambda_{NP} = C_{dye}/C_{NP}$. The concentration of dye was $C_{dye} \sim 10^{-6}$ M for all experiments except for the pump probe experiments where the concentration was increased two times. The concentration of micelles and TiO_2 nanoparticles are estimated as described below.

The micelle concentration (C_m) was calculated from Equation S1,

(S1) $$C_m = \frac{A \cdot C_{AOT}}{4\pi \cdot r_w^2}$$

where A is the effective head-group area of the AOT molecule at the water/oil interface in the droplet at a particular w_0, C_{AOT} is the AOT concentration, and r_w is the water pool radius. Considering: $A = 16.7$ Å^2 (at $w_0 = 1$) [2], $C_{AOT} = 0.4$ M, and assuming that $r_w = r_{NP} = 17.5$ Å, we estimate $C_m = 1.7\times10^{-3}$ M. Alternatively r_w can be estimated by Equation S2:

(S2) $$\frac{r_w^{\,3}}{(r_w - L)^3} = 1 + \frac{V_{AOT}}{w_0 V_w}$$

where V_w is the volume of a water molecule (30 Å^3), V_{AOT} is the volume of an AOT molecule (825 Å^3) and L is the linear length of an AOT molecule (15 Å). Solving Equation S2 (with $w_0 = 1$) yields $r_w = 22.3$ Å and using this value in Equation S1 gives $C_m = 1.1\times10^{-3}$ M which is very similar to the previously estimated value.

The TiO_2 NPs concentration (C_{NP}) was calculated from Equation S3 assuming spherical particles (as shown in the TEM micrographs).

(S3) $$C_{NP} = C_{TTIP} \cdot \frac{3V_m}{4\pi N_a r_{NP}^3}$$

where C_{TTIP} is the initial concentration of the TiO_2 precursor, N_a is Avogadro's number, V_m is the bulk TiO_2 molar volume and r_{NP} is the average particle radius. Considering C_{TTIP} = 9.1×10^{-4} M, V_m = 18.9 cm^3/mol, and r_{NP} = 1.75 nm (measured from TEM micrographs) we estimate C_{NP} = 1.3×10^{-6} M.

APPENDIX B

SUPPLEMENTARY INFORMATION FOR CHAPTER 3

Transmission Electron Microscopy micrographs of TiO_2 Nanoparticles.

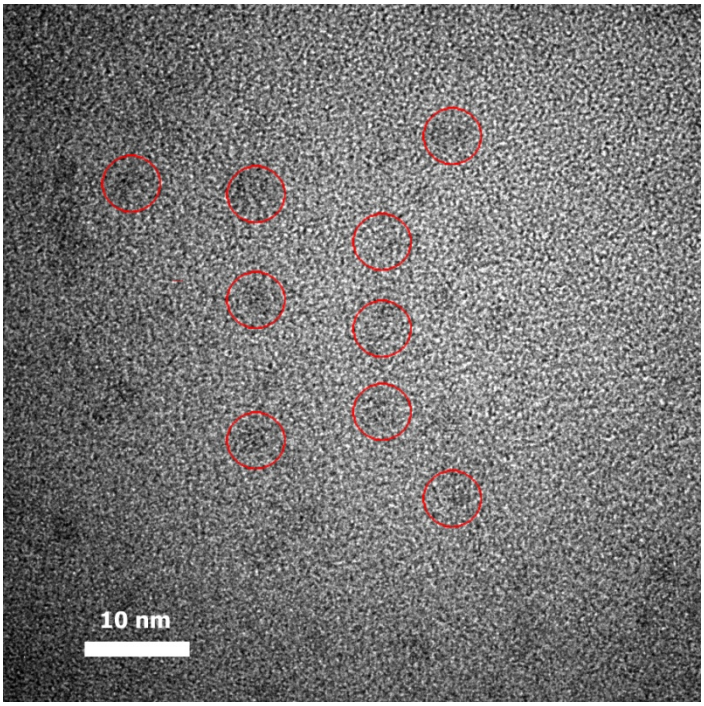

Figure S7 – TEM micrographs of TiO_2 nanoparticles.
Bar scale 10 nm.

Time sequence of steady state absorption of dye 3 upon incubation with TiO_2 NPs

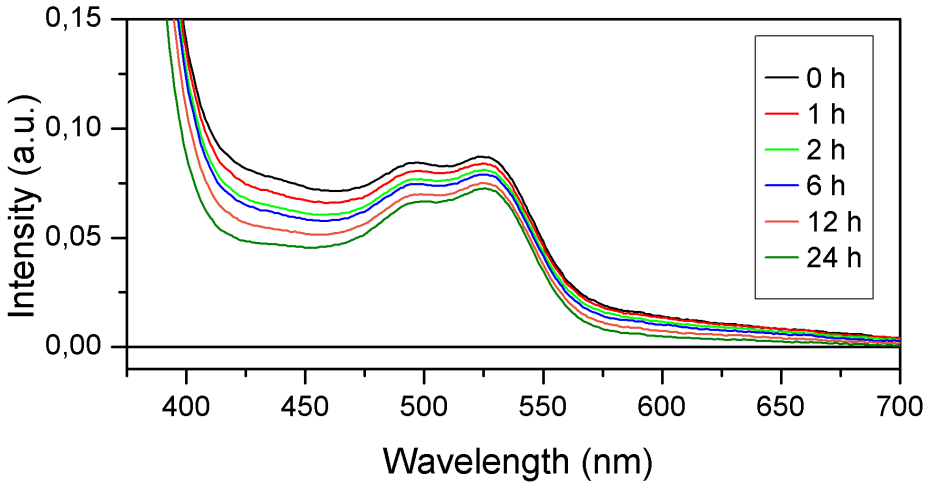

Figure S8 – Time sequence of absorption spectra

Time sequence of absorption spectra collected after addition of 3 to a suspension of TiO_2 NPs in THF. [Dye] = ~ 10^{-6} M, estimated [NP] = ~ 0.1 mg/mL.

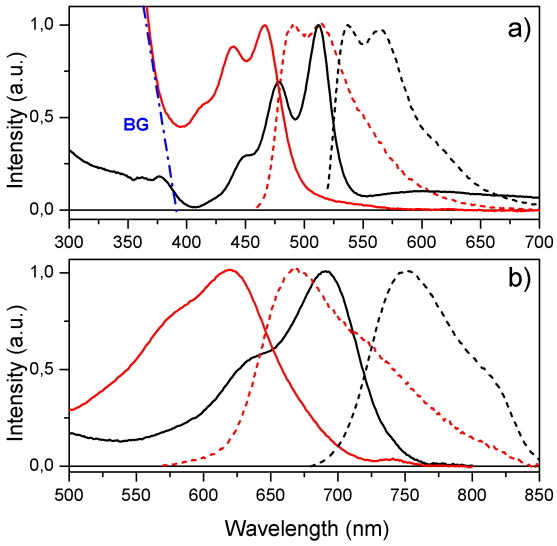

Figure S9 – Normalized absorption and emission spectra

a) Normalized absorption (solid lines) and emission (dashed lines) spectra of dye 1 in THF before (black) and after (red) the attachment to the TiO_2 NP. Dashed blue line corresponds to the TiO_2 band gap (BG). b) Normalized absorption (solid lines) and emission (dashed lines) spectra of dye 2 in THF before (black) and after (red) the attachment to the TiO_2 NP.

TC-SPC measurements

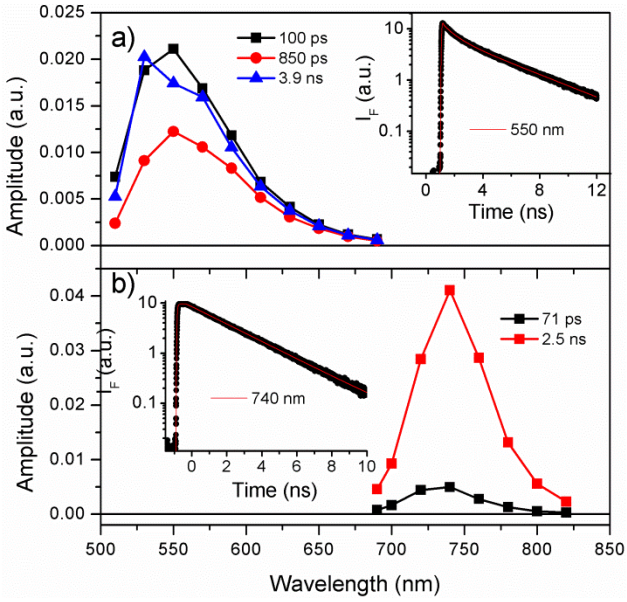

Figure S10 – Fluorescence decay associated spectra

Fluorescence decay associated spectra of a) Dye 1 in THF recorded upon excitation at 450 nm. Insert displays kinetic trace (data points) and corresponding fit (smooth line) recorded at the indicated wavelength. b) Dye 2 in THF recorded upon excitation at 640 nm. Insert displays kinetic trace (data points) and corresponding fit (smooth line) recorded at the indicated wavelength. Dye concentration was ~ 10^{-6} M for all samples.

Femtosecond transient absorption experiments

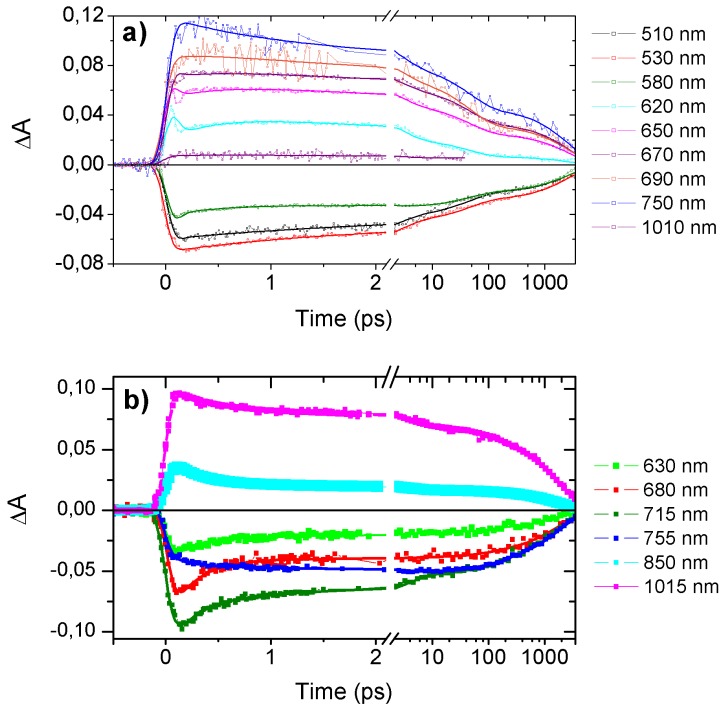

Figure S11 – Transient absorption kinetics

Transient absorption kinetics traces of a) Dye 1 in THF recorded upon excitation at 490 nm. b) Dye 2 in THF recorded upon excitation at 640 nm.

APPENDIX C

SUPPLEMENTARY INFORMATION FOR CHAPTER 4

Preparation of compounds used in this study.

Bis(2,2'-bipyridine)(4,4'-diphosphonato-2,2'-bipyridine)ruthenium bromide ([$Ru(bpy)_2$(4,4'-$(PO_3H_2)_2$bpy)]),(1) 5-(4-carboxyphenyl)-10, 15, 20-tris(2, 4, 6-trimethylphenyl)porphyrin (TMP)(2) and 5-(4-carboxyphenyl)-10, 15, 20-tris(4-methylphenyl)porphyrin (TTP)(3) were prepared according to literature methods. (1-3)

Preparation of 5-(4-carboxyphenyl)-15-(2, 4, 6-trimethylphenyl)porphyrin (MMP). To a flask containing 0.5 g (0.89 mmol) of 5-(4-methoxycarbonylphenyl)-15-(2, 4, 6-trimethylphenyl)porphyrin (4) was added 200 mL of tetrahydrofuran (THF), 100 mL of methanol (MeOH) and 40 mL of 10% aqueous potassium hydroxide. The solution was warmed to 40^{o}C and stirred under an argon atmosphere for 16 h. When thin layer chromatography (TLC) ($CHCl_3$/MeOH, 9:1) indicated that the reaction was complete, the solution was diluted with $CHCl_3$ (200 mL) and washed three times with water. The organic layer was collected and evaporated to dryness, and the solid was dried under high vacuum to give 470 mg (96%) of the desired porphyrin. ^{1}H NMR (400 MHz) δ -3.08 (2H, s, -NH), 1.85 (6H, s, Ar-CH_3), 2.66 (3H, s, Ar-CH_3), 7.33 (2H, s, Ar-H), 8.42 (2H, d, *J*=8 Hz, Ar-H), 8.60 (2H, d, *J*=8 Hz, Ar-H), 8.90 (2H, d, *J*=5 Hz, β-H), 9.05 (2H, d, *J*=5 Hz, β-H), 9.35 (2H, d, *J*=4 Hz, β-H), 9.43 (2H, d, *J*=4 Hz, β-H), 10.30 (2H, s, meso-H); MALDI-TOF-MS m/z calcd for $C_{36}H_{28}N_4O_2$, 548.2, obsd, 548.4; Uv/vis (CH_2Cl_2) 407, 502, 535, 576, 631 (nm).

Preparation of 5-[N-(3, 5-di-t-butylphenyl)-4-benzamido]-15-(4-methoxycarbonylphenyl)-10, 20-bis(2, 4, 6-trimethylphenyl)porphyrin. To a flask containing 100 mg (0.13 mmol) of 5-(4-carboxyphenyl)-15-(4-methoxycarbonylphenyl)-10, 20-bis(2, 4, 6-trimethylphenyl)porphyrin,(5) 29 mg (0.14 mmol) of 3, 5-di-*t*-butylaniline, 36 mg (0.19 mmol) of 4-DMAP and 20 mL of dichloromethane was added 36 mg (0.19 mmol) of EDCI HCl. The solution was stirred at room temperature under an argon atmosphere for 15 h. TLC (dichloromethane/hexanes, 3:1) indicated that the reaction was complete. The reaction mixture was diluted with dichloromethane (100 mL) and washed with an aqueous solution of sodium bicarbonate and then water. The organic phase was passed through a bed of anhydrous sodium sulfate. The solution was concentrated to dryness under reduced pressure and the residue was chromatographed on silica gel (dichloromethane /hexanes 5:1 to 10:1) to give 106 mg (86%). ^{1}H NMR (400 MHz) δ -2.63 (2H, s, -NH), 1.42(18H, s, -CH_3), 1.84(12H, s, Ar-CH_3), 2.63(6H, s, Ar-CH_3), 4.10(3H, s, -OCH_3), 7.29(4H, s, Ar-H), 7.31 (1H, t, *J*=2 Hz, Ar-H), 7.67 (2H, d, *J*=2 Hz, Ar-H), 8.14 (1H, s, -NH), 8.27 (2H, d, *J*=8 Hz, Ar-H), 8.31 (2H, d, *J*=8 Hz, Ar-H), 8.36 (2H, d, *J*=8 Hz, Ar-H), 8.43 (2H, d, *J*=8 Hz, Ar-H), 8.71-8.78 (8H, m, β-H); MALDI-TOF-MS m/z calcd for $C_{67}H_{65}N_5O_3$, 987.5, obsd 987.5; Uv/vis (CH_2Cl_2) 419, 515, 549, 589, 646 (nm).

Preparation of 5[N-(3, 5-di-t-butylphenyl)-4-benzamido]-15-(4-carboxyphenyl)-10, 20-bis(2, 4, 6-trimethylphenyl)porphyrin (PAP). To a flask containing 460 mg (0.47 mmol) of 5-[N-(3, 5-di-*t*-butylphenyl)-4-benzamido]-15-(4-methoxycarbonylphenyl)-10, 20-bis(2, 4, 6-trimethylphenyl)porphyrin was added 80 mL of THF, 40 mL of methanol and 20 mL of 10% aqueous potassium hydroxide. After the solution was stirred at room temperature for 64 h, TLC indicated that all the starting material had been consumed. The reaction mixture was diluted with chloroform (200 mL) and washed first with 0.5 M citric acid solution and then twice with water. The solvent was evaporated under reduced pressure and the solid was dried under high vacuum to give 430 mg (95% yield) of the porphyrin acid. ^{1}H NMR (400 MHz) δ -2.61 (2H, s, -NH), 1.42 (18H, s, -CH_3), 1.85 (12H, s, Ar-CH_3), 2.63 (6H, s, Ar-CH_3), 7.30 (4H, s, Ar-H), 7.31(1H, m, Ar-H), 7.67 (2H, s, Ar-H), 8.13 (1H, s, -NH), 8.28 (2H, d, *J*=8 Hz, Ar-H), 8.37 (2H, d, *J*=8 Hz, Ar-H), 8.38 (2H, d, *J*=8 Hz, Ar-H), 8.54 (2H, d, *J*=8 Hz, Ar-H), 8.73-8.79 (8H, m, β-H); MALDI-TOF-MS m/z calcd for $C_{66}H_{63}N_5O_3$, 973.5, obsd, 973.5; Uv/vis (CH_2Cl_2) 419, 514, 549, 590, 645 (nm).

Preparation of 5-15-bis(2, 4, 6-trimethylphenyl)porphyrinatocopper(II). To a flask containing 250 mg (0.46 mmol) of 5, 15-bis(2, 4, 6-trimethylphenyl)porphyrin(6) was added 160 mL of chloroform and 80 mL of methanol that was saturated with copper (II) acetate. The solution was warmed to 50^{o}C and after stirring for two h, TLC indicated that metalation was complete. The reaction mixture was washed with water (500 mL) and the orange organic layer was passed through a bed of anhydrous sodium sulfate. The solvent was then evaporated under reduced pressure and the residue was dried to give 248 mg

(89% yield) of the copper porphyrin. MALDI-TOF-MS m/z calcd for $C_{38}H_{32}N_4Cu_1$, 607.2, obsd, 607.3; Uv/vis (CH_2Cl_2) 403, 527, 562 (nm).

Preparation of 5-formyl-10, 20-bis(2, 4, 6-trimethylphenyl)porphyrinatocopper (II). To a flask containing 20 mL of dimethylformamide (DMF) at -5^oC was added 5.5 mL (59 mmol) of phosphoryl chloride over a 10 min period. The salt/ice bath was removed and stirring of the pale yellow oil was continued for an additional 30 min. The above solution was then added via a cannula to a solution comprised of 0.55 g (0.90 mmol) of 5-15-bis(2, 4, 6-trimethylphenyl)porphyrinatocopper(II) and 250 mL of 1, 2-dichloroethane. Stirring at room temperature was continued for several min then at 60^oC under an argon atmosphere for two h. The reaction mixture was cooled and 250 mL of aqueous sodium bicarbonate was cautiously added. The two phase mixture was vigorously stirred as solid sodium bicarbonate was added in small portions until all the acid had been neutralized. The organic layer was collected and after washing with water the green solution was passed through a bed of anhydrous sodium sulfate and the solvent was evaporated at reduced pressure. Residual DMF was removed under high vacuum. The residue was chromatographed on silica gel (dichloromethane/hexanes, 2:3 to 2:1) to give 480 mg (83% yield) of the formyl porphyrin. MALDI-TOF-MS m/z calcd for $C_{39}H_{32}N_4O_1Cu_1$, 635.2, obsd, 635.3; Uv/vis (CH_2Cl_2) 417, 517(sh), 548, 591 (nm).

Preparation of 5-formyl-10, 20-bis(2, 4, 6-trimethylphenyl)porphyrin. To a flask containing 450 mg (0.71 mmol) of 5-formyl-10, 20-bis(2, 4, 6-trimethylphenyl)porphyrinatocopper (II) was added 50 mL of TFA and then 5 mL of concentrated sulfuric acid. The solid dissolved and after 10 min TLC (dichloromethane/hexanes, 1:1) indicated that all the starting material had been consumed. The reaction mixture was poured over ice and the mixture was stirred until all the ice had melted. The porphyrin was extracted into chloroform and the combined extracts were washed with aqueous sodium bicarbonate and dried over anhydrous sodium sulfate. The organic solution was concentrated to about 80 mL and then passed down a short silica gel column ($CHCl_3$) to remove polar material. The solvent was evaporated under reduced pressure and the residue was dried under vacuum to give 344 mg (85% yield) of the free base porphyrin. ^{1}H MNR (300 MHz) δ -2.71 (2H, s, -NH), 1.84 (12H, s, Ar-CH_3), 2.65 (6H, s, Ar-CH_3), 7.31 (4H, s, Ar-H), 8.72 (2H, d, *J*=5 Hz, β-H), 8.91 (2H, d, *J*=5 Hz, β-H), 9.22 (2H, d, *J*=5 Hz, β-H), 10.04 (2H, d, *J*=5 Hz, β-H), 10.16 (1H, s, meso-H), 12.54 (1H, s, -CHO); MALDI-TOF-MS m/z calcd for $C_{39}H_{34}N_4O_1$, 574.3, obsd, 574.5; Uv/vis (CH_2Cl_2) 421, 521, 560, 595, 650 (nm).

Preparation of 10-[2-(4-methoxycarbonylphenyl)ethenyl]-5, 15-bis(2, 4, 6-trimethylphenyl)porphyrin. To a flask containing 58 mg (0.10 mmol) of 5-formyl-10, 20-bis(2, 4, 6-trimethylphenyl)porphyrin was added 250 mg (0.50 mmol) of 4-carboxymethylbenzyltriphenylphosphonium bromide and 10 mL of dimethyl sulfoxide. The mixture was stirred as 33 mg (0.61 mmol) of sodium methoxide was added and then stirred at 60^{o}C under an argon atmosphere for two h. TLC (hexanes/10% ethyl acetate)

indicated that the reaction was complete. The reaction mixture was poured into diethyl ether (150 mL) and then washed with water four times. The solvent was evaporated at reduced pressure and the residue was chromatographed on silica gel (dichloromethane/hexanes, 1:1 to 3:2) to give 67 mg (94% yield) of the desired porphyrin. ^{1}H NMR (300 MHz) δ -2.68 (2H, s, -NH), 1.86 (12H, s, Ar-CH_3), 2.66 (6H, s, Ar-CH_3), 4.01 (3H, s, -OCH_3), 7.31 (4H, s, Ar-H), 7.44 (1H, d, *J*=16 Hz, vinyl-H), 8.00 (2H, d, *J*=8 Hz, Ar-H), 8.25 (2H, d, *J*=8 Hz, Ar-H), 8.79-8.82 (4H, m, β-H), 9.23 (2H, d, *J*=5 Hz, β-H), 9.49 (2H, d, *J*=5 Hz, β-H), 9.79 (1H, d, *J*=16 Hz, vinyl-H), 10.07 (1H, s, meso-H); MALDI-TOF-MS m/z calcd for $C_{48}H_{42}N_4O_2$, 706.3, obsd, 706.3; Uv/vis (CH_2Cl_2) 423, 517, 558, 594, 653 (nm).

Preparation of 10-[2-(4-carboxyphenyl)ethenyl]-5, 15-bis(2, 4, 6-trimethylphenyl)porphyrin (DMEP). To a flask containing 60 mg (0.08 mmol) of 10-[2-(4-methoxycarbonylphenyl)ethenyl]-5, 15-bis(2, 4, 6-trimethylphenyl)porphyrin was added 20 mL of THF, 10 mL of methanol and 5 mL of 10% aqueous potassium hydroxide. The solution was warmed to 40^{o}C under an argon atmosphere for 24 h. TLC (dichloromethane) indicated that all the starting material had been consumed. The reaction mixture was poured into chloroform (80 mL) and acidified with 0.1M citric acid. After further washings with water, the organic solution was concentrated by evaporation at reduced pressure and dried to give 55 mg (93% yield) of the porphyrin acid.^{1}H NMR (400 MHz) δ -2.70 (2H, s, -NH), 1.84 (12H, s, Ar-CH_3), 2.64 (6H, s, Ar-CH_3), 7.30 (4H, s, Ar-H), 7.44 (1H, d, *J*=16 Hz, vinyl-H), 8.02 (2H, d, *J*=8 Hz, Ar-H), 8.30 (2H, d, *J*=8 Hz, Ar-H), 8.78 (2H, d, *J*=5 Hz, β-H), 8.79 (2H, d, *J*=5 Hz, β-H), 9.22 (2H, d, *J*=5 Hz, β-

H), 9.47 (2H, d, *J*=5 Hz, β-H), 9.80(1H, d, *J*=16 Hz, vinyl-H), 10.05 (1H, s, meso-H); MALDI-TOF-MS m/z calcd for $C_{47}H_{40}N_4O_2$, 692.3, obsd, 692.4; Uv/vis (CH_2Cl_2) 423, 517, 559, 592, 654 (nm).

Preparation of 5-(4-carboxyphenyl)-10, 20-bis(2, 4, 6-trimethylphenyl)porphyrin (DMP). In a vial equipped with a magnetic stir bar, 10-(4-methoxycarbonylphenyl)-5,15-bis(2, 4, 6 trimethylphenyl)porphyrin (7) (6 mg, 0.0088 mmol) was dissolved in THF (1.5 mL) followed by the addition of KOH/methanol (10% w/v, 0.5 mL). The reaction mixture was stirred at room temperature overnight. The mixture was applied to a short column of silica gel, which was eluted with 10% methanol/CH_2Cl_2. The eluent was concentrated by distillation at reduced pressure. The residue was chromatographed on silica gel (8% methanol/CH_2Cl_2) to obtain 5 mg (85% yield) of the porphyrin. ^{1}H NMR (400 MHz) δ -2.88 (s, 2H, NH), 1.85 (s, 12H, CH_3), 2.65 (s, 6H, CH_3), 7.31 (4H, s, ArH), 8.37 (2H, d, *J* = 8 Hz, ArH), 8.53 (2H, d, J = 8 Hz, ArH), 8.78 (4H, m, βH), 8.85 (2H, d, *J* = 5 Hz, βH), 9.29 (2H, d, *J* = 5 Hz, βH), 10.15 (1H, s, mesoH); MALDI-TOF-MS m/z: calcd for $C_{45}H_{38}N_4O_2$, 666.30, obsd, 666.55; UV-vis (CH_2Cl_2): λ_{max}, 413, 508, 540, 583, 638 nm.

Preparation of 5, 15-dicarboxy-10-(2, 4, 6-trimethylphenyl)porphyrin (MDC). A portion of 5, 15-diethoxycarbonyl-10-(2, 4, 6-trimethylphenyl)porphyrin(8) (175 mg, 0.306 mmol) was dissolved in tetrahydrofuran/ethanol (10/10 mL). Then, 85% potassium hydroxide (676 mg, 12 mmol) in water (3 mL) was added to the porphyrin solution. The mixture was refluxed overnight. The mixture was cooled and the solvents were removed by distillation at reduced pressure. Water (20 mL) was added to dissolve the porphyrin residue. Acetic acid (10 mL) was added to the basic aqueous porphyrin solution to

precipitate the diacid porphyrin. The acidified mixture was allowed to stand overnight for Ostwald ripening. The precipitate was filtered, washed with water, roughly dried under aspirator suction, and vacuum-dried at ambient temperature overnight to yield the desired porphyrin (158 mg, 100 %). ^{1}H NMR (DMSO-d_6): δ 14.79 (1H, bs), 10.65 (1H, s), 9.71 (2H, d, *J*=5 Hz), 9.68 (2H, d, *J*=5 Hz), 9.54 (2H, d, *J*=5 Hz), 8.76 (2H, d, *J*=5 Hz), 7.40 (2H, s), 2.63 (3H, s), 1.73 (6H, s), -3.30 (2H, s); MALDI-TOF: *m/z* calculated for $C_{31}H_{24}N_4O_4$, 516.2, obsd, 516.4 UV-vis (MeOH): λ_{max}, 408, 503, 545, 581, 636 nm.

Preparation of 10-carboxy-15-(2, 4, 6-trimethylphenyl)-20-ethoxycarbonylporphyrin (MDCE). A portion of 10,20-diethoxycarbonyl-15-mesitylporphyrin (8) (250 mg, 0.436 mmol) was stirred and heated at 45^{o}C under air in a mixture of THF (18 mL), ethanol (9 mL), and aqueous KOH (460 mg of 85% KOH in 4 mL H_2O) for 20 h. The mixture was cooled to room temperature and the base was quenched with an equivalent of trifluoroacetic acid. After THF and ethanol were evaporated, the porphyrin mixture was extracted with dichloromethane and chromatographed on a silica gel column (10% methanol in dichloromethane) to isolate the desired porphyrin (180 mg, 76% yield). ^{1}H NMR (DMSO-d_6), δ 14.76 (1H, bs), 10.69 (1H, s), 9.75 (2H, m), 9.70 (1H, d, *J*=4 Hz), 9.66 (1H, d, *J*=5 Hz), 9.58 (1H, d, *J*=4 Hz), 9.53 (1H, d, *J*=5 Hz), 8.80 (1H, d, *J*=2.0 Hz), 8.79 (1H, d, *J*=2 Hz), 7.40 (2H, s), 5.08 (2H, q, *J*=7 Hz), 2.63 (3H, s), 1.74 (6H, s), 1.73 (3H, t, *J*=7 Hz), -3.33 (2H, s); MALDI-TOF: *m/z* calcd for $C_{33}H_{28}N_4O_4$, 544.2, obsd, 544.4; UV-vis (CH_2Cl_2): λ_{max} 408, 505, 542, 584, 638 nm.

Spectroscopic characterization. A Cary 6000i (Agilent) was used to collect UV-VIS spectra of the sensitizers in solution and the sensitized electrodes. Extinction coefficients for the sensitizers were determined from a 60 mM solution of the sensitizer in ethyl acetate. Surface coverage of sensitizer was determined from the absorbance at each Q band, averaged, and corrected for scattering from the TiO_2, according to the formula (10):

$$\Gamma\ (mol\ cm^{-2}) = \frac{A(\lambda)/\varepsilon(\lambda)}{1000}$$

To collect steady state emission spectra, the sensitizers were adsorbed onto a TiO_2 film, coated by a 2 nm thick layer of ZrO_2 prepared by atomic layer deposition. Emission spectra were collected with a SPEX Fluorolog 1680 0.22 m double monochromator fluorimeter in 200 mM pH 5.3 sodium phosphate buffer. The sensitizers were excited at the maxima of the $Q_y(1,0)$ peak.

Electrochemistry. All electrochemical and photoelectrochemical measurements were made using a Ag/AgCl (3M NaCl) reference electrode. In all cases a piece of platinum mesh served as the counter electrode. Cyclic voltammograms of sensitized electrodes (without catalyst) were collected in 200 mM pH 5.3 sodium phosphate buffer using a Nuvant EZ-Stat Pro potentiostat at a scan rate of 50 mV/s. Cross-surface electron diffusion measurements were also performed in the same buffer, with the electrode poised at a potential of 1.4 V v. Ag/AgCl.

DFT calculations. DFT calculations were performed at the B3LYP/6-31G(d) level of theory. Structures were optimized in the gas phase followed by a single point energy

calculation in the presence of dichloromethane simulated with the Conductor-like Polarizable Continuum Model (CPCM) (11). A calibration with redox potentials and HOMO-LUMO energies was built using the experimental data of eight porphyrins obtained from the literature measured under similar conditions (0.10 M tetrabutylammonium hexafluorophosphate in dichloromethane) (12-17).

Photoelectrochemical Characterization. All photoelectrochemical experiments were done using a pH 6.8, 100 mM sodium phosphate buffer as the electrolyte.

For photocurrent and open-circuit photovoltage measurements, a 150W Newport Oriel Xe arc lamp fitted with an AM 0, an AM 1.5 filter and a 410 nm or 590 nm long pass filter was used as the illumination source. The sensitized electrode was placed in the anode compartment of a custom H-cell along with the reference electrode and sealed with a septum. A platinum mesh was placed in the adjoining compartment, which was also sealed with a septum and purged with 5% H_2 in argon. Open-circuit photovoltage was measured under illumination with a battery-powered voltmeter. Steady-state photocurrent measurements were performed at +100 mV v. Ag/AgCl for 10 min.

Table S1 – Absorption maxima end extinction coefficients of free base porphyrin sensitizers

Absorption maxima (nm) and molar extinction coefficients (M^{-1} cm^{-1}) of free-base porphyrin sensitizers in ethyl acetate at 298 K

	$Q_y(1,0)$		$Q_y(0,0)$		$Q_x(1,0)$		$Q_x(0,0)$	
Porphyrin	l	e	l	e	l	e	l	e
TMP	513	22450	545	8467	591	6583	647	4600
DMP	506	8433	537	1817	582	2400	638	732
MMP	500	4981	532	1745	575	1590	630	532
DMEP	515	8291	556	6520	594	2762	652	2294
TTP	513	12329	548	6495	591	3633	647	3041
PAP	513	31913	546	13937	590	9376	647	6885
MDC	502	6742	542	7121	580	5019	637	2066
MDCE	504	13572	540	6809	581	5005	637	4232

Table S2 – Absorption maxima
Absorption maxima (nm), absorbance (a.u.), and surface coverage of sensitizers on TiO_2

Porphyrin	Q-Bands (Abs)	$\Gamma \times 10^{-7}$ (mol/cm^2)
TMP	514nm (1.30±0.11); 547nm (0.80±0.02); 593nm (0.61±0.01); 649nm (0.46±0.00)	0.45 ± 0.05
DMP	507nm (1.09±0.04); 538nm (0.48±0.01); 584nm (0.47±0.01); 640nm (0.20±0.00)	0.92 ± 0.05
MMP	506nm (1.73±0.10); 538nm (1.01±0.03); 579nm (0.87±0.03); 633nm (0.48±0.01)	2.84 ± 0.21
DMEP	516nm (1.17±0.11); 559nm (1.04±0.09); 598nm (0.64±0.04); 657nm (0.51±0.03)	1.05 ± 0.13
TTP	517nm (1.33±0.09); 553nm (0.95±0.04); 594nm (0.62±0.02); 650nm (0.53±0.01)	0.84 ± 0.08
PAP	516nm (1.65±0.12); 551nm (1.10±0.05); 593nm (0.74±0.04); 650nm (0.60±0.03)	0.42 ± 0.04
MDC	508nm (0.87±0.07); 546nm (0.57±0.07); 583nm (0.50±0.02); 641nm (0.29±0.04)	0.84 ± 0.10
MDCE	507nm (1.14±0.11); 544nm (0.80±0.03); 593nm (0.64±0.04); 639nm (0.44±0.02)	0.61 ± 0.08

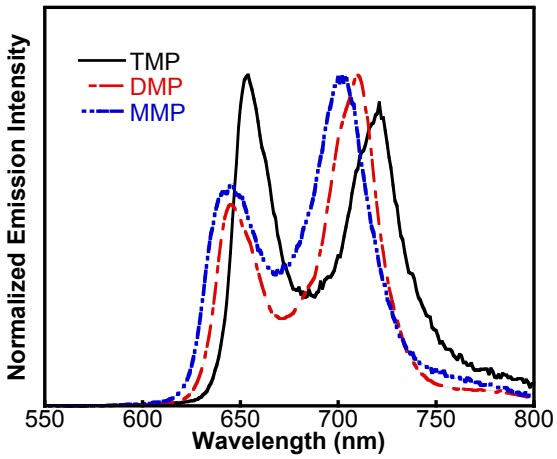

Figure S12 – Emission spectra of TMP, DMP, and MMP
Emission of TMP, DMP, and MMP on ZrO_2-coated TiO_2 in pH 5.3 200 mM sodium phosphate buffer.

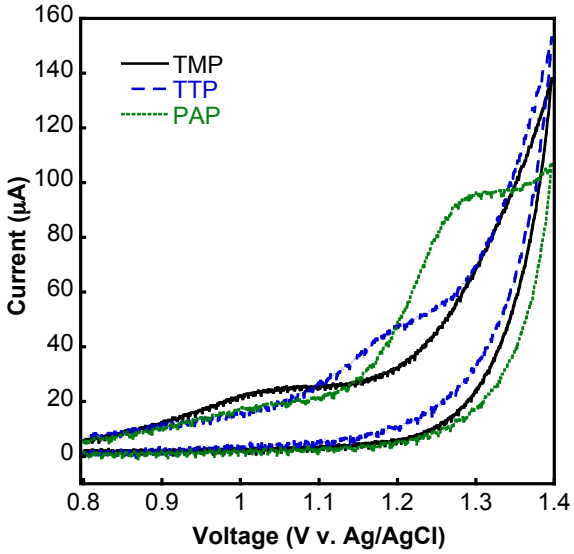

Figure S13 – CV of TMP, TTP, and PAP on TiO_2
CV of TMP, TTP, and PAP on TiO_2. Electrodes submersed in pH 5.3 200 mM sodium phosphate buffer. Potential applied relative to a Ag/AgCl (3M NaCl), platinum mesh counter electrode. Scan rate of 50 mV/s.

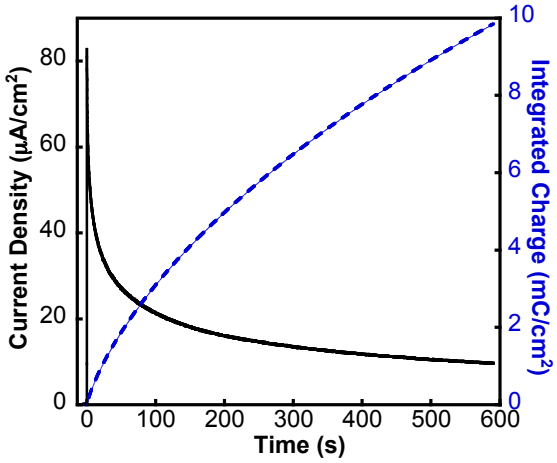

Figure S14 – Representative photocurrent and integrated charge for a DMEP sensitized electrode

Representative photocurrent and integrated charge for a DMEP sensitized electrode under illumination with a 410 nm long-pass filter in pH 6.8 100 mM sodium phosphate buffer, an applied bias of +100 mV v. Ag/AgCl, and a platinum mesh counter electrode.

DFT calculations. In the calibration of our DFT model using eight literature values for porphyrins, a very strong linear correlation was found (with rmsd < 50 mV) between the published reduction potentials and calculated LUMO energies. The correlation for oxidation potentials with HOMO energies was not as strong, but the obtained rmsd of < 100 mV was acceptable for our purposes. We proceeded to use these correlations to estimate the redox potentials of porphyrins used in this study from the calculated HOMO-LUMO energies. E_{ox} was estimated by estimated by extrapolation and E^*_{red} was obtained by substracting 1.9 from E_{ox}. Values are shown in Table S3. With the series TMP, DMP, and MMP, the calculated oxidation potentials were very similar to the measured values on TiO_2. A significant deviation (>170 mV) from calculated values was observed with TTP, PAP, DMEP, and MDEC.

Table S3 – DFT calculations of oxidation potential and excited state reduction potential for various sensitizers

DFT calculations of oxidation potential and excited state reduction potential for various sensitizers vs. Ag/AgCl in dichloromethane.

Porphyrin	E_{ox}	E^*_{red}
TMP	0.97	-0.93
DMP	1.01	-0.89
MMP	1.05	-0.85
DMEP	0.93	-1.00
TTP	1.01	-0.97
PAP	0.90	-0.89
MDC	1.42	-0.48
MDCE	1.39	-0.51

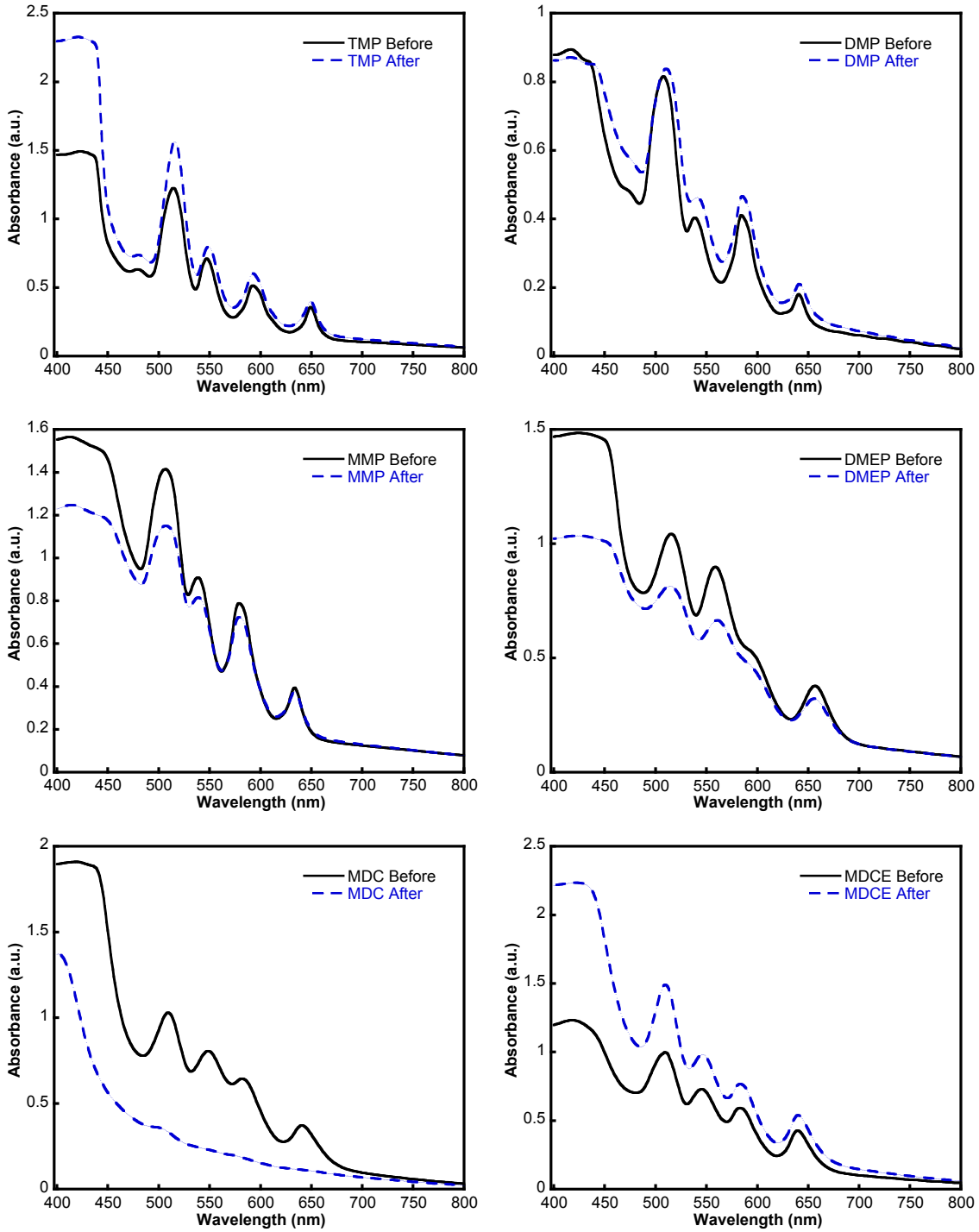

Figure S15 – UV-VIS of sensitized electrodes
UV-VIS of sensitized electrodes before and after 10 min of illumination at +100 mV v. Ag/AgCl in pH 6.8 100 mM sodium phosphate buffer. Clockwise from top left: TMP, DMP, DMEP, MDCE, MDC, and MMP.

APPENDIX D

ARTICLE PERMISSIONS

CHAPTER 2

Reprint adapted with permission from a previously published article:

Hernandez, L.; Godin, R.; Bergkamp, J. J.; Llansola Portoles, M. J.; Sherman, B. D.; Tomlin, J.; Bertolotti, S.; Chesta, C. A.; Marino-Ochoa, E.; Moore, A. L.; Moore, T. A.; Cosa, G.; Palacios, R. E. *J. Phys. Chem. B*, 2013, *117* (16), pp 4568–4581 doi: 10.1021/jp3086792.

My contributions included synthesis and writing of the manuscript.

CHAPTER 3

Reprint adapted with permission from a previously published article:

Llansola-Portoles, M. J.; Bergkamp, J. J.; Tomlin, J.; Moore, T. A.; Kodis, G.; Moore, A. L.; Cosa, G.; Palacios, R. E. *J. Phys. Chem. B*, 2013, *117* (16), pp 4568–4581 doi: 10.1021/jp3086792.

Permission was granted through the Copyright Clearance Center license number: 3617330574041

CHAPTER 4

Reprint adapted with permission from a previously published article:

Swierk, J. R.; Méndez-Hernández, D. D.; McCool, N. S., Liddell, P.; Terazono, Y.; Pahk, I.;Tomlin, J. J.; Oster, N. V.; Moore, T. A.; Moore, A. L.; Gust, D.; Mallouk, T. E. *Proc. Natl. Acad. Sci. U. S. A.* , 2015, 112(6), 1681–1686. doi:10.1073/pnas.1414901112.

My contributions included synthesis. See Appendix D for permission details

Permision was granted to reprint this article by default as PNAS does not require authors to request reprint permission for use in a thesis or dissertation